Title
Theoretical and Numerical Analyses of Flow and Transport in the Spinal Canal

Author
Lawrence, Jenna Joaquin

Publication Date
2021

UNIVERSITY OF CALIFORNIA SAN DIEGO

Theoretical and Numerical Analyses of Flow and Transport in the Spinal Canal

A dissertation submitted in partial satisfaction of the
requirements for the degree
Doctor of Philosophy

in

Engineering Sciences (Mechanical Engineering)

by

Jenna Joaquin Lawrence

Committee in charge:

Professor Antonio Sánchez, Chair
Professor Alexander Norbash
Professor Geno Pawlak
Professor Lonnie Petersen
Professor David Saintillan

2021

The dissertation of Jenna Joaquin Lawrence is approved, and it is acceptable in quality and form for publication on microfilm and electronically:

University of California San Diego

2021

TABLE OF CONTENTS

LIST OF FIGURES

LIST OF TABLES

ACKNOWLEDGEMENTS

I would like to acknowledge Antonio Sánchez, my advisor, for his support and assistance with the work presented here. He is incredibly smart and dedicated and I have learned so much from him. I would also like to acknowledge Juan Lasheras, my co-advisor and the inspiration for this project. Juan is no longer with us unfortunately but his enthusiasm for this project has continued on in many of us.

I would also like to acknowledge Wilfried Coenen, who was my post-doc for a few years and is still a source of guidance. Thank you for everything you have taught me. In addition, I would like to acknowledge all of my past and present labmates and officemates for the many coffee breaks and fun conversations. In particular, I would like to acknowledge Raquel Hakes Weston-Dawkes. She was a great source of support during graduate school and I am truly grateful for her friendship.

I would also like to acknowledge my parents, Doug and Paula, and my sisters, Erika and Christine. They have been my cheerleaders for my entire life. Finally, I would like to acknowledge my partner, Kevin Kohlhase. He is my best friend and I'm so glad to have him in my life.

Chapter 2, in part, is a reprint of the material published in the *Journal of Fluid Mechanics*, titled "On the dispersion of a drug delivered intrathecally in the spinal canal," by J. J. Lawrence, W. Coenen, A. L. Sánchez, G. Pawlak, C. Martínez-Bazán, V. Haughton, and J. C. Lasheras, (2019) 861, 679-720. The dissertation author was the primary investigator and author of this paper. Chapter 2, in part, is also a reprint of the material published in *Applied Mathematical Modelling*, titled "Modelling and direct numerical simulation of flow and solute dispersion in the spinal subarachnoid space," by C. Gutiérrez-Montes, W. Coenen, J. J. Lawrence, C. Martínez-Bazán, A. L. Sánchez, and J. C. Lasheras (2021), 94, 516-533. Cándido Gutiérrez-Montes was the primary author of this paper.

Chapter 3, in part, is a reprint of the material published in the *Journal of Fluid Mechanics*, titled "On the dispersion of a drug delivered intrathecally in the spinal canal," by J. J. Lawrence,

W. Coenen, A. L. Sánchez, G. Pawlak, C. Martínez-Bazán, V. Haughton, and J. C. Lasheras, (2019) 861, 679-720. The dissertation author was the primary investigator and author of this paper. Chapter 3, in part, is also a reprint of the material published in *Applied Mathematical Modelling*, titled “Modelling and direct numerical simulation of flow and solute dispersion in the spinal subarachnoid space,” by C. Gutiérrez-Montes, W. Coenen, J. J. Lawrence, C. Martínez-Bazán, A. L. Sánchez, and J. C. Lasheras (2021), 94, 516-533. Cándido Gutiérrez-Montes was the primary author of this paper.

Chapter 4 is coauthored with W. Coenen, C. Gutiérrez-Montes, and A. L. Sánchez. The dissertation author was the primary author of this chapter. The work presented in chapter 4 was partially supported by the National Science Foundation, grant number 1853954.

Chapter 5 is currently being prepared for submission for publication of the material along with W. Coenen and A. L. Sánchez. The dissertation author was the primary author of this material. The work presented in chapter 5 was partially supported by the National Science Foundation, grant number 1853954.

VITA

2016	B. S. in Chemical Engineering, University of California San Diego
2017	M. S. in Chemical Engineering, University of California San Diego
2021	Ph. D. in Engineering Sciences (Mechanical Engineering), University of California San Diego

PUBLICATIONS

J. J. Lawrence, W. Coenen, A. L. Sánchez, G. Pawlak, C. Martínez-Bazán, V. Haughton, and J. C. Lasheras, “On the dispersion of a drug delivered intrathecally in the spinal canal”, *Journal of Fluid Mechanics*, 861, 679-720, 2019.

C. Guiérrez-Montes, W. Coenen, **J. J. Lawrence**, C. Martínez-Bazán, A. L. Sánchez, and J. C. Lasheras, “Modelling and direct numerical simulation of flow and solute dispersion in the spinal subarachnoid space”, *Applied Mathematical Modelling*, 94, 516-533, 2021.

J. J. Lawrence, W. Coenen, and A. L. Sánchez, “Oscillating flow past a streamwise periodic array of circular cylinders”, *in preparation*.

ABSTRACT OF THE DISSERTATION

Theoretical and Numerical Analyses of Flow and Transport in the Spinal Canal

by

Jenna Joaquin Lawrence

Doctor of Philosophy in Engineering Sciences (Mechanical Engineering)

University of California San Diego, 2021

Professor Antonio Sánchez, Chair

Cerebrospinal fluid (CSF) is a water-like fluid that surrounds the brain and the spinal cord, together known as the central nervous system (CNS). CSF provides a physical cushion for the CNS and also plays an important physiological role by maintaining the electrolytic environment, transporting hormones, circulating nutrients and chemicals filtered from the blood, and removing waste products from cell metabolism of the CNS. It is generally accepted that the absence of CSF circulation may compromise the normal physiological functions of the CNS. CSF circulation also provides a mechanism for the delivery of potent analgesics and chemotherapy to the CNS, a drug delivery procedure often referred to as intrathecal drug delivery (ITDD). Despite significant efforts, most of these processes remain poorly understood.

This dissertation analyzes CSF flow and solute transport along the spinal canal by using asymptotic methods based on the disparity of length and time scales associated with this problem. In addition to the oscillatory flow induced by the cardiac and respiratory cycles, with zero time-averaged velocity at any location, it is found that small corrections associated with the convective acceleration and canal deformation lead to a nonzero steady-streaming velocity. This small steady velocity, together with Stokes drift caused by the non-uniform oscillatory flow, determines the slow time-averaged Lagrangian motion of the CSF, which is found to be responsible for the transport of solutes along the canal. A key outcome of the analysis is a time-averaged transport equation that describes solute dispersion in the long-time scale. The use of this simplified equation circumvents the need to compute concentration fluctuations resulting from the fast oscillatory motion in the short-time scale, drastically reducing the associated computational times. The accuracy and limitations of the time-averaged description are tested by comparison to the results of direct numerical simulations spanning hundreds of oscillation cycles, as needed to generate significant dispersion of the solute. The analysis is extended to study effects of buoyancy-induced motion, arising when the injected solute has a density that differs from that of the CSF. For the small density differences that characterize ITDD drugs, buoyancy is found to have a significant effect on the convective transport, leading to large changes in the resulting solute-dispersion patterns. Finally, the classical problem of oscillatory flow past a circular cylinder is extended to the case of a streamwise periodic array of cylinders, providing insight regarding the effects of spinal-canal micro-anatomical features, such as trabeculae, ligaments, and nerve roots, on the flow and transport in the spinal canal.

Chapter 1

Introduction

1.1 Relevant Physiology

Cerebrospinal fluid (CSF) is the fluid that fills the cranial and spinal subarachnoid spaces as well as the ventricles of the brain, as shown in figure 1.1(b). CSF is a Newtonian fluid with density ρ and viscosity ν similar to those of water at typical body temperatures [5, 48]. The primary functions of CSF are to cushion the brain within the skull, reduce compression on the spinal cord via buoyancy, circulate nutrients filtered from the blood, and remove waste products from cell metabolism of the central nervous system (CNS) [22, 23, 66]. It is generally accepted that the CSF circulation is essential for normal physiological function [90].

CSF is continuously secreted from the blood by the choroid plexus in the ventricles and absorbed at the arachnoid villi [8, 11, 15, 16, 53, 54, 62]. In healthy humans, these two processes are balanced to maintain a constant CSF volume of $\sim 140 - 170$ cm^3, of which ~ 30 cm^3 is contained in the ventricles, $\sim 70 - 80$ cm^3 is contained in the cranial subarachnoid space, and $\sim 40 - 60$ cm^3 is contained in the spinal subarachnoid space. Under normal physiological conditions, the CSF is produced and absorbed at a rate of $\sim 0.3 - 0.4$ cm^3/min so that the entire volume of CSF is replaced every 6-10 hours [16, 33, 52, 63].

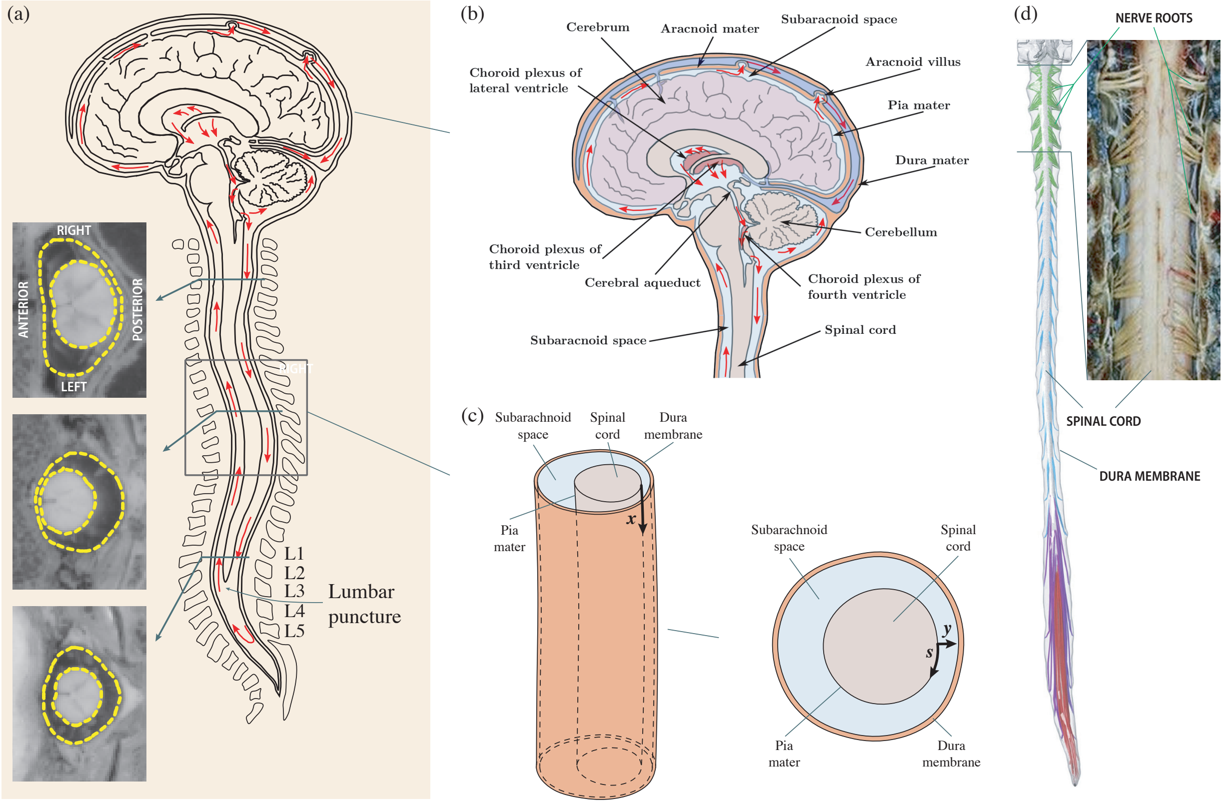

Figure 1.1: Schematic of the spinal canal, showing (a) the overall structure and most common injection route in ITDD, (b) cranial anatomy, (c) simplified spinal canal anatomy, not including smaller features such as nerve roots or trabeculae, showing the coordinate system and (d) the location of the nerve roots along the canal, from [76].

The spinal subarachnoid space (SSAS) is a thin annular canal bound internally by the pia mater and externally by the dura membrane, as indicated in figure 1.1(a) and 1.1(c). Although the shape of the spinal canal is fundamentally slender and slowly varying in healthy humans, patient-to-patient geometrical variability can be sometimes significant; for example, the average canal width in the thoracic region of similarly aged healthy adults with similar stature can range from 2 mm to 4 mm [1, 76]. The geometry of the canal is complicated by the presence of local anatomical features such as nerve roots, which are depicted in figure 1.1(d). Additional local modifications of the geometry are associated with certain injuries and conditions. For example, patients with a type 1 Chiari malformation (CM1) are prone to develop syringomyelia, a pathology characterized by the formation of a cyst or syrinx in the central canal of the spinal cord [46]. The latter can lead to a partial obstruction of the surrounding SSAS with detrimental consequences such as weakness or even loss of sensitivity in arms and legs. It has been hypothesized that there is a link between an anomalous CSF flow caused by the CM1 and the formation and growth of the syrinx [81].

1.2 Flow in the Spinal Canal

1.2.1 In-Vivo Observations

A major feature of cerebrospinal fluid flow is its oscillation, which is driven mainly by the intracranial pressure fluctuations that occur with each heart beat as a result of the cyclic variation of the cerebrovascular blood volume [3, 21]. As follows from conservation of intracranial volume, sometimes referred to as the Monro-Kellie doctrine or hypothesis [56], this pressure fluctuation drives CSF periodically into and out of the compliant spinal canal [21]. The oscillating CSF flow is accommodated by the compression of the veins and fatty tissue in the epidural space that surrounds the dural sac. The compliance of the canal is limited, with the result that the tidal volume of CSF flowing across the foramen magnum from the cranial vault into the SSAS during each cardiac cycle is approximately $\Delta V = 1 - 2$ cm^3 [46], corresponding to a small fraction (2% to 3%) of the total CSF volume $V \simeq 40 - 60$ cm^3 contained inside the spinal canal. As a consequence, the stroke length of the fluctuating motion is just a few centimeters, resulting in velocities that are of the order of a few centimeters per second in the cervical region, progressively diminishing along the canal to reach much smaller values in the lumbar region.

In addition to this oscillatory flow, it has been known since the early radiological observations of DiChiro [17] that the CSF exhibits a slow bulk motion with characteristic velocities of the order of 1 centimeter per minute, much smaller than those of the periodic fluctuating flow, and corresponding characteristic residence times of the order of 30 minutes, much longer than the period of the oscillating motion (about 1 second). He also showed the rapid migration of the compound injected in the brain ventricles downwards into the spinal canal [18, 19]. These findings, later corroborated by several radiological studies [23, 44], support the idea that there must be an active circulation mechanism associated with the overall movement of CSF.

1.2.2 Recent Theoretical and Numerical Efforts

The slow bulk motion of CSF in the SSAS is theorized to be the result of a steady-streaming phenomenon, presented in detail in a recent publication [75]. The analysis models the SSAS as a slowly varying annular canal with limited compliance, measured by a small parameter $\varepsilon \sim \Delta V/V \sim 1/50$. The oscillatory motion is determined in the first approximation by a linear unsteady lubrication problem. The nonlinear terms associated with the convective acceleration and canal deformation produce a small velocity correction with a steady component, which is commonly referred to as steady-streaming [74]. The resulting magnitude of this steady velocity is a factor ε smaller than that of the oscillatory flow, consistent with experimental observations. Recent numerical computations with anatomically correct geometries have verified the existence of steady streaming [37] and show increased amounts of steady streaming resulting from the presence of nerve roots in the cervical region. Steady streaming in the SSAS was also identified in earlier work in connection with the presence of the catheter used to infuse the drug [6, 59].

Besides the steady-streaming component of the Eulerian velocity field, there are a number of additional transport mechanisms that may contribute to the dispersion of the drug along the spinal canal. For example, an analysis of viscous oscillating flow near a wavy wall showed that the Lagrangian mean motion of an oscillating fluid particle may contain a contribution arising from Stokes drift [41]. This is a purely kinematic effect associated with the spatial nonuniformity of the pulsatile flow. In the presence of a velocity gradient, a fluid particle subject to an oscillating velocity field experiences small velocity variations, so that it does not return to its initial position at the end of each cycle. The small cyclical displacements accumulate in time, leading to a long-term motion known as Stokes drift, with associated velocities that are comparable to those of steady streaming [41].

Another mechanism that has been postulated to be relevant to drug dispersion in the SSAS is the enhancement of the streamwise transport rate arising from the coupling of the velocity shear with the transverse diffusion [46], a phenomenon known as Taylor dispersion [85]. Taylor dispersion, described theoretically for oscillatory flow in a pipe by Watson [89], is particularly effective in gaseous flow, for which the molecular diffusivity of the solute κ is comparable to the kinematic viscosity of the carrier fluid ν (i.e. values of the Schmidt number $S = \nu/\kappa \sim 1$). For example, Taylor dispersion is known to play an important role in the transport of oxygen and carbon dioxide in the lung airways during pulmonary high-frequency ventilation [24], involving high-frequency oscillatory flows with small tidal volumes. The effects of Taylor dispersion in solute transport in liquids are necessarily limited by the smaller solute diffusivities. Although the resulting effective diffusion velocities along the spine have been estimated to be negligibly small [75], more work is necessary to quantify diffusion enhancement stemming from the presence of micro-anatomical features [46].

The existence of two markedly different time scales (i.e. a period of oscillation of about 1 second and a residence time of about 30 minutes) hinders computational efforts, limiting their long-time predictive capability and their potential for providing understanding of the specific physical mechanisms that determine the drug-dispersion rate along the spinal canal. In particular, since solute transport in oscillatory flow is associated with nonlinear mechanisms (e.g. steady streaming, Stokes drift, and Taylor dispersion) that have an accumulative effect over many cycles, computational analyses based on numerical integrations over a finite number of cycles are not well suited for investigating drug dispersion. Despite these inherent limitations, previous numerical analyses have helped understand local aspects of the problem. Many of the previous numerical studies of CSF flow and solute transport have been based on modeling of short segments of the SSAS. Most of these investigations consider rigid walls and open input and output cross sections, with boundary velocity profiles adjusted to satisfy some radiological measurements [39]. The effect of deformable walls has been included in some simulations [46], which have been recently extended to patient-specific 3D models of the anatomy of the canal. Some of these computational studies also include modeling of pharmacokinetics parameters such as drug enzymatic decay, tissue uptake, and clearance by the blood [65, 82].

1.3 Intrathecal Drug Delivery

The treatment of a number of CNS pathologies, including some cancers of the CNS, and management of severe chronic and post-operative pain sometimes involves the direct injection of medication into the CSF. This procedure, used since the early 1980s [61], is often referred to as intrathecal drug delivery (ITDD). The standard ITDD protocol consists of placing a small catheter in the SSAS of the lumbar region to continuously pump the drug or to release a finite dose at selected times. Sometimes ITDD is used to deliver the drug to sites along the spinal cord close to the location of injection, while in other cases the medication is delivered to distant target sites in the brain. The most easily accessed and most commonly used injection route is a puncture in the posterior spine in the lumbar area, typically using the L3/L4 intervertebral space indicated in figure 1.1(a).

ITDD allows for the use of potent analgesic drugs that cannot be administered systemically because of metabolic or other biochemical reasons, an example being ziconoide, an analgesic agent for the amelioration of severe and chronic pain [7, 26, 38, 40, 59, 64]. More importantly, as compared to systemic drug delivery methods, such as oral, transdermal, or intravenous delivery, ITDD reduces the amount of medication needed to treat a given condition by a factor as large as 300, thereby drastically diminishing life-threatening side effects [51]. It is also useful to treat cases of CSF infection (e.g. meningitis) that require direct and prompt antibiotic therapy [71]. In addition, ITDD is used to bypass the blood-brain barrier in treatments of certain cancers that have reached the CNS, including some types of lymphoma, medulloblastoma, oligodendroglioma, and intracranial germ-cell tumors [43]. As in the case of pain and antibiotic medication, the advantage of ITDD chemotherapy is to maximize CNS exposure to the drug while reducing or even eliminating systemic drug toxicity as compared with intravenous or oral delivery.

Although ITDD is currently used with satisfactory results, the drug dispersion rate is rather unpredictable and exhibits dependences that are not thoroughly understood. For instance, it has been shown that doubling the heart rate causes a 26.4% decrease in intrathecal drug concentration at the injection site due to a faster drug dispersion rate along the canal [29]. It has also been shown that doubling the stroke volume of CSF across the foramen magnum may decrease intrathecal drug concentration at the injection site up to 38% [10]. Patient posture and amplitude of the intracranial pressure have also been shown to affect the motion of the CSF and the dispersion of the drug in the spinal canal [77].

Typical intrathecal drug densities are similar to that of the CSF, with density differences in the range of 1/1000 to 1/100 [48, 60]. In spinal anaesthesia, it is common to use the term baricity to refer to the relative density of the anaesthetic to the CSF. Hyperbaric means that the anaesthetic is more dense than the CSF, hypobaric means that the anaesthetic is less dense than the CSF, and isobaric means that the anaesthetic is the same density as the CSF. Barker was the first to use dextrose as a method of increasing the baricity to better control the spread of intrathecal anesthetics [2]. More recent findings have shown that for a hyperbaric solution, injection while the patient is seated for some time before moving to a supine position leads to an inital restriction in the transport of the anaesthesia; however, given enough time in the supine position, the injection position is irrelevant [55, 67, 87]. For a hypobaric solution, the sitting injection position leads to more cephalad spread of the anaesthesia as compared to a lateral injection position [72]. Baricity has no effect when injection occurs in the lateral position [25]. Positioning has no effect on an isobaric solution [91]. Experimental evidence is clear that the density of the injected drug and the position of the patient during injection both have an effect on the spread of the drug.

The limited predictive capability of drug-delivery rates to targeted locations, resulting from a lack of a clear understanding of the complex convective and diffusive mechanisms controlling the transport of the drug, may result in unexpected complications that cannot be explained by current knowledge of pharmacokinetics [35, 63]. Recent studies have revealed inexplicable variations in patient response, which may be attributed to differences in the physical and molecular characteristics of the injected solution, and more importantly, to the patient physiological parameters and specific anatomy and characteristics of the spinal canal. Inadvertent over- or under-dosage may result in serious clinical consequences. Under-dosage may occur in 30% or more of patients receiving standard regimes of chemotherapy and those who are inadvertently under-dosed are at risk of a significantly reduced anticancer effect, with an estimated 20% relative reduction in survival rate [88]. In addition, over-dosing with anesthetic via ITDD may produce serious consequences including acute nerve damage or chronic subclinical nerve damage [9]. Thus, there is an imperative need to develop a methodology capable of accurately predicting the dispersion of the drug along the spinal canal for the specific anatomy and physiological conditions of the individual patient as well as for the molecular characteristics and injection rate of the drug.

1.4 Microanatomy in the Spinal Canal

The spinal canal is not an open channel, as modeled in previous work [75], but rather contains a number of features that may affect the flow of cerebrospinal fluid and transport of intrathecal drugs. Figure 1.1(d) shows an anatomical image of the nerve roots in the spinal canal, approximately cylindrical objects branching off the spinal cord to deliver nerve signals to the rest of the body, along with a 3D model of the SSAS including nerve roots from a recent publication [76]. In addition to the nerve roots, the SSAS contains trabeculae and denticulate ligaments which provide structure to the spinal canal and hold the spinal cord in place [57, 86].

Cerebrospinal fluid flow in the spinal canal is oscillatory, which in the presence of obstacles is known to produce a small steady velocity component known as steady streaming. A detailed formulation of steady streaming about a single cylinder for small oscillation amplitudes finds both inner and outer streaming vortices [27]. A comprehensive regime diagram describing how the streaming patterns depend on the governing dimensionless parameters shows that there are at least four streaming regimes for a single simple object [12]. In general, steady streaming about an obstacle depends on the oscillation amplitude s, the typical size of the object a, the oscillation frequency ω, and the kinematic viscosity of the fluid ν. These quantities lead to the definition of the Womersley number $M = a/(\nu/\omega)^{1/2}$, which represents the inertial forces due to oscillation as compared to the viscous forces caused by the cylinder, and the dimensionless oscillation amplitude $\varepsilon = s/a$.

Steady streaming about multiple objects has also been studied. Numerical and experimental results for steady streaming about a pair of cylinders are shown in a recent publication [12]. Steady streaming is also utilized frequently in microfluidics, in which large arrays of cylinders or other simple objects cause steady circulatory flow patterns that are used to trap particles for imaging without direct contact [28, 45, 50]. In microfluidics, the cylinders and other objects used are not semi-infinite, as in the aforementioned works, but rather confined axially which induces additional streaming patterns, as shown in some recent experiments [49, 68].

Several groups, using full direct numerical simulations, have studied the effect of microanatomical features in the spinal canal on local mixing, steady streaming, and transport. Some find that the presence of the nerve roots enhances steady-streaming and therefore improves the transport [37], while others directly show an increase in the transport of solutes due to the nerve roots [79, 80]. An increase in drug dispersion due to the mixing patterns caused by the trabeculae has also been found [83]. There is a clear need for detailed study of steady streaming past objects in the spinal canal using classical steady-streaming methodologies.

1.5 Organization of Thesis

There are seven chapters in this thesis which are organized as follows.

The first (current) chapter describes typical healthy anatomy of the central nervous system, focusing on cerebrospinal fluid and the spinal canal. Observations of cerebrospinal fluid motion are explained as well as the use of cerebrospinal fluid motion in intrathecal drug delivery. The observed effects of drug density and patient positioning are also listed. Finally, a brief overview of spinal microanatomy and its theorized effects on drug dispersion is presented.

The second chapter studies fluid motion in a thin annular canal with an elastic outer wall as a model of cerebrospinal fluid motion in the spinal canal. The driving force of the flow is the oscillatory pressure in the cranial cavity, simplified here to be a cosine function. The elasticity of the outer wall is small, such that the tidal volume in and out of the canal with each oscillation is small compared to the total volume of cerebrospinal fluid in the canal. An asympototic analysis is performed to determine the leading-order flow, which models the short-term oscillations, and the steady-streaming flow, which models the long-term bulk motion. Lagrangian velocity components are then found, which include both steady streaming and Stokes drift components. Results are presented for a simplified geometry and then validated by comparison to full three-dimensional direct numerical simulations.

The third chapter uses the velocity field results from the previous chapter to investigate the dispersion of a solute with the same density as the cerebrospinal fluid in the given flow. Several distinguished limits of the Schmidt number, a dimensionless quantity that compares the momentum diffusivity to the molecular diffusivity, are found in an order of magnitude analysis, leading to different governing behaviors. Results are presented for a range of Schmidt numbers for two geometries of interest. Again the results of the more simple asymptotic analysis are validated by comparison to full three-dimensional direct numerical simulations.

The fourth chapter analyzes the transport for a solute with a density different from that of the cerebrospinal fluid. The momentum and transport equations are now coupled, so the buoyancy-induced velocity, a component of the Lagrangian velocity, varies with time. The same distinguished limits of the Schmidt number appear, now with the inclusion of the Richardson number to describe the effects of buoyancy as compared to the effects of convection. Results are presented for the intermediate limit of Schmidt numbers and both positive and negative Richardson numbers. The analysis is validated by comparison to full three-dimensional direct numerical simulations.

The fifth chapter studies oscillatory flow past a streamwise periodic array of circular cylinders as a simplified model of the nerve roots in the spinal canal. Asymptotic analysis is performed in the distinguished limit of small oscillation amplitude and Womersley number of order unity. Similar to chapter 2, the Eulerian velocity field contains a small steady correction term known as steady streaming and the Lagrangian velocity field contains an additional component due to Stokes drift. Transport of a solute is also briefly studied.

The sixth chapter suggests three areas of future work. The first suggestion is an extension of the velocity field for a general intracranial pressure signal. The necessary equations are all presented and it is suggested that this analysis is performed for a typical three peak intracranial pressure signal. Second, the flow in the spinal canal driven by respiratory effects along the canal should also be investigated. Equations are presented, but the calculations and analysis remain to be completed. Lastly, it is suggested that the transport of small particles is analyzed. The effect of the Stokes number, which may be significant depending on the size or density of the particle, as well as the effect of other body forces such as magnetism, are recommended areas of study.

Chapter 2

Flow in the Spinal Canal

2.1 Characteristic Scales

CSF is an incompressible, Newtonian fluid with density ρ and kinematic viscosity ν similar to those of water at body temperature. It fills the subarachnoid space of the spinal canal, a thin annular gap surrounding the spinal cord bounded internally by the pia mater and externally by the deformable dura membrane, as indicated in figure 1.1(c). The spinal canal is doubly slender, in that its length $L \sim 60-80$ cm, characteristic perimeter $\ell_c \sim 2$ cm, and characteristic width $h_c \sim 0.1$ cm satisfy the inequalities

$$L \gg \ell_c \gg h_c. \tag{2.1}$$

The associated total volume of CSF in the spinal canal is of the order of $V \sim L\ell_c h_c \sim 40-60$ cm^3.

The fluctuating motion of CSF in and out of the spinal canal is associated with the periodic variation of the intracranial pressure, driven by the pulsating blood flow in the rigid cranial vault, of angular frequency ω. In addition to the pulsation associated with the arterial blood flow, it has been observed in several radiological studies [20, 36] that respiration produces a modulation of the intracranial pressure, resulting in an additional oscillation of the CSF in the spinal canal at a lower frequency (12 to 18 cycles per minute in adults). For simplicity and reduced complexity of the algebraic manipulations, our analysis assumes the cranial pressure to be a periodic function with angular frequency ω, equal to that of that of the cardiac cycle. Section 6.1 shows an extension of the following analysis for a general periodic pressure signal with multiple associated frequencies.

In the following development, the periodic pressure fluctuation in the cranial cavity is written as $(\Delta p)_c\Pi(t)$, where $(\Delta p)_c$ is the amplitude and $\Pi(t)$ is a dimensionless periodic function. The resulting volume flux is accommodated by the deformation of the dura membrane. For simplicity, the displacement of the dura membrane is assumed to be linearly proportional to the local pressure fluctuation, with a compliance factor γ' whose characteristic value $\gamma'_c \ll h_c/(\Delta p)_c$ defines the small parameter

$$\varepsilon = \frac{\gamma'_c}{h_c/(\Delta p)_c} \tag{2.2}$$

measuring the limited compliance of the canal as well as the small oscillatory displacements of the CSF in the canal.

Because of the limited compliance of the spinal canal, the tidal volume that is displaced along the canal during each cardiac cycle, $\Delta V \simeq \varepsilon V \simeq 1-2$ cm^3, is much smaller than V. Correspondingly, the periodic flow involves axial displacements of order εL in times of order ω^{-1}, resulting in streamwise velocities of the CSF with characteristic values $u_c = \varepsilon\omega L$ of the order of a few cm/s near the entrance, progressively decaying along the canal to vanish at its closed-end sacral region. The corresponding characteristic values of the azimuthal $w_c = \varepsilon\omega\ell_c$ and transverse $v_c = \varepsilon\omega h_c$ velocities are much smaller, a consequence of the slenderness of the canal.

The slenderness of the flow is accounted for in defining a non-dimensional curvilinear coordinate system (x,y,s), with x measuring the distance from the entrance scaled with L, y measuring the transverse distance from the pia mater scaled with h_c, and s measuring the azimuthal distance, normalized with the local perimeter (see figure 1.1(c) for an indication of the coordinate system). The corresponding non-dimensional velocity components (u,v,w) are scaled with the characteristic velocities (u_c,v_c,w_c) in the longitudinal, transverse and azimuthal directions respectively. The time is scaled with the period of the angular frequency ω^{-1} to give the dimensionless variable t. Correspondingly, the velocity is 2π periodic in t. The shape of the canal is described by the dimensionless inner perimeter $\ell(x)$ (scaled with l_c) and the width distribution $h(x,s,t)$ (scaled with h_c). The deformation of the dura membrane leads to small changes of the canal width $h = \bar{h}(x,s) + \varepsilon h'(x,s,t)$, where $\bar{h}$ is the unperturbed canal width and $h'(x,s,t)$ measures the time-dependent radial deformation, such that the transverse velocity satisfies $v = \partial h'/\partial t$ at $y = h$.

A straightforward order-of-magnitude analysis of the momentum conservation equation reveals the main characteristics of CSF flow in the SSAS. The Strouhal number, measuring the relative importance of the local acceleration and the convective acceleration, is $\omega L/u_c = \omega l_c/w_c = \omega h_c/v_c = \varepsilon^{-1} \gg 1$, so that effects of inertia are small. The viscous time across the canal, h_c^2/ν, is of order ω^{-1}, yielding order-unity values of the Womersley number $\alpha = h_c/(\nu/\omega)^{1/2} \sim 1$, with α^2 measuring the ratio of the local acceleration to the viscous forces. In the first approximation, therefore, the local acceleration balances the pressure and viscous forces, resulting in a linear unsteady lubrication problem with zero time-averaged velocity at any given point. The convective acceleration introduces a small relative correction of order ε to this oscillatory lubrication velocity. Because of the nonlinear nature of the inertial terms, this velocity correction, of order $\varepsilon u_c = \varepsilon^2 \omega L$ in the axial direction, includes a steady component known as steady streaming [74].

The problem can be simplified in the slender-flow approximation (2.1) by consistently neglecting terms of order $(\ell_c/L)^2$ and $(h_c/L)^2$ when writing the conservation equations. Furthermore, to account for the deformation of the dura membrane and the resulting variable geometry, the distance to the pia mater is normalized with the local instantaneous width $h(x,s,t)$ to give the alternative transverse coordinate $\eta = y/h$.

2.2 Eulerian Velocity Field

This section summarizes the results of the analysis presented in [75] for the motion of CSF in the spinal canal, which was generalized slightly in [42]. In dimensionless form, the constitutive equation becomes

$$h - \bar{h} = \varepsilon \gamma p \qquad \Rightarrow \qquad h' = \gamma(\Pi + k^2 p') \tag{2.3}$$

involving the canal deformation $h - \bar{h} = \varepsilon h'$ from its unperturbed distribution $\bar{h}(x,s)$ and the streamwise pressure distribution $p - \Pi(t) = k^2 p'(x,t)$, where $p'(x,t)$ is the pressure variation from its entrance value scaled with $\rho \varepsilon \omega^2 L^2$ and

$$k = \frac{L\omega}{[(h_c/\gamma'_c)/\rho]^{1/2}} \tag{2.4}$$

is a dimensionless wave number, with $[(h_c/\gamma'_c)/\rho]^{1/2}$ representing the relevant elastic wave speed. In the original analysis [75], the compliance function $\gamma = \gamma'/\gamma'_c$, of order unity, was assumed to be only a function of x, resulting in deformations h' that were a function of x and t. The description is generalized in [42] by allowing for a more general variation $\gamma(x,s)$, so that $h'(x,s,t)$.

The pressure is taken to be the sum of two separate pressure functions p' and $\hat{p}$, where $p'(x,t)$ describes the streamwise pressure distribution, dependent only on the streamwise coordinate due to the slenderness of the flow, and a supplementary function $\hat{p}(x,s,t)$ introduced in the azimuthal component of the momentum equation (2.7) to describe the small relative pressure variations occurring within each cross-section, of order $(\ell_c/L) \ll 1$. Since $\hat{p}(x,s,t)$ is much smaller than $p'(x,t)$, it is neglected in the constitutive relation (2.3) and the streamwise momentum equation (2.6).

In the slender-flow limit (2.1), the continuity equation takes the form

$$\frac{1}{\ell}\frac{\partial}{\partial x}(\ell u) + \frac{\partial v}{\partial y} + \frac{1}{\ell}\frac{\partial w}{\partial s} = 0, \tag{2.5}$$

whereas the axial and azimuthal components of the momentum equation are

$$\frac{\partial u}{\partial t}+\varepsilon\left[\frac{1}{\ell}\frac{\partial}{\partial x}(\ell u^2)+\frac{\partial}{\partial y}(uv)+\frac{1}{\ell}\frac{\partial}{\partial s}(uw)\right] = -\frac{\partial p'}{\partial x}+\frac{1}{\alpha^2}\frac{\partial^2 u}{\partial y^2} \tag{2.6}$$

$$\frac{\partial w}{\partial t}+\varepsilon\left[\frac{\partial}{\partial x}(uw)+2\frac{uw}{\ell}\frac{\partial \ell}{\partial x}+\frac{\partial}{\partial y}(vw)+\frac{1}{\ell}\frac{\partial}{\partial s}(w^2)\right] = -\frac{1}{\ell}\frac{\partial \hat{p}}{\partial s}+\frac{1}{\alpha^2}\frac{\partial^2 w}{\partial y^2}, \tag{2.7}$$

where

$$\alpha=\frac{h_c}{(\nu/\omega)^{1/2}} \tag{2.8}$$

is the Womersley number, which takes values of order unity.

The pressure drop is negligible at the entrance of the canal, corresponding to the condition $p'=0$ at $x=0$. The velocity satisfies $u=v=w=0$ at $y=0$ and $u=v-\partial h'/\partial t=w=0$ at $y=h$. Since the canal is symmetric, the azimuthal velocity component w vanishes at $s=0$ and $s=1$. The requirement that the axial volume flux $\int_0^1\left(\int_0^h u\mathrm{d}y\right)\mathrm{d}s$ must vanish at the closed end $x=1$ completes the set of boundary conditions needed to determine the flow in the canal.

For computational purposes, it is convenient to introduce the normalized transverse coordinate $\eta=y/h$, so that the outer boundary occurs at the stationary location $\eta=1$ rather than the moving boundary $y=h(x,s,t)$. Although the boundary condition becomes simpler, the change of variables to η leads to more complicated equations. In the following, equations may be given in y or η.

Solution of the problem described by (2.3) and (2.5)–(2.7) is completed by introducing regular expansions in powers of ε for the velocity, canal deformation, and pressure functions. The first two terms in the expansions are solved below for an intracranial pressure of the form $\Pi(t)=\cos t$. Additional terms in a Fourier expansion for $\Pi(t)$ could be computed in a similar manner, thereby enabling the extension of the analysis to general non-harmonic periodic functions $\Pi(t)$, shown in detail in section 6.1.

2.2.1 Leading-order Solution

In the limit $\varepsilon \ll 1$ with $\alpha \sim 1$ and $k \sim 1$, the problem defined by (2.3) and (2.5)–(2.7) with the boundary conditions given below (2.7) can be solved in terms of regular expansions of the form

$$\begin{aligned} & u = u_0 + \varepsilon u_1 + \cdots, v = v_0 + \varepsilon v_1 + \cdots, w = w_0 + \varepsilon w_1 + \cdots, \\ & h' = h'_0 + \varepsilon h'_1 + \cdots, p' = p'_0 + \varepsilon p'_1 + \cdots, \hat{p} = \hat{p}_0 + \varepsilon \hat{p}_1 + \cdots. \end{aligned} \tag{2.9}$$

At leading order, (2.3) and (2.5)–(2.7) take the linear form

$$h'_0 = \gamma(\Pi + k^2 p'_0) \tag{2.10}$$

$$0 = \frac{1}{\ell}\frac{\partial}{\partial x}(\ell u_0) - \frac{\partial \bar{h}}{\partial x}\frac{\eta}{\bar{h}}\frac{\partial u_0}{\partial \eta} + \frac{1}{\bar{h}}\frac{\partial v_0}{\partial \eta} + \frac{1}{\ell}\frac{\partial w_0}{\partial s} - \frac{1}{\ell}\frac{\partial \bar{h}}{\partial s}\frac{\eta}{\bar{h}}\frac{\partial w_0}{\partial \eta} \tag{2.11}$$

$$\frac{\partial u_0}{\partial t} = -\frac{\partial p'_0}{\partial x} + \frac{1}{\alpha^2}\frac{\partial^2 u_0}{\partial y^2} \tag{2.12}$$

$$\frac{\partial w_0}{\partial t} = -\frac{1}{\ell}\frac{\partial \hat{p}_0}{\partial s} + \frac{1}{\alpha^2}\frac{\partial^2 w_0}{\partial y^2}, \tag{2.13}$$

for which the variables can be written in the form

$$\begin{aligned} u_0 &= \mathrm{Re}\left(\mathrm{i}e^{\mathrm{i}t}U\right), v_0 = \mathrm{Re}\left(\mathrm{i}e^{\mathrm{i}t}V\right), w_0 = \mathrm{Re}\left(\mathrm{i}e^{\mathrm{i}t}W\right), \\ p'_0 &= \mathrm{Re}\left(e^{\mathrm{i}t}P'\right), \hat{p}_0 = \mathrm{Re}\left(e^{\mathrm{i}t}\hat{P}\right), h'_0 = \mathrm{Re}\left(e^{\mathrm{i}t}H'\right), \end{aligned} \tag{2.14}$$

involving the complex functions $U(x,\eta,s)$, $V(x,\eta,s)$, $W(x,\eta,s)$, $P'(x)$, $\hat{P}(x,s)$, and $H'(x,s)$, to be defined below.

The axial and azimuthal velocities are given in terms of the components of the pressure gradient by

$$U = \frac{\mathrm{d}P'}{\mathrm{d}x}G \quad \text{and} \quad W = \frac{1}{\ell}\frac{\partial \hat{P}}{\partial s}G \tag{2.15}$$

with

$$G(x,\eta,s) = 1 - \frac{\cosh\left[\frac{\alpha\bar{h}}{2}\frac{1+\mathrm{i}}{\sqrt{2}}(2\eta-1)\right]}{\cosh\left[\frac{\alpha\bar{h}}{2}\frac{1+\mathrm{i}}{\sqrt{2}}\right]} \tag{2.16}$$

as follows at this order by integration of (2.6) and (2.7) with boundary conditions $u_0 = w_0 = 0$ at $\eta = (0,1)$. The transverse velocity can be evaluated by integrating (2.5) with the condition $v_0 = 0$ at $\eta = 0$ to give

$$V = -\frac{1}{\ell}\frac{\partial}{\partial x}\left(\ell\frac{\mathrm{d}P'}{\mathrm{d}x}\bar{h}\int_0^\eta G\mathrm{d}\eta\right) - \frac{1}{\ell}\frac{\partial}{\partial s}\left(\frac{1}{\ell}\frac{\partial\hat{P}}{\partial s}\bar{h}\int_0^\eta G\mathrm{d}\eta\right) + \frac{\partial\bar{h}}{\partial x}\frac{\mathrm{d}P'}{\mathrm{d}x}\eta G + \frac{1}{\ell}\frac{\partial\bar{h}}{\partial s}\frac{1}{\ell}\frac{\partial\hat{P}}{\partial s}\eta G \tag{2.17}$$

where

$$\bar{h}\int_0^\eta G\mathrm{d}\eta = \bar{h}\eta - \frac{1-\mathrm{i}}{\sqrt{2}\alpha}\frac{\sinh\left[\frac{\alpha\bar{h}}{2}\frac{1+\mathrm{i}}{\sqrt{2}}(2\eta-1)\right] + \sinh\left[\frac{\alpha\bar{h}}{2}\frac{1+\mathrm{i}}{\sqrt{2}}\right]}{\cosh\left[\frac{\alpha\bar{h}}{2}\frac{1+\mathrm{i}}{\sqrt{2}}\right]}. \tag{2.18}$$

Evaluating (2.17) at $\eta = 1$, where $V = H'$ as corresponds to $v_0 = \partial h_0'/\partial t$, gives

$$H' + \frac{1}{\ell}\frac{\partial}{\partial x}\left(\ell\frac{\mathrm{d}P'}{\mathrm{d}x}q(x,s)\right) + \frac{1}{\ell}\frac{\partial}{\partial s}\left[\frac{1}{\ell}\frac{\partial\hat{P}}{\partial s}q(x,s)\right] = 0, \tag{2.19}$$

with

$$q(x,s) = \bar{h}\int_0^1 G\mathrm{d}\eta = \bar{h} - \frac{\sqrt{2}(1-\mathrm{i})}{\alpha}\tanh\left(\frac{\alpha\bar{h}}{2}\frac{1+\mathrm{i}}{\sqrt{2}}\right) \tag{2.20}$$

and

$$H' = \gamma(1 + k^2P'), \tag{2.21}$$

the latter derived from (2.10). Integrating (2.19) around the canal section with $\partial\hat{P}/\partial s = 0$ at $s = 0$, consistent with the symmetry condition $w_0 = 0$ at $s = 0$, yields

$$\frac{q}{\ell^2}\frac{\partial\hat{P}}{\partial s} + \frac{1}{\ell}\frac{\mathrm{d}}{\mathrm{d}x}\left[\ell\int_0^s q\mathrm{d}\tilde{s}\frac{\mathrm{d}P'}{\mathrm{d}x}\right] + \left(\int_0^s \gamma\mathrm{d}\tilde{s}\right)(k^2P'+1) = 0. \tag{2.22}$$

Evaluating the last equation at $s = 1$, where $\partial\hat{P}/\partial s = 0$, finally yields the problem

$$\frac{1}{\ell}\frac{\mathrm{d}}{\mathrm{d}x}\left[\ell Q\frac{\mathrm{d}P'}{\mathrm{d}x}\right] + \left(\int_0^1 \gamma \mathrm{d}s\right)(k^2P'+1) = 0; \begin{cases} P' = 0 & \text{at} \quad x = 0 \\ \frac{\mathrm{d}P'}{\mathrm{d}x} = 0 & \text{at} \quad x = 1 \end{cases}, \tag{2.23}$$

involving the average section compliance $\int_0^1 \gamma \mathrm{d}s$ and the volume-flux function

$$Q(x) = \int_0^1 q\mathrm{d}s = \int_0^1 \left[\bar{h} - \frac{\sqrt{2}(1-\mathrm{i})}{\alpha}\tanh\left(\frac{\alpha\bar{h}}{2}\frac{1+\mathrm{i}}{\sqrt{2}}\right)\right]\mathrm{d}s. \tag{2.24}$$

For given values of $\gamma(x,s)$, $\bar{h}(x,s)$, and $\ell(x)$, the integration of (2.23) determines $P'(x)$, which can be used in (2.15) and (2.19) to evaluate U and H'. The associated azimuthal pressure gradient $\partial\hat{P}/\partial s$, determined from (2.22), is needed to evaluate the functions W and V from (2.15) and (2.17), thereby completing the description of the harmonic solution (2.14). The solution simplifies when the average section compliance γ and the shape of the canal section $\bar{h}$ are independent of x. For $\int_0^1 \gamma \mathrm{d}s = 1$, $\ell = 1$, and $\bar{h} = \bar{h}(s)$, Q is a constant and integration of (2.23) yields

$$P' = \frac{1}{k^2}\left\{\frac{\cos[k(1-x)/\sqrt{Q}]}{\cos(k/\sqrt{Q})} - 1\right\}. \tag{2.25}$$

2.2.2 Steady Streaming

Because of the nonlinear interactions associated with the convective terms and canal deformation, first-order corrections to the flow contain a steady component in addition to the oscillatory component. The computation of this steady-streaming flow begins by collecting terms of order ε in (2.6) and (2.7). Taking the time average $\langle\cdot\rangle = \frac{1}{2\pi}\int_0^{2\pi}\cdot\,\mathrm{d}t$ of the resulting equations yields

$$\begin{aligned}
\mathcal{F} &= \frac{1}{\ell}\frac{\partial}{\partial x}(\ell\bar{h}\langle u_1\rangle) - \frac{\partial}{\partial\eta}\left(\eta\frac{\partial\bar{h}}{\partial x}\langle u_1\rangle\right) + \frac{\partial\langle v_1\rangle}{\partial\eta} + \frac{1}{\ell}\frac{\partial}{\partial s}(\bar{h}\langle w_1\rangle) - \frac{\partial}{\partial\eta}\left(\frac{\eta}{\ell}\frac{\partial\bar{h}}{\partial s}\langle w_1\rangle\right) \quad (2.26)\\
\mathcal{F}_x &= -\frac{\partial\langle p_1'\rangle}{\partial x} + \frac{1}{\bar{h}^2\alpha^2}\frac{\partial^2\langle u_1\rangle}{\partial\eta^2} \quad (2.27)\\
\mathcal{F}_s &= -\frac{1}{\ell}\frac{\partial\langle\hat{p}_1\rangle}{\partial s} + \frac{1}{\bar{h}^2\alpha^2}\frac{\partial^2\langle w_1\rangle}{\partial\eta^2}, \quad (2.28)
\end{aligned}$$

where

$$\mathcal{F} = -\frac{1}{\ell}\frac{\partial}{\partial x}(\ell\langle h_0'u_0\rangle) + \frac{\partial}{\partial\eta}\left(\eta\langle u_0\frac{\partial h_0'}{\partial x}\rangle\right) - \frac{1}{\ell}\frac{\partial}{\partial s}(\langle h_0'w_0\rangle) + \frac{\partial}{\partial\eta}\left(\frac{\eta}{\ell}\langle w_0\frac{\partial h_0'}{\partial s}\rangle\right), \quad (2.29)$$

$$\begin{aligned}
\mathcal{F}_x &= \frac{1}{\ell}\frac{\partial}{\partial x}(\ell\langle u_0^2\rangle) + \frac{1}{\bar{h}}\frac{\partial}{\partial\eta}\langle u_0v_0\rangle + \frac{1}{\ell}\frac{\partial}{\partial s}\langle u_0w_0\rangle\\
&- \frac{\eta}{\bar{h}}\frac{\partial}{\partial\eta}\langle\frac{\partial h_0'}{\partial t}u_0\rangle - \frac{\partial\bar{h}}{\partial x}\frac{\eta}{\bar{h}}\frac{\partial}{\partial\eta}\langle u_0^2\rangle - \frac{1}{\ell}\frac{\partial\bar{h}}{\partial s}\frac{\eta}{\bar{h}}\frac{\partial}{\partial\eta}\langle u_0w_0\rangle + \frac{2}{\bar{h}^3\alpha^2}\frac{\partial^2}{\partial\eta^2}\langle h_0'u_0\rangle, \quad (2.30)
\end{aligned}$$

$$\begin{aligned}
\mathcal{F}_s &= \frac{\partial}{\partial x}\langle u_0w_0\rangle + 2\frac{\langle u_0w_0\rangle}{\ell}\frac{\partial\ell}{\partial x} + \frac{1}{\bar{h}}\frac{\partial}{\partial\eta}\langle v_0w_0\rangle + \frac{1}{\ell}\frac{\partial}{\partial s}\langle w_0^2\rangle - \frac{\eta}{\bar{h}}\frac{\partial}{\partial\eta}\langle\frac{\partial h_0'}{\partial t}w_0\rangle\\
&- \frac{\partial\bar{h}}{\partial x}\frac{\eta}{\bar{h}}\frac{\partial}{\partial\eta}\langle u_0w_0\rangle - \frac{1}{\ell}\frac{\partial\bar{h}}{\partial s}\frac{\eta}{\bar{h}}\frac{\partial}{\partial\eta}\langle w_0^2\rangle + \frac{2}{\bar{h}^3\alpha^2}\frac{\partial^2}{\partial\eta^2}\langle h_0'w_0\rangle \quad (2.31)
\end{aligned}$$

can be evaluated in terms of the leading-order solution. Computation of the time-averaged quantities is facilitated by use of the identities $\langle\mathrm{Re}(\mathrm{i}\mathrm{e}^{\mathrm{i}t}A)\,\mathrm{Re}(\mathrm{i}\mathrm{e}^{\mathrm{i}t}B)\rangle = \mathrm{Re}(AB^*)/2$ and $\langle\mathrm{Re}(\mathrm{e}^{\mathrm{i}t}A)\,\mathrm{Re}(\mathrm{i}\mathrm{e}^{\mathrm{i}t}B)\rangle = \mathrm{Im}(AB^*)/2$, which apply to any generic time-independent complex functions A and B, with the asterisk * denoting complex conjugates.

Integrating (2.27) and (2.28) subject to $\langle u_1\rangle = \langle w_1\rangle = 0$ at $\eta = 0, 1$ yields

$$\frac{\langle u_1\rangle}{\bar{h}^2\alpha^2} = -\frac{\mathrm{d}\langle p_1'\rangle}{\mathrm{d}x}\frac{(1-\eta)\eta}{2} + \eta\int_0^\eta\mathcal{F}_x\mathrm{d}\bar{\eta} - \int_0^\eta\mathcal{F}_x\bar{\eta}\mathrm{d}\bar{\eta} - \eta\int_0^1\mathcal{F}_x(1-\eta)\mathrm{d}\eta \quad (2.32)$$

and

$$\frac{\langle w_1\rangle}{\bar{h}^2\alpha^2} = -\frac{1}{\ell}\frac{\partial\langle\hat{p}_1\rangle}{\partial s}\frac{(1-\eta)\eta}{2} + \eta\int_0^\eta \mathcal{F}_s \mathrm{d}\tilde{\eta} - \int_0^\eta \mathcal{F}_s\tilde{\eta}\mathrm{d}\tilde{\eta} - \eta\int_0^1 \mathcal{F}_s(1-\eta)\mathrm{d}\eta \tag{2.33}$$

in terms of the unknown axial and azimuthal pressure gradients $\mathrm{d}\langle p_1'\rangle/\mathrm{d}x$ and $\partial\langle\hat{p}_1\rangle/\partial s$. The accompanying transverse steady-streaming velocity $\langle v_1\rangle$, not considered explicitly in [75], can be obtained by integration of (2.26), yielding

$$\begin{aligned}\langle v_1\rangle = &-\frac{1}{\ell}\frac{\partial}{\partial x}\left[\ell\int_0^\eta \left(\bar{h}\langle u_1\rangle + \langle h_0' u_0\rangle\right)\mathrm{d}\eta\right] + \eta\frac{\partial\bar{h}}{\partial x}\langle u_1\rangle + \eta\left\langle u_0\frac{\partial h_0'}{\partial x}\right\rangle \\ &-\frac{1}{\ell}\frac{\partial}{\partial s}\left[\int_0^\eta \left(\bar{h}\langle w_1\rangle + \langle h_0' w_0\rangle\right)\mathrm{d}\eta\right] + \eta\frac{1}{\ell}\frac{\partial\bar{h}}{\partial s}\langle w_1\rangle + \eta\left\langle w_0\frac{1}{\ell}\frac{\partial h_0'}{\partial s}\right\rangle.\end{aligned} \tag{2.34}$$

The axial and azimuthal steady-streaming components are related by

$$\frac{\partial}{\partial x}\left[\ell\left(\bar{h}\int_0^1\langle u_1\rangle\mathrm{d}\eta + \int_0^1\langle h_0' u_0\rangle\mathrm{d}\eta\right)\right] + \frac{\partial}{\partial s}\left(\bar{h}\int_0^1\langle w_1\rangle\mathrm{d}\eta + \int_0^1\langle h_0' w_0\rangle\mathrm{d}\eta\right) = 0 \tag{2.35}$$

obtained by evaluating (2.34) at $\eta = 1$. Integrating this last equation in the azimuthal direction gives

$$\bar{h}\int_0^1\langle w_1\rangle\mathrm{d}\eta + \int_0^1\langle h_0' w_0\rangle\mathrm{d}\eta = -\frac{\partial}{\partial x}\left[\ell\int_0^s\left(\bar{h}\int_0^1\langle u_1\rangle\mathrm{d}\eta + \int_0^1\langle h_0' u_0\rangle\mathrm{d}\eta\right)\mathrm{d}s\right], \tag{2.36}$$

which can be used together with (2.32) and (2.33) to determine $\partial\langle\hat{p}_1\rangle/\partial s$ as a function of $\mathrm{d}\langle p_1'\rangle/\mathrm{d}x$. Evaluating (2.36) at $s = 1$ and using the condition that the canal is closed at $x = 1$, so that the time-averaged value of the axial volume flux has to be necessarily zero, leads to

$$\int_0^1 \bar{h}\left(\int_0^1\langle u_1\rangle\mathrm{d}\eta\right)\mathrm{d}s + \int_0^1\int_0^1\langle h_0' u_0\rangle\mathrm{d}\eta\mathrm{d}s = 0, \tag{2.37}$$

which can be used, together with (2.32), to compute the average streamwise pressure gradient

$\mathrm{d}\langle p_1'\rangle/\mathrm{d}x$, thereby completing the determination of the steady-streaming flow.

The Eulerian velocity field includes a leading-order component, first-order corrections, and higher-order corrections (of the order ε^2 and smaller) which are not considered here. The leading-order components (u_0, v_0, w_0) are harmonic and have a time average that is identically zero. The first-order corrections (u_1, v_1, w_1) contain nonzero steady components $(\langle u_1\rangle, \langle v_1\rangle, \langle w_1\rangle)$, which is known as steady streaming.

2.3 Lagrangian Velocity Field

It can be anticipated that, in addition to the small oscillations of dimensionless amplitude ε induced by the pulsatile component of the flow, fluid particles undergo relative displacements of order unity in characteristic times of order $\varepsilon^{-2}\omega^{-1}$. We shall see that, besides the direct contribution resulting from the steady-streaming velocity $\langle \mathbf{v}_1\rangle = (\langle u_1\rangle, \langle v_1\rangle, \langle w_1\rangle)$, this slow Lagrangian motion includes an additional contribution associated with the Stokes drift of the fluid particles, resulting from the nonuniformity of the harmonic leading-order velocity field $\mathbf{v}_0$. This can be clarified by considering the motion of a fluid particle, whose trajectory is obtained by integration of

$$\begin{cases} \frac{\mathrm{d}x_p}{\mathrm{d}t} = \varepsilon u(x_p, \eta_p, s_p, t) \\ \frac{\mathrm{d}y_p}{\mathrm{d}t} = h\frac{\mathrm{d}\eta_p}{\mathrm{d}t} + \left(\frac{\partial h}{\partial t} + \frac{\partial h}{\partial x}\frac{\mathrm{d}x_p}{\mathrm{d}t} + \frac{\partial h}{\partial s}\frac{\mathrm{d}s_p}{\mathrm{d}t}\right)\eta_p = \varepsilon v(x_p, \eta_p, s_p, t) \\ \ell\frac{\mathrm{d}s_p}{\mathrm{d}t} = \varepsilon w(x_p, \eta_p, s_p, t) \end{cases} \tag{2.38}$$

with initial conditions $(x_p, \eta_p, s_p) = (x_i, \eta_i, s_i)$ at $t = 0$.

It is convenient to exploit the existence of the two time scales ω^{-1} and $\varepsilon^{-2}\omega^{-1}$ in a formal multiple-scale analysis that introduces a second time variable $\tau = \varepsilon^2 t$ to describe the slow evolution of the fluid-particle location, with $x_p(t,\tau)$, $\eta_p(t,\tau)$, and $s_p(t,\tau)$ assumed to be periodic in the short time scale t. This presumed time dependence is used to write (2.38) in the form

$$\frac{\partial x_p}{\partial t}+\varepsilon^2\frac{\partial x_p}{\partial \tau} = \varepsilon u, \tag{2.39}$$

$$h\left(\frac{\partial \eta_p}{\partial t}+\varepsilon^2\frac{\partial \eta_p}{\partial \tau}\right)+\varepsilon\left(\frac{\partial h'}{\partial t}+\frac{\partial h}{\partial x}u+\frac{1}{\ell}\frac{\partial h}{\partial s}w\right)\eta_p = \varepsilon v, \tag{2.40}$$

$$\ell\left(\frac{\partial s_p}{\partial t}+\varepsilon^2\frac{\partial s_p}{\partial \tau}\right) = \varepsilon w. \tag{2.41}$$

The problem can be solved by introducing the expansions

$$\begin{cases} x_p = x_0(t,\tau)+\varepsilon x_1(t,\tau)+\varepsilon^2 x_2(t,\tau)+\cdots \\ \eta_p = \eta_0(t,\tau)+\varepsilon \eta_1(t,\tau)+\varepsilon^2 \eta_2(t,\tau)+\cdots \\ s_p = s_0(t,\tau)+\varepsilon s_1(t,\tau)+\varepsilon^2 s_2(t,\tau)+\cdots \end{cases} . \tag{2.42}$$

The Eulerian velocity components appearing in (2.39)–(2.41) must be expressed in the Taylor-expansion form

$$\begin{aligned} u &= u_0(\mathbf{x}_0,t)+\varepsilon\left[u_1(\mathbf{x}_0,t)+x_1\tfrac{\partial u_0}{\partial x}(\mathbf{x}_0,t)+\eta_1\tfrac{\partial u_0}{\partial \eta}(\mathbf{x}_0,t)+s_1\tfrac{\partial u_0}{\partial s}(\mathbf{x}_0,t)\right]+\cdots \\ v &= v_0(\mathbf{x}_0,t)+\varepsilon\left[v_1(\mathbf{x}_0,t)+x_1\tfrac{\partial v_0}{\partial x}(\mathbf{x}_0,t)+\eta_1\tfrac{\partial v_0}{\partial \eta}(\mathbf{x}_0,t)+s_1\tfrac{\partial v_0}{\partial s}(\mathbf{x}_0,t)\right]+\cdots \\ w &= w_0(\mathbf{x}_0,t)+\varepsilon\left[w_1(\mathbf{x}_0,t)+x_1\tfrac{\partial w_0}{\partial x}(\mathbf{x}_0,t)+\eta_1\tfrac{\partial w_0}{\partial \eta}(\mathbf{x}_0,t)+s_1\tfrac{\partial w_0}{\partial s}(\mathbf{x}_0,t)\right]+\cdots \end{aligned} \tag{2.43}$$

where the known functions (u_0,v_0,w_0), (u_1,v_1,w_1), ... and their derivatives are evaluated at $\mathbf{x}_0=(x_0,\eta_0,s_0)$. Similarly, the canal perimeter $\ell(x)$ and width $h(x,s,t)$ must be expanded according to

$$\ell = \ell(x_0)+\varepsilon x_1\frac{\partial \ell}{\partial x}(x_0)+\cdots \tag{2.44}$$

and

$$h=\bar{h}(x_0,s_0)+\varepsilon\left[h'_0(x_0,s_0,t)+x_1\frac{\partial \bar{h}}{\partial x}(x_0,s_0)+s_1\frac{\partial \bar{h}}{\partial s}(x_0,s_0)\right]+\cdots, \tag{2.45}$$

with similar expansions introduced for the known geometrical functions $\partial h'_0/\partial t$, $\partial h'_1/\partial t$, $\partial \bar{h}/\partial x$, and $\partial\bar{h}/\partial s$.

Substituting (2.42)–(2.45) into (2.39)–(2.41) and collecting the terms that appear at different orders in powers of ε lead to a set of equations that can be solved sequentially. At the leading-order, $O(1)$, the problem becomes

$$\frac{\partial x_0}{\partial t} = \frac{\partial \eta_0}{\partial t} = \frac{\partial s_0}{\partial t} = 0, \tag{2.46}$$

which can be readily integrated to give the result $\mathbf{x}_0 = [x_0(\tau), \eta_0(\tau), s_0(\tau)]$, indicating that the leading-order terms evolve only in the long time scale, so that the fast oscillatory motion is restricted to the first-order corrections $\mathbf{x}_1 = (x_1, \eta_1, s_1)$, as is consistent with the small stroke lengths of order ε of the Eulerian velocity field. The rate of change in the long time scale $\mathrm{d}\mathbf{x}_0/\mathrm{d}\tau$ determines the time-averaged Lagrangian velocity components of the slow bulk motion according to

$$u_{\mathrm{L}} = \frac{\mathrm{d}x_0}{\mathrm{d}\tau},\ v_{\mathrm{L}} = \frac{\mathrm{d}y_0}{\mathrm{d}\tau} = \bar{h}\frac{\mathrm{d}\eta_0}{\mathrm{d}\tau} + \eta_0 \frac{\partial\bar{h}}{\partial x}\frac{\mathrm{d}x_0}{\mathrm{d}\tau} + \eta_0 \frac{\partial\bar{h}}{\partial s}\frac{\mathrm{d}s_0}{\mathrm{d}\tau},\ w_{\mathrm{L}} = \ell\frac{\mathrm{d}s_0}{\mathrm{d}\tau} \tag{2.47}$$

to be obtained below by carrying the analysis to order ε^2.

At order ε we find

$$\begin{aligned} \frac{\partial x_1}{\partial t} &= u_0, && (2.48)\\ \bar{h}\frac{\partial \eta_1}{\partial t} &= v_0 - \left(\frac{\partial h_0'}{\partial t} + \frac{\partial \bar{h}}{\partial x}u_0 + \frac{1}{\ell}\frac{\partial \bar{h}}{\partial s}w_0\right)\eta_0, && (2.49)\\ \ell\frac{\partial s_1}{\partial t} &= w_0. && (2.50) \end{aligned}$$

Since the dependence on the short time scale t enters above only through the harmonic functions $u_0[\mathbf{x}_0(\tau), t]$, $v_0[\mathbf{x}_0(\tau), t]$, $w_0[\mathbf{x}_0(\tau), t]$, and $\partial h_0'/\partial t[x_0(\tau), s_0(\tau), t]$, given in (2.14), straightforward integration provides

$$
\begin{aligned}
x_1 &= \int u_0 \mathrm{d}t + \tilde{x}_1(\tau), && (2.51)\\
\eta_1 &= \frac{1}{\bar{h}}\left[\int v_0 \mathrm{d}t - \left(h_0' + \frac{\partial \bar{h}}{\partial x}\int u_0 \mathrm{d}t + \frac{1}{\ell}\frac{\partial \bar{h}}{\partial s}\int w_0 \mathrm{d}t\right)\eta_0\right] + \tilde{\eta}_1(\tau) && (2.52)\\
s_1 &= \frac{1}{\ell}\int w_0 \mathrm{d}t + \tilde{s}_1(\tau), && (2.53)
\end{aligned}
$$

with

$$\int u_0 \mathrm{d}t = \mathrm{Re}\left(\mathrm{e}^{\mathrm{i}t}U\right), \int v_0 \mathrm{d}t = \mathrm{Re}\left(\mathrm{e}^{\mathrm{i}t}V\right), \int w_0 \mathrm{d}t = \mathrm{Re}\left(\mathrm{e}^{\mathrm{i}t}W\right), \tag{2.54}$$

as follows from (2.14). The slowly varying terms $\tilde{x}_1$, $\tilde{\eta}_1$, and $\tilde{s}_1$ appearing in (2.51)–(2.53), which represent small relative corrections of order ε to the long-time evolution of the fluid-particle location, are not considered in the present development but could be obtained by carrying the analysis to a higher order.

Collecting terms of order $O(\varepsilon^2)$ in (2.39) provides

$$\frac{\partial x_2}{\partial t} + \frac{\mathrm{d}x_0}{\mathrm{d}\tau} = u_1 + x_1\frac{\partial u_0}{\partial x} + \eta_1\frac{\partial u_0}{\partial \eta} + s_1\frac{\partial u_0}{\partial s}, \tag{2.55}$$

which leads to

$$
\begin{aligned}
\frac{\mathrm{d}x_0}{\mathrm{d}\tau} &= \langle u_1\rangle + \left\langle \frac{\partial u_0}{\partial x}\int u_0 \mathrm{d}t\right\rangle + \frac{1}{\bar{h}}\left\langle \frac{\partial u_0}{\partial \eta}\int v_0 \mathrm{d}t\right\rangle + \frac{1}{\ell}\left\langle \frac{\partial u_0}{\partial s}\int w_0 \mathrm{d}t\right\rangle\\
&- \frac{\eta_0}{\bar{h}}\left(\left\langle \frac{\partial u_0}{\partial \eta}h_0'\right\rangle + \frac{\partial \bar{h}}{\partial x}\left\langle \frac{\partial u_0}{\partial \eta}\int u_0 \mathrm{d}t\right\rangle + \frac{1}{\ell}\frac{\partial \bar{h}}{\partial s}\left\langle \frac{\partial u_0}{\partial \eta}\int w_0 \mathrm{d}t\right\rangle\right) \qquad (2.56)
\end{aligned}
$$

upon taking the time average $\langle\cdot\rangle = \frac{1}{2\pi}\int_t^{t+2\pi}\cdot\,\mathrm{d}t$. The above equation includes products of the harmonic functions (2.14) and (2.54). Using the leading order continuity equation (2.11) along with integration by parts enables the above equation (2.56) to be written in the compact form

$$\begin{aligned} u_{\mathrm{L}} = \frac{\mathrm{d}x_0}{\mathrm{d}\tau} = \langle u_1 \rangle \quad &+ \quad \frac{1}{\bar{h}} \left\{ \langle u_0 h_0' \rangle + \frac{1}{\ell}\frac{\partial}{\partial s}\left(\bar{h} \left\langle u_0 \int w_0 \mathrm{d}t \right\rangle \right) \right\} \\ &+ \quad \frac{1}{\bar{h}}\frac{\partial}{\partial \eta} \left\langle u_0 \left[\int v_0 \mathrm{d}t - \eta \left(h_0' + \frac{1}{\ell}\frac{\partial \bar{h}}{\partial s} \int w_0 \mathrm{d}t \right) \right] \right\rangle . \end{aligned} \tag{2.57}$$

As expected, besides the steady-streaming velocity $\langle u_1 \rangle$, the Lagrangian velocity includes a Stokes-drift component arising from the interactions of the leading-order axial velocity with the leading-order azimuthal and transverse velocities and the deformation of the canal. Except for the contribution due to the canal deformation, the Stokes-drift component arises due to the nonuniformity of the velocity field, as can be seen by the presence of the partial derivatives in η and s. Similar manipulations of the corresponding equations for $\mathrm{d}\eta_0/\mathrm{d}\tau$ and $\mathrm{d}s_0/\mathrm{d}\tau$ lead to

$$\begin{aligned} v_{\mathrm{L}} = \langle v_1 \rangle \quad &+ \quad \frac{1}{\ell}\frac{\partial}{\partial x}\left(\ell \left\langle v_0 \int u_0 \mathrm{d}t \right\rangle \right) + \frac{1}{\ell}\frac{\partial}{\partial s} \left\langle v_0 \int w_0 \mathrm{d}t \right\rangle \\ &- \quad \frac{\eta}{\bar{h}}\frac{\partial}{\partial \eta} \left\langle v_0 \left(h_0' + \frac{\partial \bar{h}}{\partial x} \int u_0 \mathrm{d}t + \frac{1}{\ell}\frac{\partial \bar{h}}{\partial s} \int w_0 \mathrm{d}t \right) \right\rangle \end{aligned} \tag{2.58}$$

and

$$\begin{aligned} w_{\mathrm{L}} = \langle w_1 \rangle \quad &+ \quad \frac{1}{\bar{h}} \left[\langle w_0 h_0' \rangle + \frac{\partial}{\partial x}\left(\bar{h} \left\langle w_0 \int u_0 \mathrm{d}t \right\rangle \right) \right] \\ &+ \quad \frac{1}{\bar{h}}\frac{\partial}{\partial \eta} \left\langle w_0 \left[\int v_0 \mathrm{d}t - \eta \left(h_0' + \frac{\partial \bar{h}}{\partial x} \int u_0 \mathrm{d}t \right) \right] \right\rangle \end{aligned} \tag{2.59}$$

also exhibiting both steady-streaming and Stokes-drift contributions.

The three components satisfy the mass conservation equation

$$\frac{1}{\ell}\frac{\partial}{\partial x}(\ell u_{\mathrm{L}}) - \frac{\partial \bar{h}}{\partial x}\frac{\eta}{\bar{h}}\frac{\partial u_{\mathrm{L}}}{\partial \eta} + \frac{1}{\bar{h}}\frac{\partial v_{\mathrm{L}}}{\partial \eta} + \frac{1}{\ell}\frac{\partial w_{\mathrm{L}}}{\partial s} - \frac{1}{\ell}\frac{\partial \bar{h}}{\partial s}\frac{\eta}{\bar{h}}\frac{\partial w_{\mathrm{L}}}{\partial \eta} = 0, \tag{2.60}$$

which can be integrated across the canal to give

$$\frac{1}{\ell}\frac{\partial}{\partial x}\left(\ell\bar{h}\int_0^1 u_{\mathrm{L}}\mathrm{d}\eta\right)+\frac{1}{\ell}\frac{\partial}{\partial s}\left(\bar{h}\int_0^1 w_{\mathrm{L}}\mathrm{d}\eta\right)=0 \tag{2.61}$$

relating the width-averaged values

$$\int_0^1 u_{\mathrm{L}}\mathrm{d}\eta=\int_0^1\langle u_1\rangle\mathrm{d}\eta+\frac{1}{\bar{h}}\left[\int_0^1\langle h_0'u_0\rangle\mathrm{d}\eta+\frac{1}{\ell}\frac{\partial}{\partial s}\left(\bar{h}\int_0^1\left\langle u_0\int w_0\mathrm{d}t\right\rangle\mathrm{d}\eta\right)\right] \tag{2.62}$$

and

$$\int_0^1 w_{\mathrm{L}}\mathrm{d}\eta=\int_0^1\langle w_1\rangle\mathrm{d}\eta+\frac{1}{\bar{h}}\left[\int_0^1\langle h_0'w_0\rangle\mathrm{d}\eta+\frac{\partial}{\partial x}\left(\bar{h}\int_0^1\left\langle w_0\int u_0\mathrm{d}t\right\rangle\mathrm{d}\eta\right)\right] \tag{2.63}$$

of the axial and azimuthal components of the time-averaged Lagrangian flow, which will be of interest later.

2.4 Results for a Simplified Geometry

The Lagrangian velocity field $(u_{\mathrm{L}}, v_{\mathrm{L}}, w_{\mathrm{L}})$, as well as the width-averaged values $\int_0^1 u_{\mathrm{L}}\mathrm{d}\eta$ and $\int_0^1 w_{\mathrm{L}}$, can be evaluated using the expressions (2.57)–(2.59) and (2.62)–(2.63). The results depend on the Womersley number α defined in (2.8), which measures the relative importance of viscous forces, and the dimensionless wave number defined in (2.4), which enters in the elastic equation (2.3) relating the pressure with the canal deformation, both order-unity parameters. The geometry of the canal is defined by the inner perimeter $\ell(x)$ and unperturbed canal width $\bar{h}(x,s)$, both order-unity dimensionless functions. Additionally, a compliance function $\gamma(x,s)\sim 1$ is introduced for generality to describe the spatial variation of the elastic properties of the outer dura membrane.

Although the formulation above can be used to describe the Lagrangian velocity field

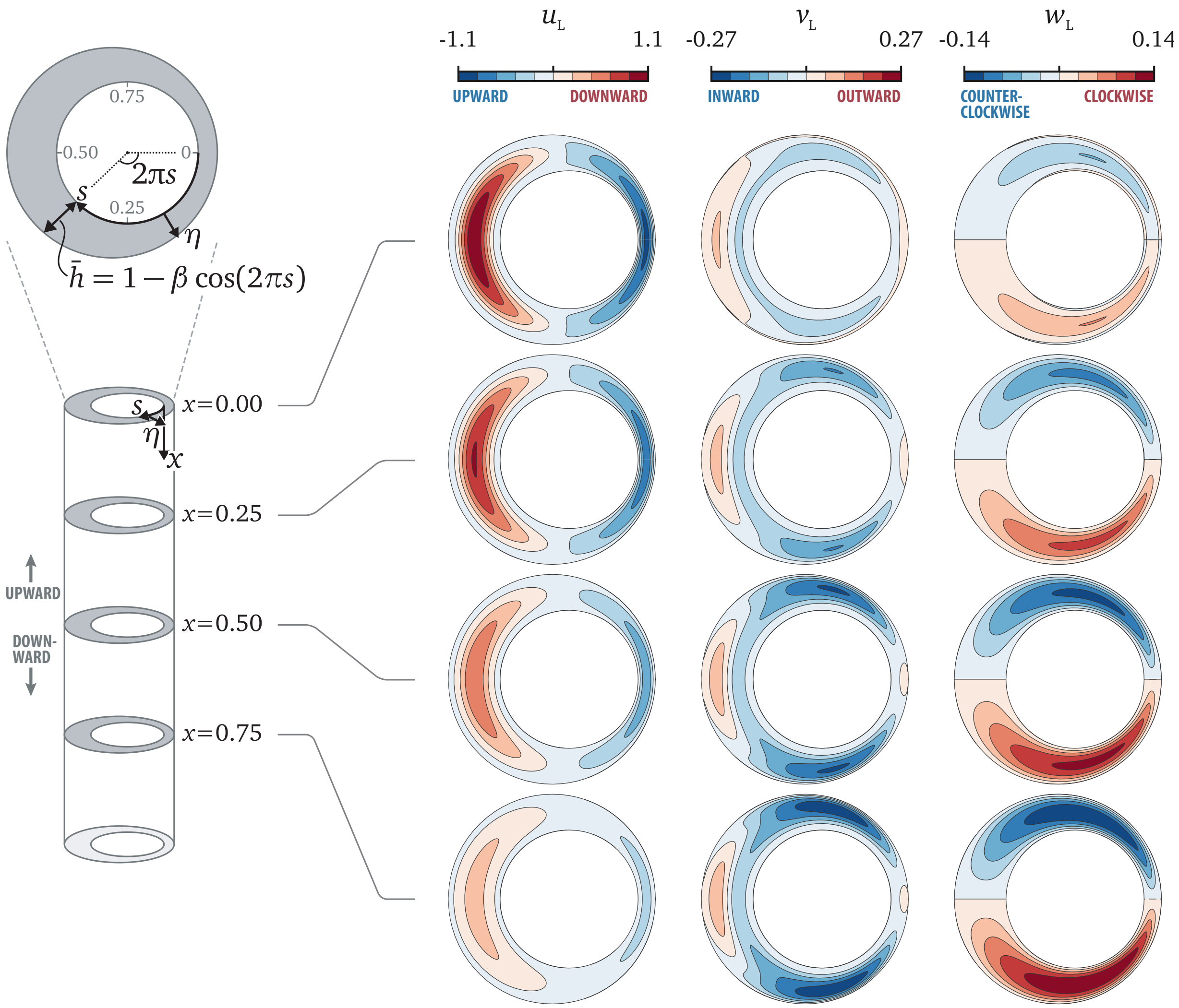

Figure 2.1: A schematic view of the model geometry used in the numerical evaluations (left figure) and the associated distributions of Lagrangian-velocity components at different sections x for $\beta = 0.5$, $\alpha = 3$, $k = 0.5$ (right-hand-side panels).

in anatomically-correct spinal-canal geometries through introduction of appropriately selected functions $\ell(x)$, $\bar{h}(x,s)$, and $\gamma(x,s)$, we use a simplified model geometry to highlight the dominant features of cerebrospinal fluid motion. Following previous work [75], the SSAS is modeled as an annular canal with uniform elastic properties (i.e. $\gamma = 1$) bounded between two eccentric parallel circular cylinders whose radii differ by a small amount h_c and whose axes are displaced by βh_c with $0 \leq \beta < 1$, so that $\ell = 1$ and $\bar{h} = 1 - \beta\cos(2\pi s)$. The resulting canal geometry is schematically represented on the left side of figure 2.1.

The expressions given in (2.57)–(2.59) together with the leading-order Eulerian velocity components u_0, v_0, w_0, wall deformation h_0', and steady-streaming components $\langle u_1\rangle$, $\langle v_1\rangle$, and $\langle w_1\rangle$ can be used to evaluate $(u_{\mathrm{L}}, v_{\mathrm{L}}, w_{\mathrm{L}})$. The panels on the right side of figure 2.1 show the resulting distributions at different sections x for $\beta = 0.5$, $\alpha = 3$, and $k = 0.5$, with the width of the annular cross-section arbitrarily enlarged to facilitate visualization. As expected, the distributions of u_{L} and v_{L} are symmetric with respect to the symmetry plane of the canal ($s = 0,\ 0.5$), whereas w_{L} is antisymmetric.

For the geometry investigated, steady streaming is the dominant contribution to the Lagrangian velocity, while the contribution of Stokes drift is comparatively smaller. This is apparent when comparing the distributions of axial and azimuthal Lagrangian velocity u_{L} and w_{L} shown in figure 2.1 with the distributions of $\langle u_1\rangle$ and $\langle w_1\rangle$, given for these same conditions in figures 5 and 6 of [75]. The comparison reveals that the Lagrangian velocity and the steady-streaming velocity display the same qualitative characteristics. In particular, the axial motion is directed towards the cranial vault (i.e. negative values of u_{L} and $\langle u_1\rangle$) in the narrow part of the canal and towards the lumbar region (i.e. positive values of u_{L} and $\langle u_1\rangle$) in the wide part, with the azimuthal velocity being directed from the narrowest section $s = 0$ to the widest section $s = 0.5$ to accommodate the deceleration of the flow as the closed end is approached.

The width-averaged axial and azimuthal components of the Lagrangian velocity $\int_0^1 u_{\mathrm{L}}\mathrm{d}\eta$ and $\int_0^1 w_{\mathrm{L}}\mathrm{d}\eta$, which will be of use for future calculations, are plotted on the left-hand side panels

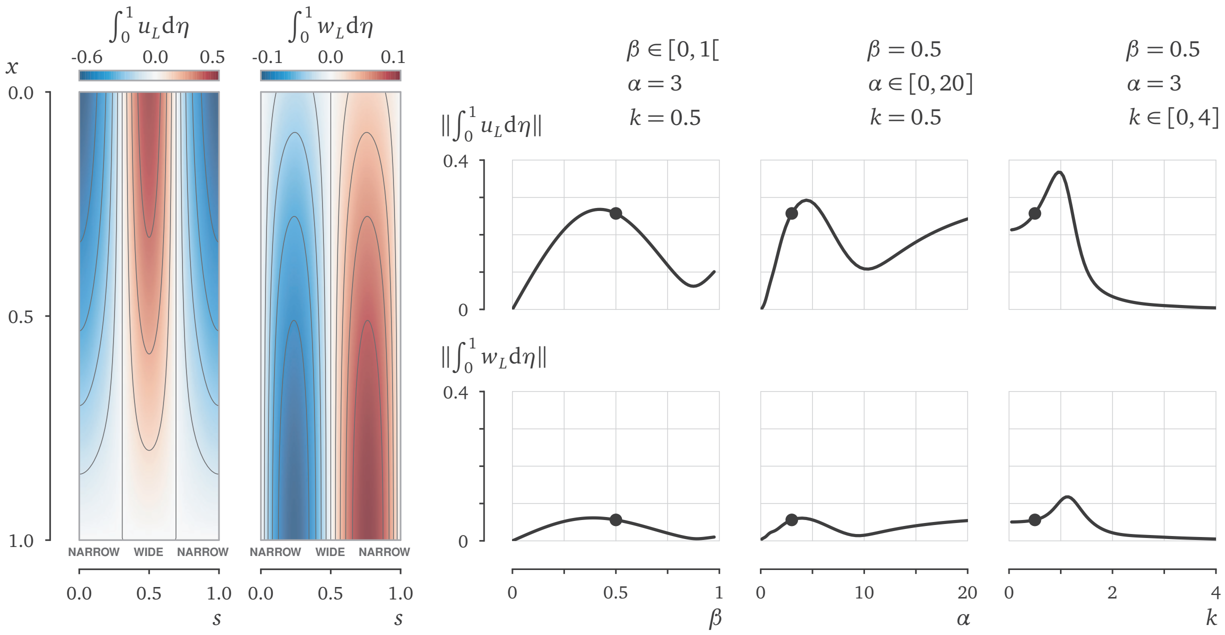

Figure 2.2: The left-hand side maps show the distributions of the width-averaged axial and azimuthal Lagrangian velocity components for $\beta = 0.5$, $\alpha = 3$, and $k = 0.5$, while the right-hand side plots show the parametric variation of their root-mean-square values $||\int_0^1 u_\mathrm{L} \mathrm{d}\eta||$ and $||\int_0^1 w_\mathrm{L} \mathrm{d}\eta||$, with the dots indicating the values corresponding to the distributions shown on the left.

of figure 2.2 for the same conditions as figure 2.1. Parametric dependences on the three controlling parameters β, α, and k, are investigated on the right-hand-side plots by showing the variation of the root-mean-square values $||\int_0^1 u_{\mathrm{L}}\mathrm{d}\eta||$ and $||\int_0^1 w_{\mathrm{L}}\mathrm{d}\eta||$ (where $||\cdot|| = \left[\int_0^1 \int_0^1 (\cdot)^2 \mathrm{d}s\mathrm{d}x\right]^{1/2}$) with each individual parameter, while keeping the other two at the fixed constant values of figure 2.1.

The results in figure 2.2 indicate that for axisymmetric configurations, corresponding in the model to the case $\beta = 0$ of concentric cylinders, the azimuthal motion is absent, and the resulting width-averaged axial velocity is strictly zero, as follows from the continuity equation (2.61). This feature of the solution emphasizes the importance of eccentricity. If the spinal canal had perfect axial symmetry, convective transport would be drastically limited. Nonzero values of $\int_0^1 u_{\mathrm{L}}\mathrm{d}\eta$ and $\int_0^1 w_{\mathrm{L}}\mathrm{d}\eta$ are found for any $\beta > 0$, with the motion being most pronounced for an intermediate value (i.e. $\beta \simeq 0.4$ for $\alpha = 3$, and $k = 0.5$).

The effect of viscous forces is measured in the problem through the Womersley number $\alpha = h_c/(\nu/\omega)^{1/2}$. When viscous effects are dominant for $\alpha \ll 1$, the resulting pulsating flow is very slow and the associated Lagrangian motion, involving time-averaged products of fluctuations, becomes negligibly slow. In the opposite limit $\alpha \gg 1$, viscosity effects are confined to near-wall Stokes layers. The numerical evaluations reveal a persistent Lagrangian motion with associated root-mean-square velocities that approach finite values for $\alpha \gg 1$. It is of interest that, for intermediate values $\alpha \sim 1$, pertaining to spinal-canal flow conditions, the curves of $||\int_0^1 u_{\mathrm{L}}\mathrm{d}\eta||$ and $||\int_0^1 w_{\mathrm{L}}\mathrm{d}\eta||$ in figure 2.2 display a non-monotonic variation, with maxima reached at $\alpha \simeq 4$ followed by local minima around $\alpha \simeq 10$.

The last column in figure 2.2 investigates the influence of the wave number k, which measures the ratio of the canal length to the characteristic elastic-wave length, a parameter of order unity in the spinal canal, as shown by MRI measurements [34]. This parameter determines the amplitude of the tidal volume flux for the leading-order oscillatory flow, as shown in [75]. The numerical computations reveal finite values of $||\int_0^1 u_{\mathrm{L}}\mathrm{d}\eta||$ and $||\int_0^1 w_{\mathrm{L}}\mathrm{d}\eta||$ for $k \ll 1$, corresponding to canal deformations that are everywhere in phase with the cranial pressure variation.

The Lagrangian velocities increase initially with increasing k, but eventually decrease to vanish in the short-wave-length limit $k \gg 1$, associated with vanishing tidal volume fluxes. The most pronounced Lagrangian motion is found around $k \simeq 1$, associated with the peak in the amplitude of the tidal volume flux (see figure 2 in [75]).

For the simple geometry investigated here, the overall Lagrangian motion depends non-monotonically on the three controlling parameters β, α , and k. It is worth noticing that the local maxima for α and k found in this parametric study are of order unity, as expected from the order of magnitude analysis. The Lagrangian flow is significantly reduced for $\beta = 0$, extreme values of k, and for some values of α.

2.5 DNS Validation

With the aim of providing detailed numerical results for validation of the theoretical model, three-dimensional, unsteady direct numerical simulations (DNS) of fluid motion in the spinal canal are conducted. Following previous theoretical developments, the present analysis will approximate the SSAS as an open annular canal, thereby neglecting the presence of micro-anatomical obstacles, such as trabeculae, ligaments, and nerve roots. Two geometrically simple configurations will be investigated, as sketched in figure 2.3(b) and (c). The exterior surface surrounding the canal represents the dura membrane, while the interior surface represents the rigid pia mater surrounding the spinal cord. The deformation of the veins and fatty tissue present in the dura membrane due to local pressure fluctuations must be accounted for in analyzing the motion of the CSF, leading to a fluid-structure interaction problem that was previously solved on the basis of a linear elastic model. The associated time-dependent displacements are small compared with the canal thickness, and can therefore be analyzed as small perturbations from an unperturbed state.

The unperturbed shape of the dura membrane will be taken to be a circular cylinder of

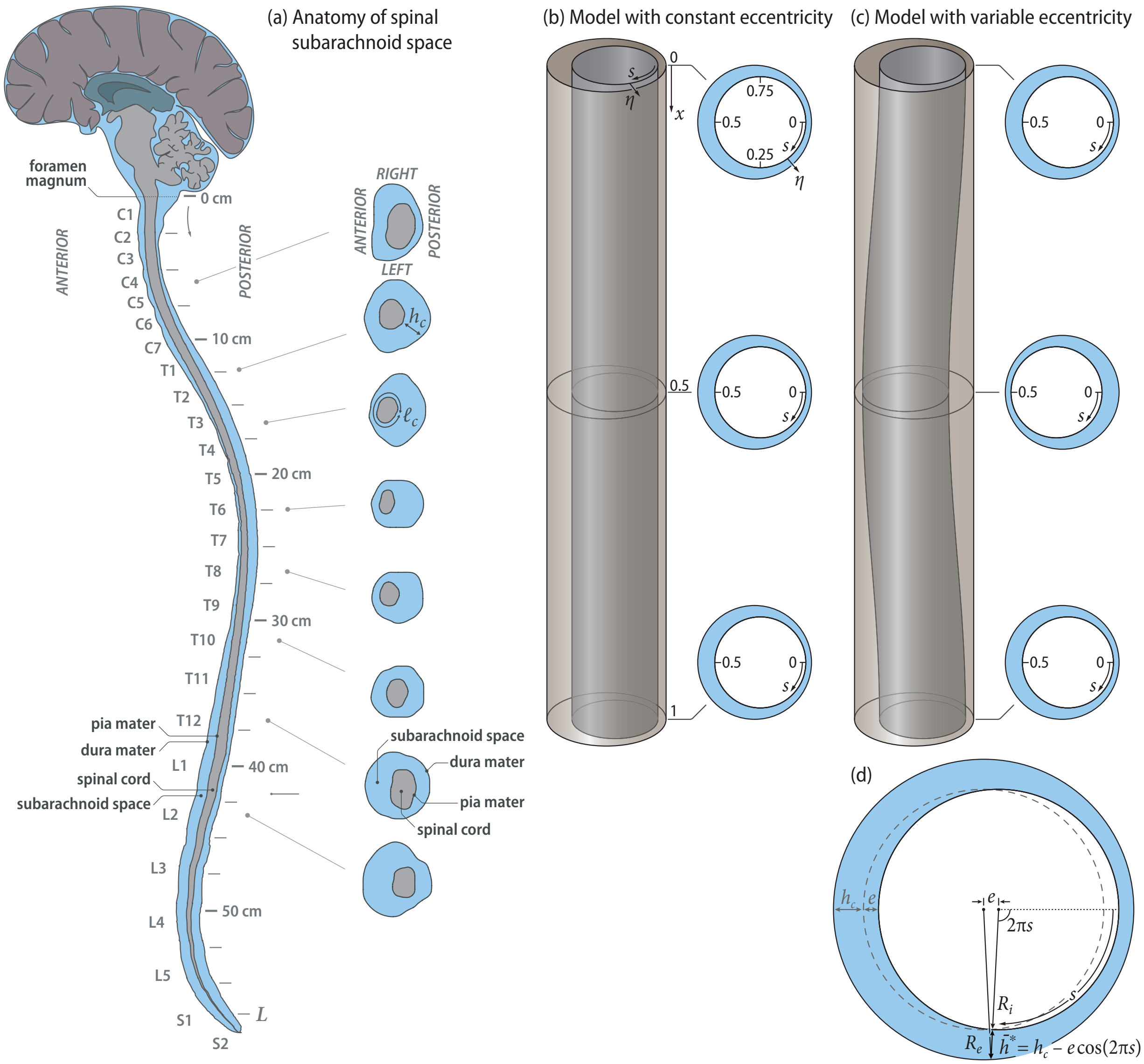

Figure 2.3: Sketch of the geometrical configurations. (a) Anatomy of the spinal subarachnoid space (SSAS) extending from the foramen magnum to the sacrum. The figure shows several axial cuts at different locations. (b) Geometrical model with constant eccentricity indicating the curvilinear coordinates (x, s, η). (c) Geometrical model with variable eccentricity. (d) Definition of the unperturbed canal width in the geometrical models.

radius R_e and length L. A circular cross section will also be assumed for the rigid inner surface surrounding the spinal canal, whose radius is $R_i = R_e - h_c$ with $h_c \ll R_e$. Correspondingly, in a plane perpendicular to the axis of the outer cylinder the annular canal is the space defined between two eccentric circles whose centers are separated by a small distance e, with $0 \leq e \leq h_c$, as indicated in figure 2.3(d). With small errors of order $h_c/R_e \ll 1$, the local unperturbed width of the canal $\bar{h}^*$, measured normal to the inner surface, is given by $\bar{h}^* = h_c - e\cos(2\pi s)$, with $0 \leq s \leq 1$. The configuration with two parallel cylinders of figure 2.3(b), used in computations for the previous section, corresponds to the case of constant eccentricity $e = \beta h_c$, where $\beta < 1$ is a positive constant representing the degree of eccentricity. The configuration in figure 2.3(c), introduced here to investigate effects of variable eccentricity, considers the simple functional dependence $e/h_c = \beta\cos(2\pi x)$.

To facilitate the computation, instead of using the intracranial pressure as input, the displacement of the dura membrane was prescribed, that also being the approach of the moving-boundary-motion method first used in the computations of Tangen et al. (2015) [83] (see also Khani et al. 2018 [37]). For consistency, the nonuniform temporal distribution of the dura-membrane displacement was selected to be that found at leading order in the previous theoretical analysis of the fluid-structure interaction problem [75].

In the first stage of the computations, the Navier–Stokes equations for an incompressible Newtonian fluid,

$$\nabla \cdot \bar{v}^* = 0, \tag{2.64}$$

$$\frac{\partial \bar{v}^*}{\partial t^*} + \bar{v}^* \cdot \nabla \bar{v}^* = -\nabla p^* + \nu \nabla^2 \bar{v}^*, \tag{2.65}$$

were solved over many wall-displacement oscillation cycles until a periodic solution was attained. In the governing equations (2.64) and (2.65), asterisks denote dimensional variables and p^* represents the spatial pressure differences divided by the density. Numerically averaging the periodic Eulerian velocity $\bar{v}^*$ yields its steady-streaming component, which in turn can be subtracted from $\bar{v}^*$ to determine the zero-mean leading-order component of the velocity. Both are to be compared with the results of the asymptotic analysis presented in sections 2.2.1 and 2.2.2.

Equations (2.64) and (2.65) were solved numerically with the finite-volume solver Ansys

Fluent (Release 16.2), assuring second-order accuracy in time and in space. The PISO algorithm was used for the pressure–velocity coupling [32]. No-slip conditions were imposed at the canal walls and a condition of developed flow, $\nabla \bar{v}^* \cdot \bar{n} = 0$ was imposed at the inlet, where a buffer region of length $0.15L$ was added to avoid entrance effects. To model the deformation of the dura membrane, a dynamic mesh solver that employs a Laplacian mesh motion algorithm was used [37, 84], with the instantaneous radius of the external boundary surface R_e' varying from its unperturbed value R_e according to

$$R_e' = R_e + \varepsilon h_c h_0'(x^*/L, \omega t^*) = R_e + \varepsilon h_c |H'| \cos[\omega t^* + \arg(H')]. \tag{2.66}$$

Here, the elastic-wave deformation $h_0' = |H'| \cos[\omega t^* + \arg(H')]$ is determined from the complex function H', given in (2.21) from the previous asymptotic analysis. The equation for H' accommodates general axial and azimuthal variations of $\gamma(x, s)$, as needed to account for the non-uniform deformable nature of the dura membrane [70], enabling subject-specific studies in which the function $\gamma(x, s)$ can be determined from in-vivo MRI measurements of CSF flow, as done recently [13]. For the sake of simplicity, however, the following validation exercise is restricted to cases with constant γ.

While the theoretical model is formulated in terms of dimensionless parameters, the DNS formulation requires specification of dimensional values for all parameters appearing in the equations and boundary conditions. The kinematic viscosity, appearing in equation (2.65), was taken to be $\nu = 0.698 \times 10^{-6}\,\mathrm{m}^2/\mathrm{s}$, the value corresponding to water at 36.8^{o} C. The dimensions of the domain for the two configurations shown in Figs. 2.3(b) and (c) are $L = 0.6\,\mathrm{m}$, $R_e = 5\,\mathrm{mm}$, and $R_i = 4\,\mathrm{mm}$, corresponding to a canal with characteristic width $h_c = R_e - R_i = 1\,\mathrm{mm}$ and constant inner perimeter $\ell_c = 2\pi R_i \simeq 25\,\mathrm{mm}$. In all computations, the dimensionless eccentricity is taken to be $\beta = 0.5$. The canal deformation, given in (2.66), is evaluated for an angular frequency $\omega = 2\pi\, s^{-1}$, as corresponds approximately to the cardiac cycle, with the function $H'(x^*/L)$, given in (2.21), computed with $k = 0.5$ and $\alpha = (h_c^2\omega/\nu)^{1/2} = 3$, the latter value consistent with the parametric choice $h_c = 1\,\mathrm{mm}$, $\omega = 2\pi s^{-1}$, and $\nu = 0.698 \times 10^{-6}\,\mathrm{m}^2/\mathrm{s}$. In all computations, the reduced amplitude is taken to be $\varepsilon = 1/20$.

The computational domain was discretized using a structured uniform mesh. A grid sensitivity analysis was conducted to ensure the grid-size independence of the results. To that end, integrations were sequentially performed with an increasing number of grid points, starting from a coarse grid with 7.5×10^4 computational cells. In comparing results corresponding to different grids, the periodic velocity field was characterized by the amplitude of the axial velocity oscillation $(u^*_{\max} - u^*_{\min})$ at two locations of the anteroposterior plane, namely, $x^* = L/2$ $(x = 1/2)$, $y^* = \bar{h}/2$ $(\eta = 1/2)$ and $s = 0$ and $s = 0.5$. This velocity amplitude was seen to decrease as the number of grid point increases, with relative changes becoming progressively smaller. The refinement was continued until the relative differences of the velocity resulting from doubling the number of grid points in consecutive computations were less than 0.3%. The final configuration selected, to be used in the computations presented below, contains a total of 1.95×10^6 grid points.

In the following, results from the simulations will be compared with those of the previous theoretical analyses. The steady-streaming velocity components u_{SS} and w_{SS} will be evaluated from the DNS results by taking the time averages $\langle u^* \rangle = \omega/(2\pi) \int_0^{2\pi/\omega} u^* \,\mathrm{d}t^*$ and $\langle w^* \rangle = \omega/(2\pi) \int_0^{2\pi/\omega} w^* \,\mathrm{d}t^*$, and scaling the resulting axial and azimuthal components with their characteristic values $\varepsilon^2\omega L$ and $\varepsilon^2\omega\ell_c$, respectively. These values are compared below with the theoretical predictions $u_{\mathrm{SS}} = \langle u_1 \rangle$ and $w_{\mathrm{SS}} = \langle w_1 \rangle$ from the asymptotic analysis. Similarly, the harmonic leading-order velocity components predicted by the linear lubrication problem, $(u_0, w_0) = \mathrm{Re}\left[\mathrm{i}\mathrm{e}^{\mathrm{i}t}(U, W)\right]$, will be compared with the corresponding DNS predictions for the purely oscillatory flow, obtained by subtracting its mean value according to $u^* - \langle u^* \rangle$ and $w^* - \langle w^* \rangle$, and scaling the resulting axial and azimuthal velocity components with their characteristic values $\varepsilon\omega L$ and $\varepsilon\omega\ell_c$.

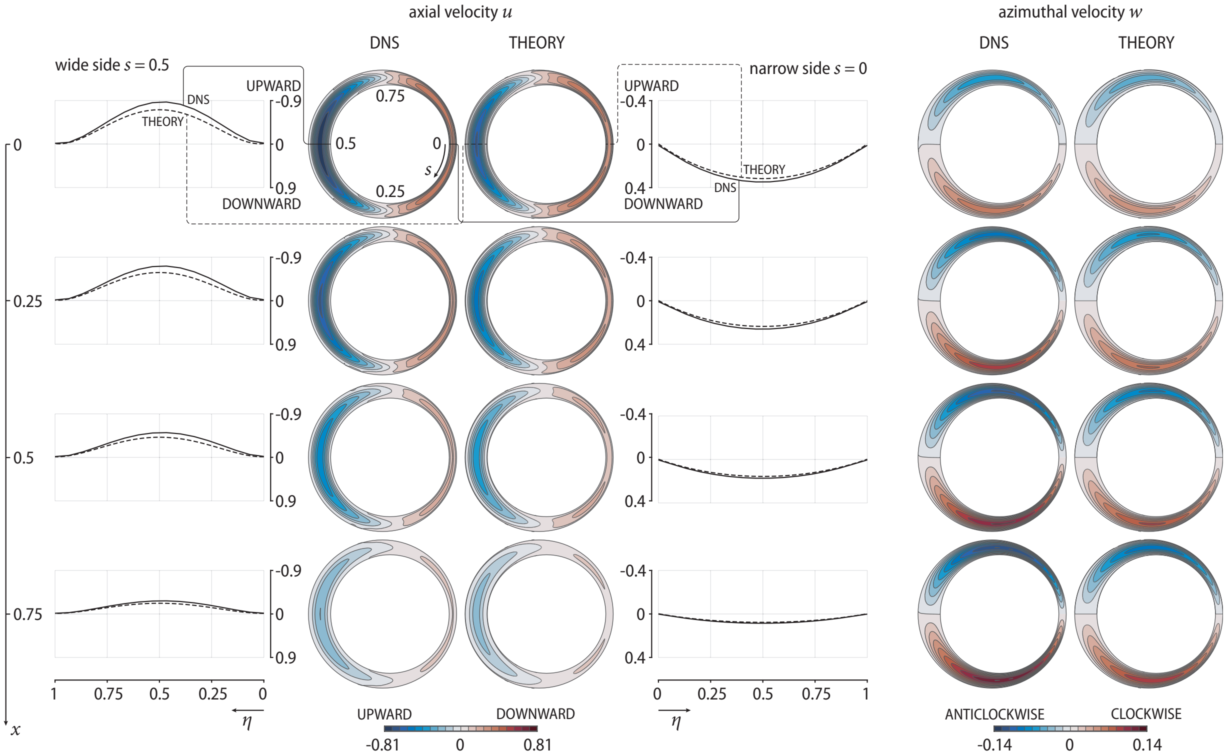

Figure 2.4: Comparison of the oscillatory velocity determined in the numerical simulations with that predicted by the simplified model. The theoretical predictions are evaluated from the analytical expressions $u_0 = \text{Re}\left[\text{ie}^{\text{i}t}U(x,\eta,s)\right]$ and $w_0 = \text{Re}\left[\text{ie}^{\text{i}t}W(x,\eta,s)\right]$, with the normalized transverse coordinate η taken to be perpendicular to the inner surface. To enable quantitative comparisons to be made, the DNS results are represented in their dimensionless form $(u^* - \langle u^* \rangle)/(\varepsilon\omega L)$ and $(w^* - \langle w^* \rangle)/(\varepsilon\omega\ell_c)$ with $\ell_c = 2\pi R_i$.

2.5.1 Results for Constant Eccentricity

Leading Order Velocity Field

The axial and azimuthal components of the oscillatory velocity obtained from the DNS, expressed in the dimensionless form $(u^* - \langle u^* \rangle)/(\varepsilon\omega L)$ and $(w^* - \langle w^* \rangle)/(\varepsilon\omega\ell_c)$, are compared in figure 2.4 with the theoretical predictions $(u_0, w_0) = \text{Re}\left[\text{ie}^{\text{i}t}(U,W)\right]$. Velocity distributions are given for $t = \omega t^* = \pi$ at four different sections $x = (0, 0.25, 0.5, 0.75)$. In plotting the theoretical predictions, the coordinate η is measured perpendicular to the inner surface. Note that upward (cranial) / downward (caudal) flow corresponds to negative / positive values of the axial velocity.

As expected, the flow is symmetric with respect to the symmetry plane of the canal,

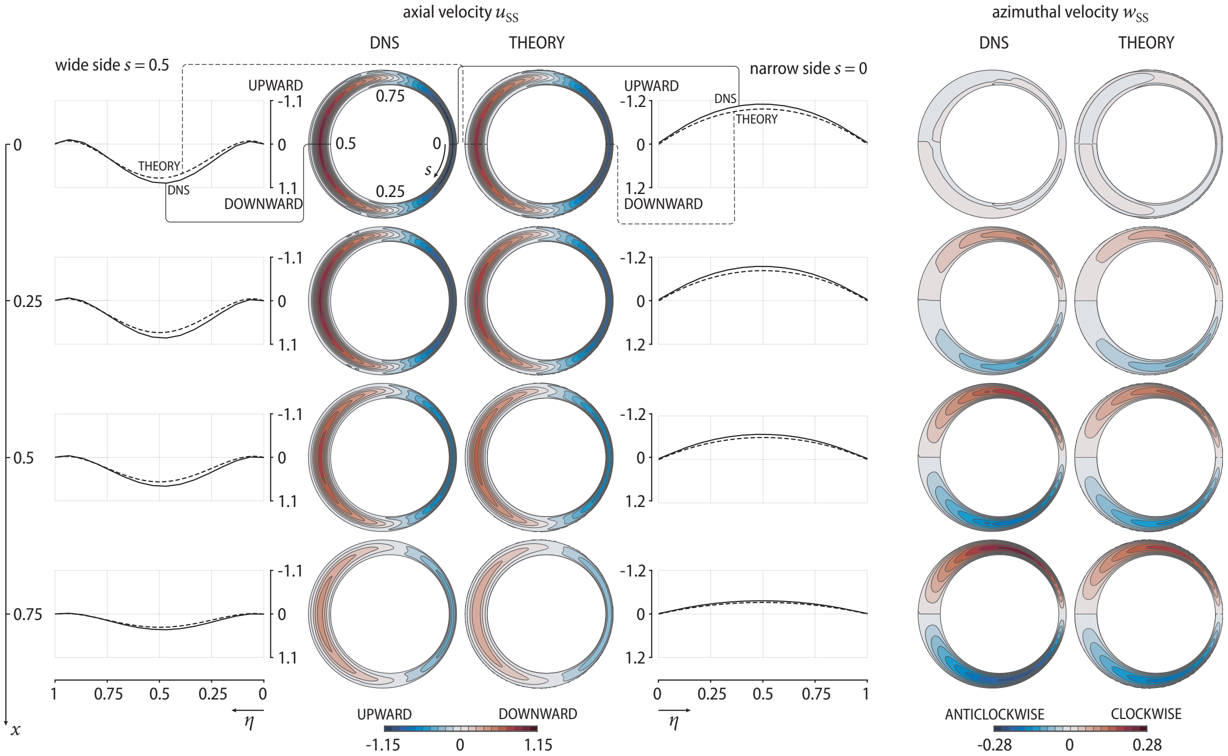

Figure 2.5: Comparison of the steady-streaming velocity components u_{SS} and w_{SS} determined numerically with those predicted by the simplified model. The theoretical predictions are evaluated using the expressions $u_{SS} = \langle u_1 \rangle(x, \eta, s)$ and $w_{SS} = \langle w_1 \rangle(x, \eta, s)$ given in (2.32) and (2.33), with the normalized transverse coordinate η taken to be perpendicular to the inner surface. To enable quantitative comparisons to be made, the DNS results are represented in their dimensionless form $u_{SS} = \langle u^* \rangle / (\varepsilon^2 \omega L)$ and $w_{SS} = \langle w^* \rangle / (\varepsilon^2 \omega \ell_c)$ with $\ell_c = 2\pi R_i$.

defined by $s = 0$ and $s = 0.5$. The magnitude of the axial velocities is seen to decrease with the axial coordinate, to eventually vanish at the closed end of the canal $x = 1$. By way of contrast, the magnitude of the azimuthal velocity, shown on the right-hand side of the figure, tends to increase along the length of the spinal canal, as needed to accommodate the flow recirculation. At the instant of time $t = \omega t^* = \pi$ selected in the figure, the flow moves downwards in the narrow part of the canal and upwards in the wide part. Since viscous effects are more prominent in the narrow regions (i.e. around $s = 0$), the largest peak velocities are found at $s = 0.5$.

To enable a more precise quantitative comparison, profiles of axial velocity are plotted across the canal at $s = 0.5$ (left) and $s = 0$ (right). The velocity profiles obtained analytically are symmetric in both locations, since the model does not take into account curvature effects. However, the numerical results, obtained with large but finite curvature $R_i/h_c = 4$, display slight asymmetries, with peak velocities lying closer to the inner surface $\eta = 0$. The relative difference in centerline velocity, measured by the value of $|u_0 - (u^* - \langle u^* \rangle)|/|u_0|$ at $\eta = 0.5$, varies over the course of the oscillation cycle. This relative difference is of the order of 9% when the flow rate is maximum at $t = \pi/2$ (upward flow) and at $t = 3\pi/2$ (downward flow) and of the order of 15% when the flow rate reverses direction at $t = 0$ and $t = \pi$, the flow in the latter instant of time being represented in figure 2.4. As explained later in the discussion of figure 2.6, both the small asymmetries and the departures in the velocity values are associated with curvature effects resulting from the finite value of the slenderness ratio h_c/R_i.

Steady Streaming

The predictions $u_{SS} = \langle u_1 \rangle$ and $w_{SS} = \langle w_1 \rangle$ for the axial and azimuthal components of the steady-streaming velocity, evaluated from the expressions given in section 2.2.2, are compared in figure 2.5 with the time-averaged values of the DNS velocities, expressed in the dimensionless form $u_{SS} = \langle u^* \rangle/(\varepsilon^2 \omega L)$ and $w_{SS} = \langle w^* \rangle/(\varepsilon^2 \omega \ell_c)$, as needed for consistency. Good agreement is again found between the theoretical predictions and the numerical results, with relative differences in peak values remaining below 15%. As can be inferred from the transverse profiles of u_{SS} at $s = 0$ and $s = 0.5$, the magnitude of the steady-streaming velocities computed in the direct numerical simulations is slightly larger than that predicted by the analytical model. As explained below, the observed departures, on the order of 10% to 15 %, can be attributed to the different approximations incorporated in developing the analytical results, as well as the finite slenderness of the geometry. Although the results presented here have been obtained for $\alpha = 3$, preliminary direct numerical simulations at $\alpha = 10$ also corroborate the good agreement between the theoretical and the numerical results at more realistic Womersley numbers, commonly observed in human beings.

The resulting axial velocities are found to be mainly positive (caudal) where the canal

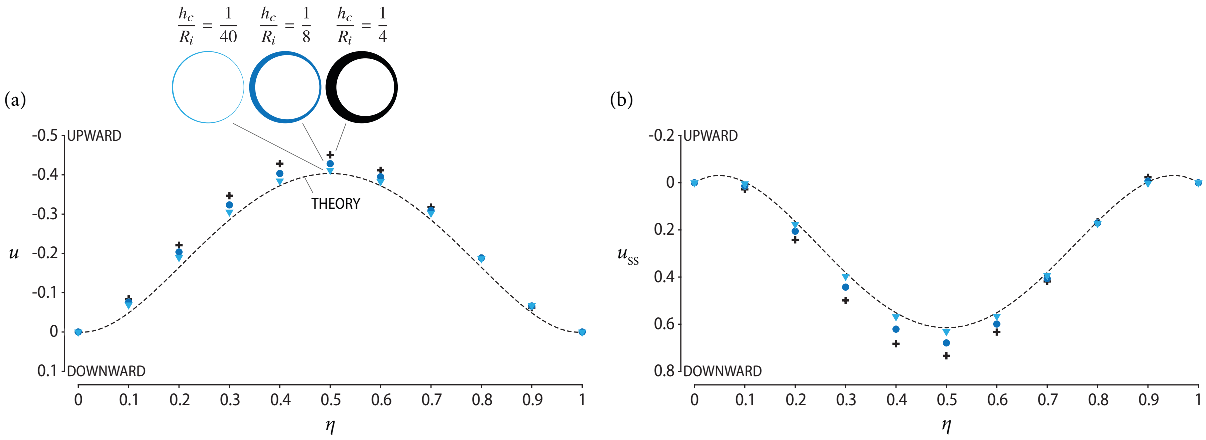

Figure 2.6: Profiles of axial velocity at $x = 0.5$ and $s = 0.5$ for three different values of h_c/R_i, including the instantaneous pulsating component $(u^* - \langle u^* \rangle)/(\varepsilon\omega L)$ evaluated at $t = \omega t^* = \pi$ (a), and the time-averaged component $u_{SS} = \langle u^* \rangle/(\varepsilon^2\omega L)$ (b). The dashed lines represent the corresponding theoretical predictions u_0 and $\langle u_1 \rangle$.

width is larger (i.e. values of s around $s = 0.5$) and mostly negative (cranial) where the canal width is smaller (i.e. values of s around $s = 0$), in agreement with previous results. The flow is symmetric with respect to the plane $s = 0$ and $s = 0.5$, where $w_{SS} = 0$, with the fluid moving azimuthally in the direction of decreasing canal width. It is of interest that the magnitude of u_{SS} decreases away from the entrance (i.e. for increasing values of x) while that of w_{SS} increases, as needed to accommodate flow recirculation.

The small discrepancies observed between the numerical simulations and the theoretical predictions can be attributed to the simplifications introduced in developing the theoretical model. To investigate the inaccuracies associated with the assumption of slender flow, stated in (2.1), computations were performed in more slender canals with smaller widths $h_c = R_e - R_i$, such that $h_c/R_i = 1/8$ and $h_c/R_i = 1/40$. Resulting profiles of axial velocity at $x = 0.5$ and $s = 0.5$ are plotted in figure 2.6 along with those of the previous calculations, corresponding to $h_c/R_i = 1/4$. The pulsating and time-averaged components $(u^* - \langle u^* \rangle)/(\varepsilon\omega L)$ and $\langle u^* \rangle/(\varepsilon^2\omega L)$ are compared with the functions u_0 and $\langle u_1 \rangle$. As can be seen, as effects of curvature become less important for decreasing values of h_c/R_i, the associated DNS profiles become more symmetric and tend

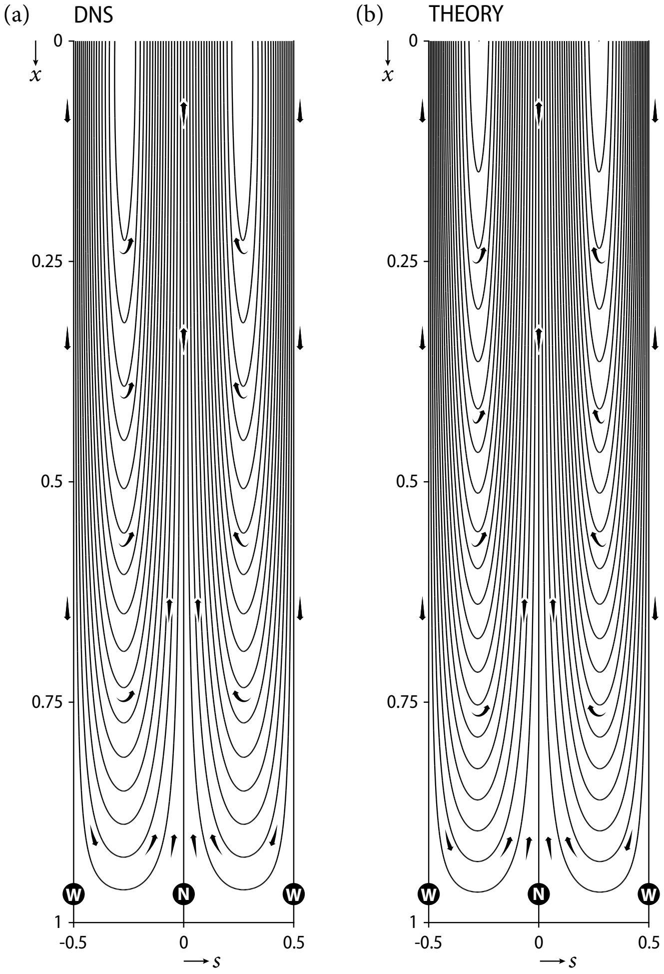

Figure 2.7: Streamlines corresponding to the width-averaged velocities $\int_0^1 u_{\mathrm{SS}}\mathrm{d}\eta$ and $\int_0^1 w_{\mathrm{SS}}\mathrm{d}\eta$ for the flow conditions of figure 2.5. The letters N and W near the bottom indicate the azimuthal location of the narrowest and widest sections.

to approach the theoretical prediction. For instance, when the canal thickness is reduced to $h_c/R_i = 1/40$, the peak values of the pulsating and time-averaged velocity components predicted by the model differ by only 1.5% and 3.5% from the corresponding DNS values.

The long-term Eulerian bulk flow induced by the steady streaming can be characterized by representing on an $s-x$ plane the streamlines associated with the width-averaged values of the axial and azimuthal velocity components $\int_0^1 u_{\mathrm{SS}}\mathrm{d}\eta$ and $\int_0^1 w_{\mathrm{SS}}\mathrm{d}\eta$. Results corresponding to the computation of figure 2.5 are shown on the left-hand side of figure 2.7, with small arrows added to indicate the direction of the flow. The separation between streamlines characterizes the velocity magnitude, with smaller spacing corresponding to larger speeds. The resulting streamlines are very similar to those corresponding to the theoretical predictions, represented in the accompanying right-hand-side plot (figure 2.7b). The streamlines help visualize the flow features previously discussed. The fluid is seen to enter along the wide part of the canal and leave along the narrow part, recirculation occurring at a faster rate towards the closed end, in agreement with the velocity contours shown in figure 2.5.

2.5.2 Results for Variable Eccentricity

To investigate effects of nonuniform eccentricity of the canal section, additional integrations were performed for the model geometry shown in figure 2.3(c). Streamlines corresponding to the width-averaged values $\int_0^1 u_{\mathrm{SS}} \mathrm{d}\eta$ and $\int_0^1 w_{\mathrm{SS}} \mathrm{d}\eta$ of the axial and azimuthal velocity components are shown in figure 2.8.

The flow direction is reversed between contiguous recirculating cells, so that in the top and bottom regions the flow is downwards at $s = 0.5$ and upwards at $s = 0$, while in the intermediate region the flow is upwards at $s = 0.5$ and downwards at $s = 0$. The streamlines separating the three distinct regions include stagnation points at the symmetry plane $s = 0$ and $s = 0.5$, around which the flow exhibits a local counterflow configuration. The streamline spacing is used to indicate the magnitude of the velocity, which shows very different values in the different regions, smaller at larger distances from the entrance. The results indicate that the time-averaged motion is virtually absent in the bottom recirculating region, where the velocities are three orders of magnitude smaller than those found in the top recirculating region, in agreement with previous findings [13].

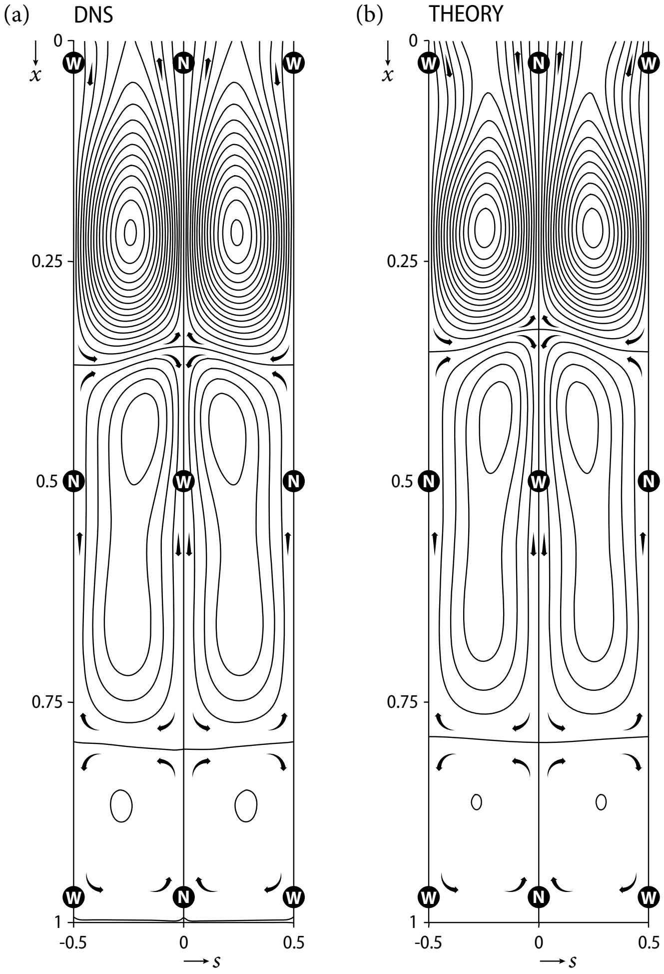

Figure 2.8: Streamlines corresponding to the width-averaged velocities $\int_0^1 \langle u_{\mathrm{SS}} \rangle \mathrm{d}\eta$ and $\int_0^1 \langle w_{\mathrm{SS}} \rangle \mathrm{d}\eta$ for the variable-eccentricity model geometry of figure 2.3(c). The letters N and W indicate the azimuthal location of the narrowest and widest sections respectively.

2.6 Conclusions

A model of the velocity field of cerebrospinal fluid in the spinal canal has been found analytically. The flow is assumed to be doubly slender, following the conditions in (2.1), and the Womersley number α and dimensionless wave number k are assumed to be order unity while the parameter measuring the limited compliance ε, effectively measuring the stroke volume compared to the total volume of fluid in the canal, is assumed to be small. Using this small parameter, all variables are expanded asymptotically. The leading order velocity field due to the intracranial pressure variation is found to be oscillatory with a zero mean. The velocity field found at order ε is found to have a nonzero mean and is known as Eulerian steady streaming. By taking a Lagrangian view, Stokes drift is found to be an additional steady component to the first-order velocity field.

Results for the velocity are presented for a simplified geometry, then verified by comparison to full DNS. Notably, the root-mean-square values of the velocity depend non-monotonically on the parameters α, β, and k and show local maxima for $\alpha \approx 3$, $\beta \approx 0.4$, and $k \approx 0.5$. The axial velocity, for given values of these parameters, tends towards the cranial vault on the narrow side of the canal and away from the cranial vault on the wide side of the canal. For a canal with varying eccentricity, this leads to closed recirculation regions, as the narrow and wide sides of the canal alternate along the length of the canal. The DNS shows good agreement with the simplified model and increasingly good agreement as the computational domain becomes more slender.

This chapter, in part, is a reprint of the material published in the *Journal of Fluid Mechanics*, titled “On the dispersion of a drug delivered intrathecally in the spinal canal,” by J. J. Lawrence, W. Coenen, A. L. Sánchez, G. Pawlak, C. Martínez-Bazán, V. Haughton, and J. C. Lasheras, (2019) 861, 679-720. The dissertation author was the primary investigator and author of this paper. This chapter, in part, is also a reprint of the material published in *Applied Mathematical Modelling*, titled “Modelling and direct numerical simulation of flow and solute dispersion in the spinal subarachnoid space,” by C. Gutiérrez-Montes, W. Coenen, J. J. Lawrence, C. Martínez-Bazán, A. L. Sánchez, and J. C. Lasheras (2021), 94, 516-533. Cándido Gutiérrez-Montes was the primary author of this paper.

Chapter 3

Transport of Solutes with Density Equal to that of CSF

3.1 Characteristic Scales

The velocity field in the spinal canal determines the convective transport of the drug injected in the lumbar region. Besides the characteristic time associated with the pulsating flow ω^{-1}, we have seen that the time-averaged Lagrangian motion introduces a second characteristic time scale, the residence time $\varepsilon^{-2}\omega^{-1}$. Molecular diffusion is characterized by the solute diffusivity κ, typical values of which are of the order of $\kappa \simeq 5 \times 10^{-10}$ m^2/s for chemotherapy drugs such as methotrexate [4], with even larger values pertaining to the radioactive tracers used in exploratory radiological imaging. The associated Schmidt number ν/κ, defined as the ratio of the kinematic viscosity to the molecular diffusivity, is very large, of the order of a few thousand. Diffusion occurs primarily in the direction transverse to the width of the canal, with associated characteristic times h_c^2/κ, whereas the times characterizing axial and azimuthal diffusion, given by L^2/κ and ℓ_c^2/κ, are much longer due to the slenderness of the flow, so that these processes play a negligible role and can be discarded in the description.

To anticipate the relative importance of diffusion in the transport of the solute along the SSAS, it is of interest to compare the two flow characteristic times ω^{-1} and $\varepsilon^{-2}\omega^{-1}$ identified above with the diffusion time $h_c^2/\kappa = S\alpha^2\omega^{-1}$, expressed in terms of the square of the Womersley number $\alpha^2 = \omega h_c^2/\nu$, which is of order unity for the CSF flow in the spinal canal. The comparison of the large values $S \sim 1000$ of the Schmidt number with the typical values of the parameter $\varepsilon \sim 1/50$ suggests that the distinguished limit $S \sim \varepsilon^{-2}$ applies under most conditions of interest for intrathecal drug delivery, for which the diffusion times h_c^2/κ are comparable to the characteristic residence time $\varepsilon^{-2}\omega^{-1}$ of the fluid particles in the spinal canal. As a result, in the limit $S \sim \varepsilon^{-2}$ the temporal variation of the solute concentration is determined by the combined effects of the time-averaged Lagrangian convection and the diffusion across the canal width. The latter will be seen to become dominant for solutes with smaller values of $S \ll \varepsilon^{-2}$, causing the solute concentration to be uniform across the canal at leading order and resulting in a simpler transport equation involving the width-averaged Lagrangian velocities $\int_0^1 u_{\mathrm{L}} \mathrm{d}\eta$ and $\int_0^1 w_{\mathrm{L}} \mathrm{d}\eta$.

The variation of the solute concentration in the short time scale ω^{-1} occurs through small fluctuations of order ε. For solutes with Schmidt numbers $S \sim 1$, the interactions of these nonuniform fluctuations with the pulsating velocity field will be shown to lead to an additional dispersion mechanism, with transport rates that are seen to be of the order of (although significantly smaller than) those of the time-averaged Lagrangian convection. We shall see that this shear-enhanced dispersion, which has been shown to be an important transport mechanism in applications involving oscillatory gaseous flow, such as high-frequency ventilation [24], becomes less effective as the value of S increases, and is entirely negligible for the Schmidt numbers typical of drugs delivered intrathecally, for which transport relies mainly on Lagrangian convection.

3.2 Solute Transport

For the curvilinear coordinates (x,y,s) the transport equation for a solute of molecular diffusivity κ with concentration c takes the form

$$\frac{\partial c}{\partial t}+\varepsilon\left(u\frac{\partial c}{\partial x}+v\frac{\partial c}{\partial y}+\frac{w}{\ell}\frac{\partial c}{\partial s}\right)=\frac{1}{\alpha^2 S}\frac{\partial^2 c}{\partial y^2}, \tag{3.1}$$

where $\alpha \sim 1$ is the Womersley number and $S=\nu/\kappa$ is the Schmidt number. The diffusion term in the above equation only involves derivatives in the y direction, a simplification that follows from the slenderness condition (2.1). Effects of second-order derivatives in the azimuthal and axial direction are anticipated to introduce corrections that are of order $(h_c/\ell_c)^2$ and $(h_c/L)^2$, respectively, which are not described in the present development, consistent with the lubrication approximation used in computing the velocity field. The analysis below will be performed for the case of impermeable bounding surfaces, yielding boundary conditions

$$\frac{\partial c}{\partial y}=0 \quad \text{at } y=0,h. \tag{3.2}$$

Consistent with previous work [75] and chapter 2, we introduce a normalized transverse coordinate $\eta = y/h$ involving the local time-varying canal width $h(x,s,t)$. Also, because of the anticipated slow evolution of the concentration in the canal, with characteristic transport times $\varepsilon^{-2}\omega^{-1}$, the problem is analyzed with a two-time formalism that includes the long time scale $\tau=\varepsilon^2 t$ in addition to the short time scale t. The resulting concentration field $c(x,\eta,s,t,\tau)$, assumed to be 2π periodic in t, satisfies the transport problem

$$\begin{aligned}\frac{\partial c}{\partial t} &- \varepsilon\frac{\partial h'}{\partial t}\frac{\eta}{h}\frac{\partial c}{\partial \eta}+\varepsilon^2\frac{\partial c}{\partial \tau}+\varepsilon\left[u\left(\frac{\partial c}{\partial x}-\frac{\partial h}{\partial x}\frac{\eta}{h}\frac{\partial c}{\partial \eta}\right)\right.\\ &+ \left.\frac{v}{h}\frac{\partial c}{\partial \eta}+\frac{w}{\ell}\left(\frac{\partial c}{\partial s}-\frac{\partial h}{\partial s}\frac{\eta}{h}\frac{\partial c}{\partial \eta}\right)\right]=\frac{1}{\alpha^2 S h^2}\frac{\partial^2 c}{\partial \eta^2}; \quad \frac{\partial c}{\partial \eta}=0 \quad \text{at } \eta=0,1\end{aligned} \tag{3.3}$$

as follows from (3.1).

The problem will be solved by expressing the solute concentration in the expansion form

$$c = c_0 + \varepsilon c_1 + \varepsilon^2 c_2 + \cdots, \tag{3.4}$$

consistent with (2.9). All expansion terms $c_i(x,\eta,s,t,\tau)$ for $i = 0,1,2,\cdots$ are assumed to be expressible in the form $c_i = \langle c_i \rangle + \tilde{c}_i$, where the average in the short time scale $\langle c_i \rangle(x,\eta,s,\tau) = \frac{1}{2\pi}\int_t^{t+2\pi} c_i \, \mathrm{d}t$ varies in the long-time scale τ, while the harmonic functions $\tilde{c}_i(x,\eta,s,t,\tau)$ carry the short-time dependence. Introducing (2.9) and (3.4) into (3.3) and collecting terms in increasing powers of ε yield a series of problems that can be solved sequentially, as done below in the two distinguished limits $S = O(\varepsilon^{-2})$ and $S = O(1)$.

3.2.1 Solute Transport for $\sigma = \varepsilon^2 S \sim 1$

We begin by considering the clinically significant case of large values of the Schmidt number $S = \nu/\kappa \sim \varepsilon^{-2}$, corresponding to most drugs used in ITDD procedures. In this distinguished limit, the diffusion time across the canal h_c^2/κ is comparable to the characteristic residence time $\varepsilon^{-2}\omega^{-1}$, and therefore much larger than the oscillation time $\omega^{-1} \sim h_c^2/\nu$, so that interactions between the short-time fluctuations of concentration and velocity do not lead to appreciable enhancement of the solute dispersion. We begin by rewriting the Schmidt number in the starting equation (3.3) in the rescaled form $\sigma = \varepsilon^2 S$, with $\sigma \sim 1$.

At $O(1)$ the solution provides

$$\frac{\partial c_0}{\partial t} = 0 \quad \rightarrow \quad c_0 = c_0(x,\eta,s,\tau), \tag{3.5}$$

indicating that at leading order the concentration evolves only in the long time scale. The short-time variation of the concentration is limited to the corrections c_1, which are described by the problem that arises at the following order, given by

$$\frac{\partial c_1}{\partial t} = -u_0\frac{\partial c_0}{\partial x} - \frac{w_0}{\ell}\frac{\partial c_0}{\partial s} - \left[v_0 - \left(\frac{\partial h_0'}{\partial t} + \frac{\partial \bar{h}}{\partial x}u_0 + \frac{1}{\ell}\frac{\partial \bar{h}}{\partial s}w_0\right)\eta\right]\frac{1}{\bar{h}}\frac{\partial c_0}{\partial \eta}. \tag{3.6}$$

Since the dependence on t enters in (3.6) only through the harmonic functions u_0, v_0, w_0, and $\partial h_0'/\partial t$, to be evaluated using the expressions (2.14), straightforward integration provides

$$\begin{aligned} c_1 &= -\int u_0 \mathrm{d}t\,\frac{\partial c_0}{\partial x} - \int w_0 \mathrm{d}t\,\frac{1}{\ell}\frac{\partial c_0}{\partial s} - \int v_0 \mathrm{d}t\,\frac{1}{\bar{h}}\frac{\partial c_0}{\partial \eta} \\ &+ \left(h_0' + \int u_0 \mathrm{d}t\,\frac{\partial \bar{h}}{\partial x} + \int w_0 \mathrm{d}t\,\frac{1}{\ell}\frac{\partial c_0}{\partial s}\right)\frac{\eta}{\bar{h}}\frac{\partial c_0}{\partial \eta} + \langle c_1\rangle \end{aligned} \tag{3.7}$$

including the time-averaged value $\langle c_1\rangle(x,\eta,s,\tau)$ and the harmonic functions h_0', $\int u_0 \mathrm{d}t$, $\int v_0 \mathrm{d}t$, and $\int w_0 \mathrm{d}t$ given in (2.14) and (2.54).

The evolution equation for c_0 emerges at the following order. Collecting terms of $O(\varepsilon^2)$ in (3.3) and taking the time average leads to the convection-diffusion equation

$$\frac{\partial c_0}{\partial \tau} + u_{\mathrm{L}}\left(\frac{\partial c_0}{\partial x} - \frac{\partial \bar{h}}{\partial x}\frac{\eta}{\bar{h}}\frac{\partial c_0}{\partial \eta}\right) + \frac{v_{\mathrm{L}}}{\bar{h}}\frac{\partial c_0}{\partial \eta} + \frac{w_{\mathrm{L}}}{\ell}\left(\frac{\partial c_0}{\partial s} - \frac{\partial \bar{h}}{\partial s}\frac{\eta}{\bar{h}}\frac{\partial c_0}{\partial \eta}\right) = \frac{1}{\alpha^2\sigma\bar{h}^2}\frac{\partial^2 c_0}{\partial \eta^2}, \tag{3.8}$$

involving the time-averaged Lagrangian velocities (2.57)–(2.59) and the rescaled Schmidt number $\sigma = \varepsilon^2 S \sim 1$. Equation (3.8) is to be integrated for a given initial distribution $c_0 = c_i(x,\eta,s)$ with the boundary conditions $\partial c_0/\partial\eta = 0$ at $\eta = 0, 1$. An integral equation for the total amount of solute contained between a given section x and the end of the canal follows from integrating (3.8) to yield

$$\frac{\partial}{\partial \tau}\left\{\int_x^1\left[\ell\int_0^1\left(\bar{h}\int_0^1 c_0 \mathrm{d}\eta\right)\mathrm{d}s\right]\mathrm{d}x\right\} = \ell\int_0^1 \bar{h}\left(\int_0^1 u_{\mathrm{L}} c_0 \mathrm{d}\eta\right)\mathrm{d}s, \tag{3.9}$$

involving the solute flux across section x

$$\phi_c = \ell\int_0^1\left(\int_0^1 u_{\mathrm{L}} c_0 \mathrm{d}\eta\right)\bar{h}\,\mathrm{d}s. \tag{3.10}$$

It is also worth noting that one may alternatively write the problem (3.8) in the form

$$\frac{\partial c_0}{\partial \tau}+u_{\mathrm{L}}\frac{\partial c_0}{\partial x}+v_{\mathrm{L}}\frac{\partial c_0}{\partial y}+\frac{w_{\mathrm{L}}}{\ell}\frac{\partial c_0}{\partial s}=\frac{1}{\alpha^2\sigma}\frac{\partial^2 c_0}{\partial y^2};\quad \frac{\partial c_0}{\partial y}=0 \text{ at } y=0,\bar{h}(x,s), \tag{3.11}$$

obtained from (3.8) by using the relation $y=\eta\bar{h}(x,y)$ to express u_{L}, v_{L}, and w_{L} as functions of (x,y,s). Despite the apparent simplicity of (3.11), the associated computational domain varies in time according to $0 \leq y \leq h(x,s,t)$, so that the more complicated equation (3.8), involving a transverse coordinate with normalized constant bounds $0 \leq \eta \leq 1$, offers computational advantages.

3.2.2 Solute Transport for $1 \ll S \ll \varepsilon^{-2}$

One can rewrite simpler descriptions of the above equation for extreme values of $\sigma=\varepsilon^2 S$. For example, for $\sigma \gg 1$, corresponding to tracers with $S \gg \varepsilon^{-2}$, diffusion is entirely negligible, with the result that the fluid particle conserves its initial concentration at all times. On the other hand, in the opposite limit $\sigma \ll 1$ corresponding to values $S \ll \varepsilon^{-2}$ (but still sufficiently larger than unity for the analysis leading to (3.8) to remain valid), the transverse diffusion term on the right-hand side of (3.8) becomes dominant. Since $\partial c_0/\partial\eta=0$ at $\eta=0,1$, it follows that the concentration of the solute is uniform across the width of the canal, with small departures of order σ that need not be considered in the first-order approximation. In deriving an equation for $c_0(x,s,\tau)$ it is convenient to remove the singular diffusion term by integrating (3.8) from $\eta=0$ to $\eta=1$ taking into account the condition $\partial c_0/\partial\eta=0$ in evaluating the convective terms, leading to

$$\frac{\partial c_0}{\partial \tau}+\left(\int_0^1 u_{\mathrm{L}}\mathrm{d}\eta\right)\frac{\partial c_0}{\partial x}+\left(\int_0^1 w_{\mathrm{L}}\mathrm{d}\eta\right)\frac{1}{\ell}\frac{\partial c_0}{\partial s}=0 \tag{3.12}$$

involving the width-averaged Lagrangian velocity components (2.62) and (2.63).

3.2.3 Solute Transport for $S \sim 1$

Although the molecular diffusivities of the drugs used in ITDD are always much smaller than the kinematic viscosity, yielding large values of $S = \nu/\kappa \gg 1$, to investigate the role of Taylor dispersion it is of interest to consider the transport of solutes with $S = \nu/\kappa \sim 1$. In this distinguished limit the diffusion time across the canal h_c^2/κ is comparable to the oscillation time $\omega^{-1} \sim h_c^2/\nu$, and therefore much smaller than the characteristic residence time $\varepsilon^{-2}\omega^{-1}$. As a result, the leading-order time-averaged solute concentration $\langle c_0 \rangle(x,s,\tau)$ becomes independent of the transverse coordinate η. We shall see that the small short-time fluctuations of the concentration described by the harmonic function $\tilde{c}_1$ are essential in the description, in that their interactions with the oscillating velocity provide an additional dispersion mechanism for the solute, described in the time-averaged transport equation for $\langle c_0 \rangle(x,s,\tau)$ through apparent diffusion rates proportional to Taylor diffusivities.

At $O(1)$ the problem (3.3) becomes

$$\frac{\partial c_0}{\partial t} = \frac{1}{\alpha^2 S \bar{h}^2}\frac{\partial^2 c_0}{\partial \eta^2}, \quad \frac{\partial c_0}{\partial \eta} = 0 \text{ at } \eta = 0,1, \tag{3.13}$$

with $c_0 = \langle c_0 \rangle + \tilde{c}_0$. An equation for $\langle c_0 \rangle$ follows from taking the time average of (3.13) to yield

$$0 = \frac{\partial^2 \langle c_0 \rangle}{\partial \eta^2}, \quad \frac{\partial \langle c_0 \rangle}{\partial \eta} = 0 \text{ at } \eta = 0,1, \tag{3.14}$$

which can be readily integrated to give $\partial \langle c_0 \rangle / \partial \eta = 0$. The complex function $\tilde{C}_0$ that determines the leading-order harmonic contribution $\tilde{c}_0 = \mathrm{Re}(\mathrm{e}^{\mathrm{i}t}\tilde{C}_0)$ is identically zero, as can be seen by integrating

$$\mathrm{i}\tilde{C}_0 = \frac{1}{\alpha^2 S \bar{h}^2}\frac{\partial^2 \tilde{C}_0}{\partial \eta^2}, \quad \frac{\partial \tilde{C}_0}{\partial \eta} = 0 \text{ at } \eta = 0,1. \tag{3.15}$$

Consequently, at this order the solution reduces to

$$c_0 = \langle c_0 \rangle = c_0(x, s, \tau). \tag{3.16}$$

At $O(\varepsilon)$ the transport problem (3.3) yields

$$\frac{\partial c_1}{\partial t} + u_0 \frac{\partial c_0}{\partial x} + \frac{w_0}{\ell}\frac{\partial c_0}{\partial s} = \frac{1}{\alpha^2 S \bar{h}^2}\frac{\partial^2 c_1}{\partial \eta^2}, \quad \frac{\partial c_1}{\partial \eta} = 0 \text{ at } \eta = 0, 1 \tag{3.17}$$

for the first-order correction c_1. The leading-order velocity components satisfy $\langle u_0 \rangle = \langle w_0 \rangle = 0$, so that the time average of (3.17) provides

$$0 = \frac{\partial^2 \langle c_1 \rangle}{\partial \eta^2}, \quad \frac{\partial \langle c_1 \rangle}{\partial \eta} = 0 \text{ at } \eta = 0, 1, \tag{3.18}$$

which readily yields $\langle c_1 \rangle = \langle c_1 \rangle(x, s, \tau)$. The harmonic fluctuation $\tilde{c}_1$, needed in the following development, is determined by integration of

$$\frac{1}{\alpha^2 S \bar{h}^2}\frac{\partial^2 \tilde{c}_1}{\partial \eta^2} - \frac{\partial \tilde{c}_1}{\partial t} = u_0 \frac{\partial c_0}{\partial x} + \frac{w_0}{\ell}\frac{\partial c_0}{\partial s}, \quad \frac{\partial \tilde{c}_1}{\partial \eta} = 0 \text{ at } \eta = 0, 1. \tag{3.19}$$

The solution reduces simply to

$$\tilde{c}_1 = -\left(\int u_0 \mathrm{d}t\right)\frac{\partial c_0}{\partial x} - \left(\int w_0 \mathrm{d}t\right)\frac{1}{\ell}\frac{\partial c_0}{\partial s} \qquad \text{for} \quad S \gg 1, \tag{3.20}$$

when the diffusion term in (3.19) becomes negligibly small, whereas in the general case $S \sim 1$ the solution is more complicated and requires consideration of the variation with η of the axial and azimuthal velocity components $u_0 = \mathrm{Re}\left(\mathrm{i}e^{\mathrm{i}t} U\right)$ and $w_0 = \mathrm{Re}\left(\mathrm{i}e^{\mathrm{i}t} W\right)$. The functions $U(x, \eta, s)$ and $W(x, \eta, s)$, shown in (2.15), can be used to write

$$u_0 = \mathrm{Re}\left(\mathrm{i}e^{\mathrm{i}t}\frac{\mathrm{d}P'}{\mathrm{d}x} G\right) \quad \text{and} \quad w_0 = \mathrm{Re}\left(\mathrm{i}e^{\mathrm{i}t}\frac{1}{\ell}\frac{\partial \hat{P}}{\partial s} G\right), \tag{3.21}$$

where the dependence on η is carried by the function

$$G = 1 - \frac{\cosh\left[\frac{\alpha\bar{h}}{2}\frac{1+\mathrm{i}}{\sqrt{2}}(2\eta - 1)\right]}{\cosh\left[\frac{\alpha\bar{h}}{2}\frac{1+\mathrm{i}}{\sqrt{2}}\right]}. \tag{3.22}$$

The functions $P'(x)$ and $\hat{P}(x,s)$ in (3.21), independent of η, define the spatial variation of the leading-order pressure functions p' and $\hat{p}$. Using (3.21) together with $\tilde{c}_1 = \mathrm{Re}\left(\mathrm{e}^{\mathrm{i}t}\tilde{C}_1\right)$ in (3.19) yields

$$\frac{1}{\alpha^2 S\bar{h}^2}\frac{\partial^2\tilde{C}_1}{\partial\eta^2} - \mathrm{i}\tilde{C}_1 = \mathrm{i}G\left(\frac{\mathrm{d}P'}{\mathrm{d}x}\frac{\partial c_0}{\partial x} + \frac{1}{\ell}\frac{\partial\hat{P}}{\partial s}\frac{1}{\ell}\frac{\partial c_0}{\partial s}\right), \quad \frac{\partial\tilde{C}_1}{\partial\eta} = 0 \text{ at } \eta = 0, 1. \tag{3.23}$$

which can be integrated to give

$$\tilde{C}_1 = -F\left(\frac{\mathrm{d}P'}{\mathrm{d}x}\frac{\partial c_0}{\partial x} + \frac{1}{\ell}\frac{\partial\hat{P}}{\partial s}\frac{1}{\ell}\frac{\partial c_0}{\partial s}\right), \tag{3.24}$$

where

$$\begin{aligned} F &= \frac{\lambda}{2}\Big[\left(\mathrm{e}^{\lambda}\int_0^1 G\mathrm{e}^{-\lambda\eta}\mathrm{d}\eta + \mathrm{e}^{-\lambda}\int_0^1 G\mathrm{e}^{\lambda\eta}\mathrm{d}\eta\right)\frac{\mathrm{e}^{\lambda\eta} + \mathrm{e}^{-\lambda\eta}}{\mathrm{e}^{\lambda} - \mathrm{e}^{-\lambda}} \\ &+ \mathrm{e}^{-\lambda\eta}\int_0^\eta G\mathrm{e}^{\lambda\bar{\eta}}\mathrm{d}\bar{\eta} - \mathrm{e}^{\lambda\eta}\int_0^\eta G\mathrm{e}^{-\lambda\bar{\eta}}\mathrm{d}\bar{\eta}\Big], \end{aligned} \tag{3.25}$$

with $\lambda = \frac{1+\mathrm{i}}{\sqrt{2}}\sqrt{S}\alpha\bar{h}(x,s)$. The resulting expression for $\tilde{c}_1 = \mathrm{Re}\left(\mathrm{e}^{\mathrm{i}t}\tilde{C}_1\right)$ can be cast in the compact form

$$\tilde{c}_1 = -\left(\int u_a \mathrm{d}t\right)\frac{\partial c_0}{\partial x} - \left(\int w_a \mathrm{d}t\right)\frac{1}{\ell}\frac{\partial c_0}{\partial s} \tag{3.26}$$

by introducing the apparent velocities

$$u_a = \mathrm{Re}\left(\mathrm{i}\mathrm{e}^{\mathrm{i}t}\frac{\mathrm{d}P'}{\mathrm{d}x}F\right) \quad \text{and} \quad w_a = \mathrm{Re}\left(\mathrm{i}\mathrm{e}^{\mathrm{i}t}\frac{1}{\ell}\frac{\partial\hat{P}}{\partial s}F\right). \tag{3.27}$$

Equation (3.25) yields $F = G$ for $S \gg 1$, with the result that $u_a = u_0$ and $w_a = w_0$, so that (3.26) reduces to (3.20) in that limit.

The transport equation for c_0 can be obtained from the analysis of (3.3) at $O(\varepsilon^2)$. The solution can be derived directly by considering the global conservation equation

$$\begin{aligned}\frac{\partial}{\partial t}\left(h\int_0^1 c\,\mathrm{d}\eta\right) &+ \varepsilon^2\frac{\partial}{\partial \tau}\left(h\int_0^1 c\,\mathrm{d}\eta\right)\\ &+ \frac{\varepsilon}{\ell}\left[\frac{\partial}{\partial x}\left(\ell h\int_0^1 uc\,\mathrm{d}\eta\right)+\frac{\partial}{\partial s}\left(h\int_0^1 wc\,\mathrm{d}\eta\right)\right]=0, \qquad (3.28)\end{aligned}$$

obtained by integrating (3.3) between $\eta = 0$ and $\eta = 1$. Writing (3.28) for the two-time formalism and introducing the expansions (2.9) provides

$$\begin{aligned}\bar{h}\frac{\partial c_0}{\partial \tau} &+ \left(\bar{h}\int_0^1 \langle u_1\rangle \mathrm{d}\eta + \int_0^1 \langle h_0' u_0\rangle \mathrm{d}\eta\right)\frac{\partial c_0}{\partial x} + \left(\bar{h}\int_0^1 \langle w_1\rangle \mathrm{d}\eta + \int_0^1 \langle h_0' w_0\rangle \mathrm{d}\eta\right)\frac{1}{\ell}\frac{\partial c_0}{\partial s}\\ &+ \frac{1}{\ell}\frac{\partial}{\partial x}\left(\ell\bar{h}\int_0^1 \langle u_0\tilde{c}_1\rangle \mathrm{d}\eta\right) + \frac{1}{\ell}\frac{\partial}{\partial s}\left(\bar{h}\int_0^1 \langle w_0\tilde{c}_1\rangle \mathrm{d}\eta\right) = 0 \qquad (3.29)\end{aligned}$$

after taking the time average and accounting for the conditions $\partial c_0/\partial\eta = 0$ and $\langle u_0\rangle = \langle w_0\rangle = 0$.

As can be inferred from observation of (2.62) and (2.63), the factors in the apparent convective terms in the first line of (3.29) correspond to the width-averaged Lagrangian velocity components $\int u_{\mathrm{L}}\mathrm{d}\eta$ and $\int w_{\mathrm{L}}\mathrm{d}\eta$, except for the last Stokes-drift terms in (2.62) and (2.63), which are missing in (3.29). The integrals in the second line of (3.29) account for the interactions of the fluctuations of concentration with the fluctuations of velocity. When $S \gg 1$ the fluctuations of concentration, given in (3.20), are not affected by diffusion and the interactions described by the last two terms in (3.29) result in the missing contribution to the Stokes-drift convective transport, as can be seen by using (3.20) to write

$$\frac{1}{\ell}\frac{\partial}{\partial x}\left(\ell\bar{h}\int_0^1\langle u_0\tilde{c}_1\rangle \mathrm{d}\eta\right)+\frac{1}{\ell}\frac{\partial}{\partial s}\left(\bar{h}\int_0^1\langle w_0\tilde{c}_1\rangle \mathrm{d}\eta\right)=$$
$$\frac{1}{\ell}\frac{\partial}{\partial s}\left(\bar{h}\int_0^1\left\langle u_0\int w_0\mathrm{d}t\right\rangle \mathrm{d}\eta\right)\frac{\partial c_0}{\partial x}+\frac{\partial}{\partial x}\left(\bar{h}\int_0^1\left\langle w_0\int u_0\mathrm{d}t\right\rangle \mathrm{d}\eta\right)\frac{1}{\ell}\frac{\partial c_0}{\partial s}, \tag{3.30}$$

Consequently, in the limit $S \gg 1$ the transport equation (3.29) reduces to (3.12), which was derived earlier from (3.8) by considering values of $\sigma = \varepsilon^2 S \ll 1$.

In the general case $S \sim 1$, the effect of transverse diffusion modifies the short-time fluctuations $\tilde{c}_1$, as described by (3.26). In this case, the interactions of these fluctuations with the fluctuations of velocity, described by the nonuniform velocity profiles u_0 and w_0, lead to Taylor dispersion in the azimuthal and axial directions, providing an additional transport mechanism for the solute, supplemental to the convection associated with the time-averaged Lagragian motion. Using (3.26) in evaluating in (3.29) the integrals containing $\tilde{c}_1$ and rearranging the result to isolate the effect of Taylor dispersion lead to

$$\begin{aligned}\bar{h}\frac{\partial c_0}{\partial \tau} &+ \bar{h}\left(\int_0^1 u_{\mathrm{L}}\mathrm{d}\eta\right)\frac{\partial c_0}{\partial x}+\bar{h}\left(\int_0^1 w_{\mathrm{L}}\mathrm{d}\eta\right)\frac{1}{\ell}\frac{\partial c_0}{\partial s}=\frac{1}{\ell}\frac{\partial}{\partial x}\left(\ell D_{xx}\frac{\partial c_0}{\partial x}\right)\\ &+ \frac{1}{\ell}\frac{\partial}{\partial x}\left(D_{xs}\frac{\partial c_0}{\partial s}\right)+\frac{1}{\ell}\frac{\partial}{\partial s}\left(D_{sx}\frac{\partial c_0}{\partial x}\right)+\frac{1}{\ell}\frac{\partial}{\partial s}\left(D_{ss}\frac{1}{\ell}\frac{\partial c_0}{\partial s}\right),\end{aligned} \tag{3.31}$$

involving the width-averaged Lagrangian velocities given in (2.62) and (2.63) along with the

Taylor diffusivities

$$\begin{aligned} D_{xx}(x,s) &= \bar{h}\textstyle\int_0^1 \langle u_0\,(\int u_a \mathrm{d}t)\rangle\,\mathrm{d}\eta \\ D_{xs}(x,s) &= \bar{h}\textstyle\int_0^1 \langle u_0\,(\int (w_a - w_0)\mathrm{d}t)\rangle\,\mathrm{d}\eta \\ D_{sx}(x,s) &= \bar{h}\textstyle\int_0^1 \langle w_0\,(\int (u_a - u_0)\mathrm{d}t)\rangle\,\mathrm{d}\eta \\ D_{ss}(x,s) &= \bar{h}\textstyle\int_0^1 \langle w_0\,(\int w_a \mathrm{d}t)\rangle\,\mathrm{d}\eta. \end{aligned} \tag{3.32}$$

Since $u_a = u_0$ and $w_a = w_0$ for $S \gg 1$, it is clear from the definitions (3.32) that all diffusivities vanish as $S \to \infty$, so that (3.31) naturally reduces to (3.12) in this limit. An integral conservation equation, the counterpart of (3.9) for $S \sim 1$, can be derived by integrating (3.31) to give

$$\frac{\partial}{\partial \tau}\left\{\int_x^1 \left[\ell \int_0^1 c_0 \bar{h}\,\mathrm{d}s\right] \mathrm{d}x\right\} = \phi_c, \tag{3.33}$$

where

$$\phi_c = \ell \int_0^1 \left(\int_0^1 u_{\mathrm{L}} \mathrm{d}\eta\right) c_0 \bar{h}\,\mathrm{d}s - \ell \int_0^1 D_{xx} \frac{\partial c_0}{\partial x} \mathrm{d}s - \int_0^1 D_{xs} \frac{\partial c_0}{\partial s} \mathrm{d}s \tag{3.34}$$

is the solute flux across section x.

3.3 Results for Two Simplified Geometries

The formulation above explicitly defines the solute transport given the geometrical functions $\bar{h}(x,s)$, $\ell(x)$, $\gamma(x,s)$, the parameters β, α, and k, and the initial distribution of solute c_i. Transport results are shown for the simplified geometry with constant eccentricity, the same configuration used in previous work [75] and chapter 2. Since the same parameters β, α, and k are used, the velocities found in chapter 2 are applicable here. The additional case of concentric cylinders is briefly considered as well. This case is not clinically relevant, as the spinal cord and spinal canal are not concentric, but it is of academic interest as the transport behavior has additional features due to the azimuthal symmetry.

3.3.1 Constant Eccentricity

The time-averaged transport equation for the solute takes different forms depending on the value of the Schmidt number. For $S \sim \varepsilon^{-2} \gg 1$, the solute concentration at leading order $c_0(x,\eta,s,\tau)$ is obtained from the reduced transport equation (3.8), involving transverse diffusion across the width of the canal and convective transport, the latter driven by the time-averaged Lagrangian velocity $(u_{\mathrm{L}}, v_{\mathrm{L}}, w_{\mathrm{L}})$. For $S \sim 1$ the solute concentration $c_0(x,s,\tau)$ is found to be uniform across the width of the canal in the first approximation as a result of the dominant effect of transverse diffusion. As seen in the associated transport equation (3.31), convective transport involves the width-averaged axial and azimuthal components of the Lagrangian velocity, while the apparent diffusion terms resulting from the interactions of the small fluctuations of the concentration with the pulsatile flow are expressed in terms of Taylor diffusivities.

The relevant transport coefficients, i.e. u_{L}, v_{L}, and w_{L} in (3.8) and $\int_0^1 u_{\mathrm{L}} \mathrm{d}\eta$, $\int_0^1 w_{\mathrm{L}} \mathrm{d}\eta$, D_{xx}, D_{xs}, D_{sx}, and D_{ss} in (3.31), can be evaluated using the expressions given in chapter 2 for the Eulerian velocity components and wall deformation, along with the expressions given in (3.32) for the Taylor diffusivities. The results depend on the Womersley number α defined in (2.8), which measures the relative importance of viscous forces, and the dimensionless wave number defined in (2.4), which enters in the elastic equation (2.3) relating the pressure with the canal deformation, both order-unity parameters. The Taylor diffusivities (3.32) have an additional dependence on the Schmidt number S, entering in (3.27) through the function F given in (3.25). The geometry of the canal is defined by the inner perimeter $\ell(x)$ and unperturbed canal width $\bar{h}(x,s)$, both order-unity functions. Additionally, a compliance function $\gamma(x,s) \sim 1$ is introduced for generality to describe the spatial variation of the elastic properties of the outer dura membrane.

The diffusion terms in (3.31) describe the dispersion resulting from the interactions of

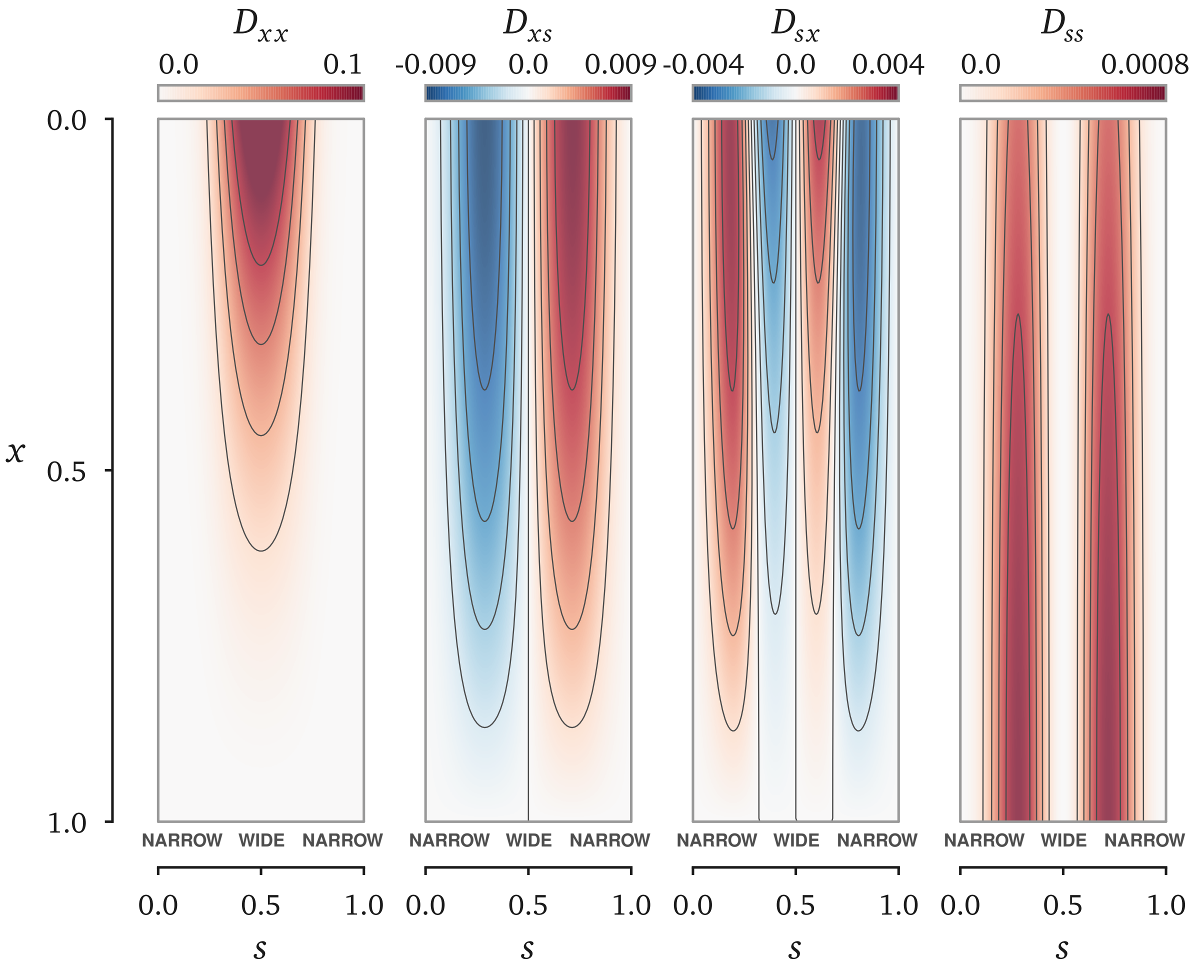

Figure 3.1: The distributions of the Taylor diffusivities for $\beta = 0.5$, $k = 0.5$, and $S = 1$.

the short-time fluctuations of concentration and velocity, the former influenced by transverse diffusion. The relative contribution of this additional transport mechanism to the dispersion of the solute along the canal depends on the values of the Taylor diffusivities (3.32), to be compared with the width-averaged Lagrangian velocities, which determine in (3.31) the convective transport. For the model geometry considered here, the values of $\int_0^1 u_{\mathrm{L}} \mathrm{d}\eta$ and $\int_0^1 w_{\mathrm{L}} \mathrm{d}\eta$ are shown on the left panels of figure 2.2 for $\beta = 0.5$, $\alpha = 3$, and $k = 0.5$. Corresponding distributions of D_{xx}, D_{xs}, D_{sx}, and D_{ss} are given in figure 3.1 for $S = 1$.

A first observation from the numerical results is that, even for this case of very diffusive solutes with $S = 1$, the magnitude of the Taylor diffusivities is relatively small, compared with those of the width-averaged axial and azimuthal Lagrangian velocities. The axial diffusivity exhibits the largest values $D_{xx} \sim 0.1$, while the other three diffusivities remain everywhere smaller than 0.01, with D_{ss} showing the smallest values.

The spatial distributions of axial diffusivity D_{xx} and azimuthal diffusivity D_{ss}, symmetric about $s = 0.5$, show a strong correlation with the distributions of the amplitudes of the oscillatory velocity components $|u_0|$ and $|w_0|$. Thus, the distribution of D_{xx} is concentrated near the entrance in the widest part of of the canal ($s = 0.5$), where the axial motion is more pronounced. Similarly, the distribution of D_{ss} shows two longitudinal bands centered about $s \simeq 0.25$ and $s \simeq 0.75$, corresponding to the peaks of the azimuthal-velocity amplitude $|w_0|$. Outside these distinct regions the diffusivities are found to be negligibly small, that being a result of the quadratic dependence of D_{xx} and D_{ss} on the fluctuations. The diffusivities D_{xs} and D_{sx} are antisymmetric about $s = 0.5$, and therefore show positive and negative values, with spatial distributions that tend to be more uniform than those of D_{xx} and D_{ss}.

Parametric dependences of the Taylor diffusivities are investigated in figure 3.2 by plotting their root-mean-square values. The plots are generated by varying one of the four controlling parameters β, α, k, and S, while keeping the other three constant and equal to the values employed in figure 3.1. Due to the absence of azimuthal motion in axisymmetric canals, for $\beta = 0$ the only nonzero diffusivity is D_{xx}. All diffusivities increase for increasing values of the eccentricity and reach their maximum values at $\beta = 1$. By way of contrast, the curves showing the variations with α, k, and S are non-monotonic, with diffusivities peaking at intermediate values of these controlling parameters. The computations with varying Schmidt number were extended up to $S = 1000$, a value representative of the drugs used in intrathecal-delivery procedures. As can be seen, the resulting diffusivities are negligibly small for $S > 100$, indicating that shear-enhanced dispersion is ineffective under conditions of interest for therapeutical applications, for which the mean Lagrangian motion becomes the dominant transport mechanism. This is to be further

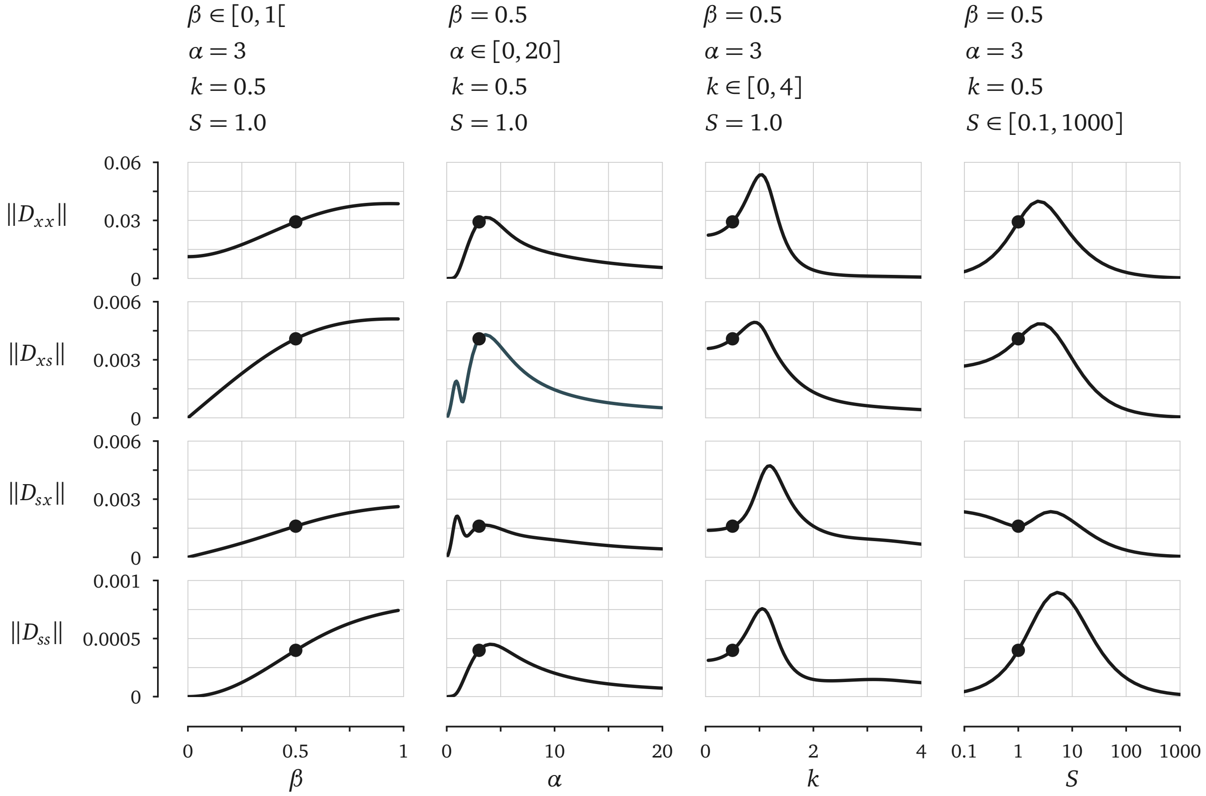

Figure 3.2: The parametric variation of the root-mean-square values of the Taylor diffusivities, with the dots indicating the values corresponding to the distributions shown in figure 3.1.

assessed in the time-dependent computations given below.

Once the time-averaged Lagrangian velocities and Taylor diffusivities are evaluated for given values of the governing parameters and geometry, the computation of the solute dispersion reduces to the integration of a linear transport equation, given in (3.8) for $\sigma = \varepsilon^2 S \sim 1$ and in (3.31) for $S \sim 1$, with the simpler equation (3.12) applying in the intermediate case $1 \ll S \ll \varepsilon^{-2}$. In these equations, convective transport is driven by the time-averaged Lagrangian velocity, given by the sum of the steady-streaming and Stokes-drift components. Taylor dispersion emerges in (3.31) as an additional transport mechanism for solutes with $S \sim 1$. Although this mechanism in principle can be important, in view of the relative magnitude of the width-averaged velocities $\int_0^1 u_\mathrm{L} \mathrm{d}\eta$ and $\int_0^1 w_\mathrm{L} \mathrm{d}\eta$, shown in figure 2.2, and the much smaller Taylor diffusivities, shown in figures 3.1 and 3.2, it can be anticipated that, even for $S \sim 1$, convection largely dominates the transport of the solute under most conditions, as verified in the integrations below. The only exception is that of perfectly axisymmetric canals (i.e. with $\bar{h} = \bar{h}(x)$ and $\gamma = \gamma(x)$), for which the azimuthal motion is absent, with the result that the width-averaged axial velocity along the closed-end canal is identically zero, as follows from (2.61). This case, of some academic interest, is analyzed separately in the next section. The results are, however, of limited practical relevance for solute transport in the spinal canal, because of the lack of azimuthal symmetry in real anatomy. For that reason, the remaining computations shown here consider instead an eccentric canal, a geometry that is more relevant in connection with ITDD applications.

The results given in figures 3.3 and 3.4 correspond to an eccentricity $\beta = 0.5$, a Womersley number $\alpha = 3$, and a nondimensional wave number $k = 0.5$. The corresponding Lagrangian velocity components and associated width-averaged values displayed in figures 2.1 and 2.2, whereas the Taylor diffusivities for $S = 1$ are shown in figure 3.1. The numerical computations, which use a second-order central finite-difference approximation for the spatial discretizations and a Runge-Kutta 4/5 method for time advancement, consider a solute delivered at $\tau = 0$ in a localized region centered about $x = 0.75$. The resulting distributions of width-averaged concentration $\int_0^1 c_0 \mathrm{d}\eta$ as a function of x and s at different instants of time are shown in figure 3.3 for different solute diffusivities. For improved clarity, the azimuthal coordinate in the plots is extended beyond the range $0 < s < 1$, with values of $\int_0^1 c_0 \mathrm{d}\eta$ at $s < 0$ corresponding to those at $1 + s$ and values at $s > 1$ corresponding to those at $s - 1$. The axial distribution of the averaged concentration at each section x, computed according to $\int_0^1 (\bar{h} \int_0^1 c_0 \mathrm{d}\eta) \mathrm{d}s$, is indicated on the side of each individual panel.

Results of integrations of (3.8) for $\sigma = \varepsilon^2 S = 10$ and $\sigma = \varepsilon^2 S = 1$ are shown in figures 3.3(a) and 3.3(b), respectively, while figure 3.3(c) shows results for $1 \ll S \ll \varepsilon^{-2}$, obtained from (3.12), and figure 3.3(d) shows results for $S = 1$, computed with use of (3.31). With the characteristic value of ε being of order $\varepsilon \sim 1/50$ and the Schmidt number of drugs typically used in ITDD procedures being or order $S \sim 1000$, it appears that the conditions investigated

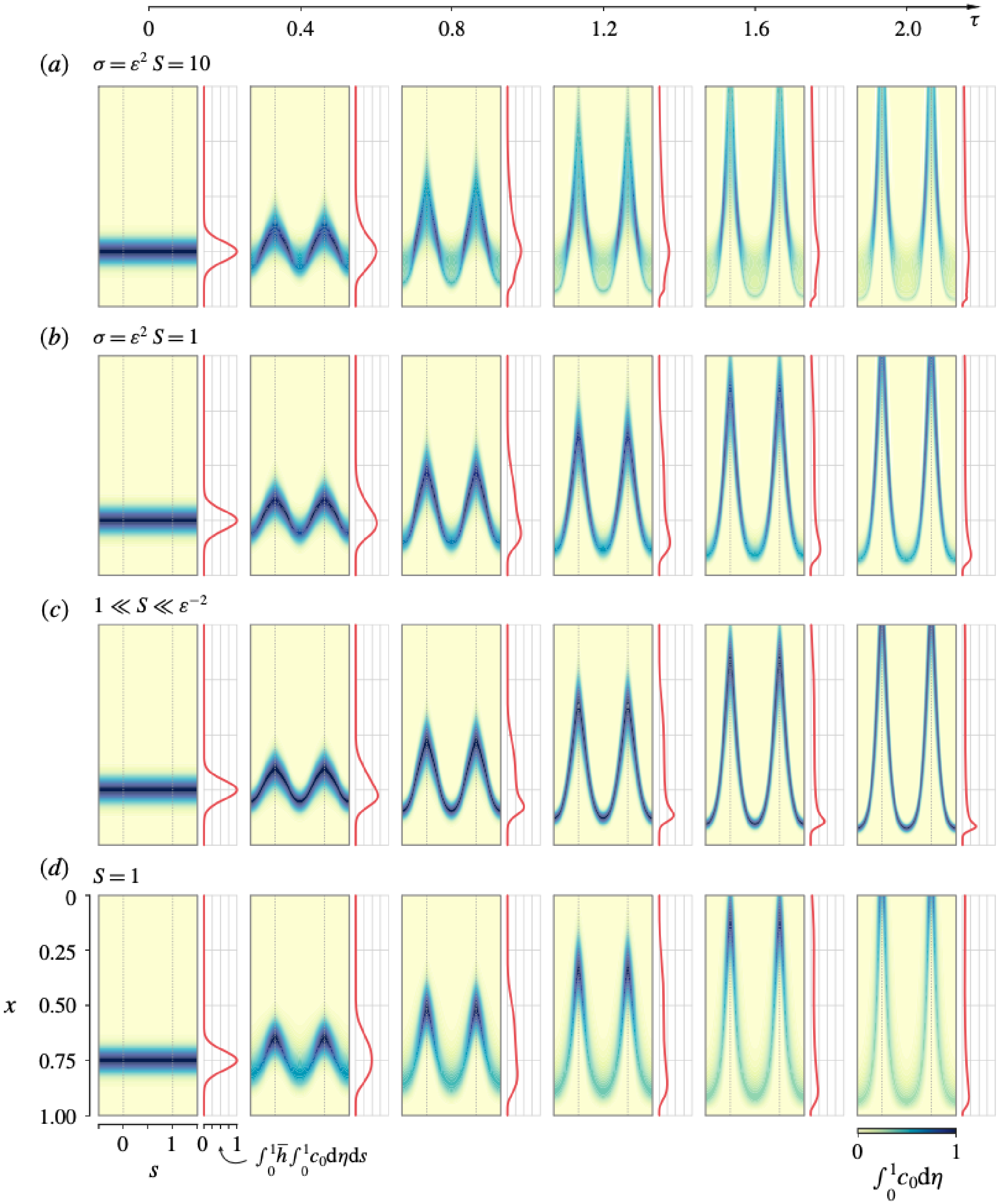

Figure 3.3: Distributions of width-averaged concentration $\int_0^1 c_0 \mathrm{d}\eta$ at different instants of time as obtained numerically for $\beta = 0.5$, $\alpha = 3$, and $k = 0.5$ by integration of (3.8) with $\sigma = 10$ (a) and $\sigma = 1$ (b), by integration of (3.12) (c) and by integration of (3.31) with $S = 1$ (d). The axial distribution of the average concentration at each canal section $\int_0^1 \bar{h} \int_0^1 c_0 \mathrm{d}\eta \mathrm{d}s$ is indicated along the right side of each panel.

in figure 3.3(b) are directly relevant to drug dispersion in the spinal canal, while the results for $\sigma = \varepsilon^2 S = 10$, corresponding to Schmidt numbers of order $S \sim 25,000$, are representative of transport of radioactive or fluorescent tracers, used in clinical studies. On the other hand, the results for $S = 1$, corresponding to mixing of two gases, are included to illustrate effects of Taylor dispersion and the intermediate case $1 \ll S \ll \varepsilon^{-2}$ is included to test the predictive capability of the simplified transport equation (3.12).

For all of the computations shown in figure 3.3 the initial concentration is given by the Gaussian distribution $c_i = \exp[-16^2(x-0.75)^2]$. The integration of (3.8) employs the boundary conditions $\partial c_0/\partial \eta = 0$ at $\eta = 0, 1$, corresponding to impermeable bounding surfaces. Additionally, a boundary condition must be specified for c_0 at the open boundary $x = 0$. Since convection is the only axial transport mechanism in (3.8), the appropriate condition is determined by the sign of u_{L} at $x = 0$, indicated by blue (upward) and red (downward) colors in the upper left circular plot of figure 2.1. In regions of upward flow (negative values of u_{L}) the concentration is given by that within the canal at earlier times, whereas in regions of downward flow (positive values of u_{L}) the concentration is that found outside the canal, assumed to be $c_0 = 0$ in our integrations. The same boundary conditions are used at the canal entrance $x = 0$ when integrating (3.12). On the other hand, the presence of Taylor dispersion in (3.31), involving second-order spatial derivatives, necessitates introduction of suitable modified boundary conditions at the entrance $x = 0$, but not at the closed end $x = 1$, because there the diffusion rate vanishes as a result of the zero values of D_{xx}, D_{xs}, and D_{sx}, which are apparent in the plots of figure 3.1. As discussed by [30] in their study of axial dispersion in a channel with oscillating walls, determination of the entry conditions requires consideration of the flow outside the canal, which would be dependent upon the specific geometry found there. To avoid this complicating aspect of the problem, in the integrations reported in figure 3.3(d) we chose a simplified computational strategy, in which the axial diffusive transport across the boundary at $x = 0$ is eliminated, and in which the axial convective transport is treated as described before, i.e. in regions of inflow the concentration is set to zero, whereas in regions of outflow it is determined by its value within the canal at earlier times.

A notable finding of the numerical integrations in figure 3.3 is the striking qualitative agreement of the different transport patterns. This result implies that the dominant transport mechanism is convection driven by the Lagrangian motion, with the axial velocity u_{L} largely determining the evolution of the solute in all cases. As expected from the distributions of u_{L} shown in figure 2.2, the solute is transported rapidly towards the canal entrance along the preferential path $s = 0$ (or $s = 1$), corresponding to the narrow part of the canal where we find large negative values of u_{L}, regardless of the Schmidt number.

The extent of the effects of Taylor dispersion can be assessed by comparing the snapshots in figure 3.3(d), corresponding to $S = 1$, with the dispersion-free results shown in figure 3.3(c) for the same rescaled times. As can be seen, even for this large-diffusivity case $S = 1$, the differences between both sets of computations are not significant, and are mainly observed in the solute distribution in the low-velocity region near the closed end, where the effect of Taylor dispersion tends to spread the solute concentration. Additional results of integrations of (3.31) for $S = 50$, not shown in figure 3.3, gave solute distributions that are virtually indistinguishable from those shown in figure 3.3(c). These findings, consistent with the quantitative results in figure 3.2, indicate that Taylor dispersion, which is known to play a central role in axial dispersion in axisymmetric or planar configurations, contributes negligibly to the transport of drugs delivered intrathecally in the spinal canal.

For $S \ll \varepsilon^{-2}$ the solute concentration is uniform across the width of the canal in the first approximation, while in the opposite case $S \gg \varepsilon^{-2}$ molecular diffusion is entirely negligible, so that each fluid particle conserves its initial concentration. An intermediate behavior is found in the distinguished limit $S \sim \varepsilon^{-2}$, the case considered in figures 3.3(a) and 3.3(b), where transverse molecular diffusion is significant, but unable completely uniformize the solute concentration across the canal width. As a result, the solute located initially near the bounding surfaces $\eta = 0$ and $\eta = 1$, where the velocity is small, tends to remain at the initial location, an effect that is clearly visible in the computations for $\sigma = \varepsilon^2 S = 10$ in figure 3.3(a). Away from the walls, the solute is convected by the flow, so that the resulting transport pattern in 3.3(a) and 3.3(b) is similar to that found in 3.3(c).

To provide a more direct quantitative assessment of the effects of the Schmidt number on solute dispersion, the value of the solute flux ϕ_c was computed at three different sections $x = (0, 0.25, 0.5)$ for the solute evolutions of figure 3.3 and also for additional computations with $S = 50$ based on (3.31). The value of $\phi_c(x,\tau)$ is evaluated from (3.10) in the integrations for $\sigma = \varepsilon^2 S = 10$ and $\sigma = \varepsilon^2 S = 1$ and from (3.34) in the integrations for $S = 1$ and $S = 50$, with the simpler expression

$$\phi_c = \ell \int_0^1 \left(\int_0^1 u_{\mathrm{L}} \mathrm{d}\eta \right) c_0 \bar{h} \, \mathrm{d}s \tag{3.35}$$

applying in the intermediate limit $1 \ll S \ll \varepsilon^{-2}$. The results are represented in figure 3.4.

Since the solute migrates towards the canal entrance, the corresponding values of ϕ_c are negative. The curves at different sections display the expected delay associated with the distance from the injection location ($x = 0.75$). The differences in the temporal variation of the solute flux between the extreme values of the Schmidt number $\varepsilon^2 S = 10$ and $S = 1$ can be attributed to their distinct transport mechanisms. For the least diffusive case ($\varepsilon^2 S = 10$) the concentration of each fluid particle remains almost constant, so that particles located initially near the center of the canal $\eta = 0.5$, where the velocity is higher, tend to move faster, whereas those near the bounding surfaces $\eta = (0,1)$ move more slowly. By way of contrast, for $S = 1$ the concentration, uniform in η, is convected with the width-averaged velocity, smaller than the peak velocity found near the center. As a result, for $\varepsilon^2 S = 10$ the flux ϕ_c increases earlier than that for $S = 1$, because of the rapid motion of the fluid particles near the center of the canal, but reaches a peak value that is significantly lower, because near-wall fluid particles take a long time to move from the initial location. The differences between the other three curves ($S = 50$, $1 \ll S \ll \varepsilon^2$ and $\sigma = \varepsilon^2 S = 1$) are much smaller, with associated predictions of solute flux differing typically by about 10%. This quantitative agreement suggests that the simplified transport model (3.12), involving only

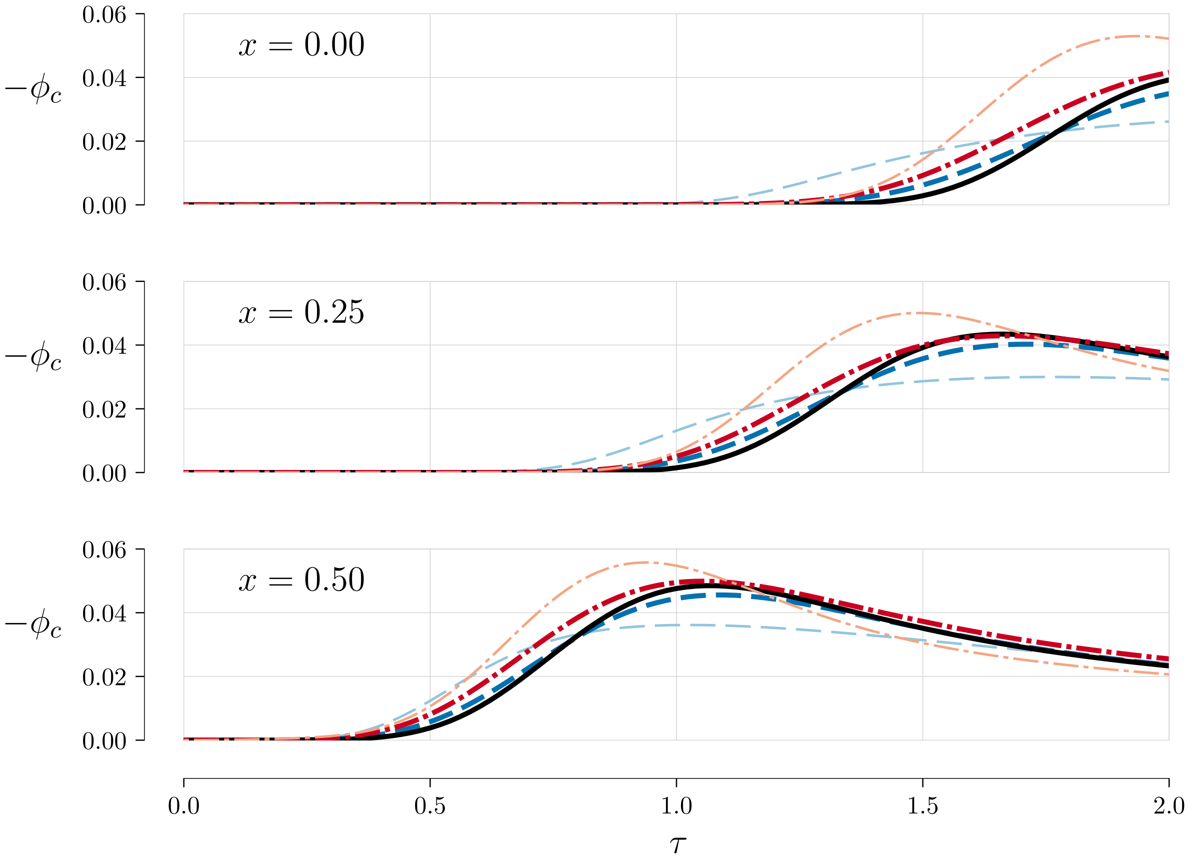

Figure 3.4: The variation with time of the solute flux $\phi_c(\tau)$ at three different sections $x = (0, 0.25, 0.5)$ for $\beta = 0.5$, $\alpha = 3$, and $k = 0.5$. The value of ϕ_c for $S = 1$ (thin dot-dashed curves) and $S = 50$ (thick dot-dashed curves) was evaluated from (3.34), whereas that for $1 \ll S \ll \varepsilon^{-2}$ (thick solid curves) was evaluated from (3.35) and that for $\sigma = \varepsilon^2 S = 1$ (thick dashed curves) and $\sigma = \varepsilon^2 S = 10$ (thin dashed curves) was evaluated from (3.10).

convection driven by the width-averaged Lagrangian velocities, can provide a sufficiently accurate description for many purposes.

3.3.2 Concentric Cylinders

Axisymmetric annular canals constitute a singular configuration of academic interest, although the anticipated relevance to transport in the spinal canal is limited. A distinctive characteristic of axisymmetric geometries is that, because of the lack of azimuthal motion, the width-averaged axial velocity $\int_0^1 u_{\mathrm{L}} \mathrm{d}\eta$ is identically zero, so that solute transport for $S \sim 1$ depends exclusively on Taylor dispersion, as described by

$$\bar{h}\frac{\partial c_0}{\partial t} = \frac{1}{\ell}\left(\ell D_{xx}\frac{\partial c_0}{\partial x}\right). \tag{3.36}$$

To investigate this case in more detail, we consider a concentric annular canal of uniform elastic properties (i.e. $\ell = 1$, $\bar{h} = 1$, and $\gamma = 1$) with an initial solute concentration

$$c_i(x) = \exp[-16^2(x-0.75)^2]. \tag{3.37}$$

A detailed description of the temporal evolution requires integration of the full transport equation (3.1) over multiple cycles in the short time scale t for a sufficiently small value of ε. For the concentric canal, the equation takes the simplified form

$$\frac{\partial c}{\partial t} - \varepsilon\frac{\partial h'}{\partial t}\frac{\eta}{h}\frac{\partial c}{\partial \eta} + \varepsilon u\left(\frac{\partial c}{\partial x} - \frac{\partial h}{\partial x}\frac{\eta}{h}\frac{\partial c}{\partial \eta}\right) + \varepsilon\frac{v}{h}\frac{\partial c}{\partial \eta} = \frac{1}{\alpha^2 S h^2}\frac{\partial^2 c}{\partial \eta^2}. \tag{3.38}$$

The instantaneous velocity and canal deformation were evaluated from the results of chapter 2 from the asymptotic expressions $u \approx u_0 + \varepsilon\langle u_1\rangle$, $v \approx v_0 + \varepsilon\langle v_1\rangle$, $h - 1 = \varepsilon h' \approx \varepsilon h'_0$. In addition to the nonpermeability boundary conditions $\partial c/\partial\eta = 0$ at $\eta = 0, 1$, the integration of (3.38) must specify a boundary condition at $x = 0$. To handle the oscillatory nature of the axial flow at that boundary, the computational domain was artificially extended in the upward direction by an absorbing buffer region between $x = -0.1$ and $x = 0$, in which the values of the transport coefficients in equation (3.38) were set equal to those at $x = 0$. An absorption term $-Bc$ with $B = \max(0, -\{1 - \tanh[20(x + 0.05)]\}u)$ is added the right-hand-side of the transport equation (3.38) to effectively absorb the solute concentration that enters the buffer region during the upward-moving part of the oscillation cycle. The numerical integrations of (3.38) with the additional absorption term were performed using a third order implicit backward difference scheme for time derivatives and a fourth-order centered finite difference discretization for the spatial derivatives.

Results of integrations of (3.38) are to be compared with those of the reduced evolution equation

$$\frac{\partial c_0}{\partial \tau} = \frac{\partial}{\partial x}\left(D_{xx}\frac{\partial c_0}{\partial x}\right) \tag{3.39}$$

which follows from (3.36) when $\bar{h} = \ell = 1$. A boundary value $c_0 = 0$ at $x = 0$ was used in the integrations, with no boundary conditions needed at the canal end $x = 1$, since D_{xx} vanishes there.

Instantaneous concentration maps $c(x, \eta, t)$ obtained from (3.38) for $S = 1$ and $\varepsilon = 0.02$ are shown in figure 3.5(a). In the integrations, the velocity and canal deformation are evaluated with $\alpha = 6$ and $k = 1$. As indicated in the top right corner, the times selected $t - \pi/2 = 2\pi(125, 250, 375, 500, 625)$ incorporate a $\pi/2$ shift, so that the specific snapshots shown in the figure represent intermediate instants between peaks of the fluctuating cycle. The results are used to compute the width-averaged concentration $\int_0^1 c\,\mathrm{d}\eta$, whose axial distribution is shown as a solid curve on the right side of each plot. The results are compared with the profiles of $c_0(x, \tau)$ at corresponding times $\tau = \varepsilon^2 t$ obtained by integrating (3.39), with the value of D_{xx} evaluated for $\alpha = 6$, $k = 1$, and $S = 1$. As can be seen, the accuracy of the predictions provided by the reduced equation (3.39), represented by dashed curves, is excellent in all cases.

The time-averaged variable $c_0(x, \tau)$ does not describe the short-time fluctuations of the concentration that are driven by the oscillatory flow. These can be significant initially when the solute is injected in a small localized region, that being the case considered in (3.37). The extent

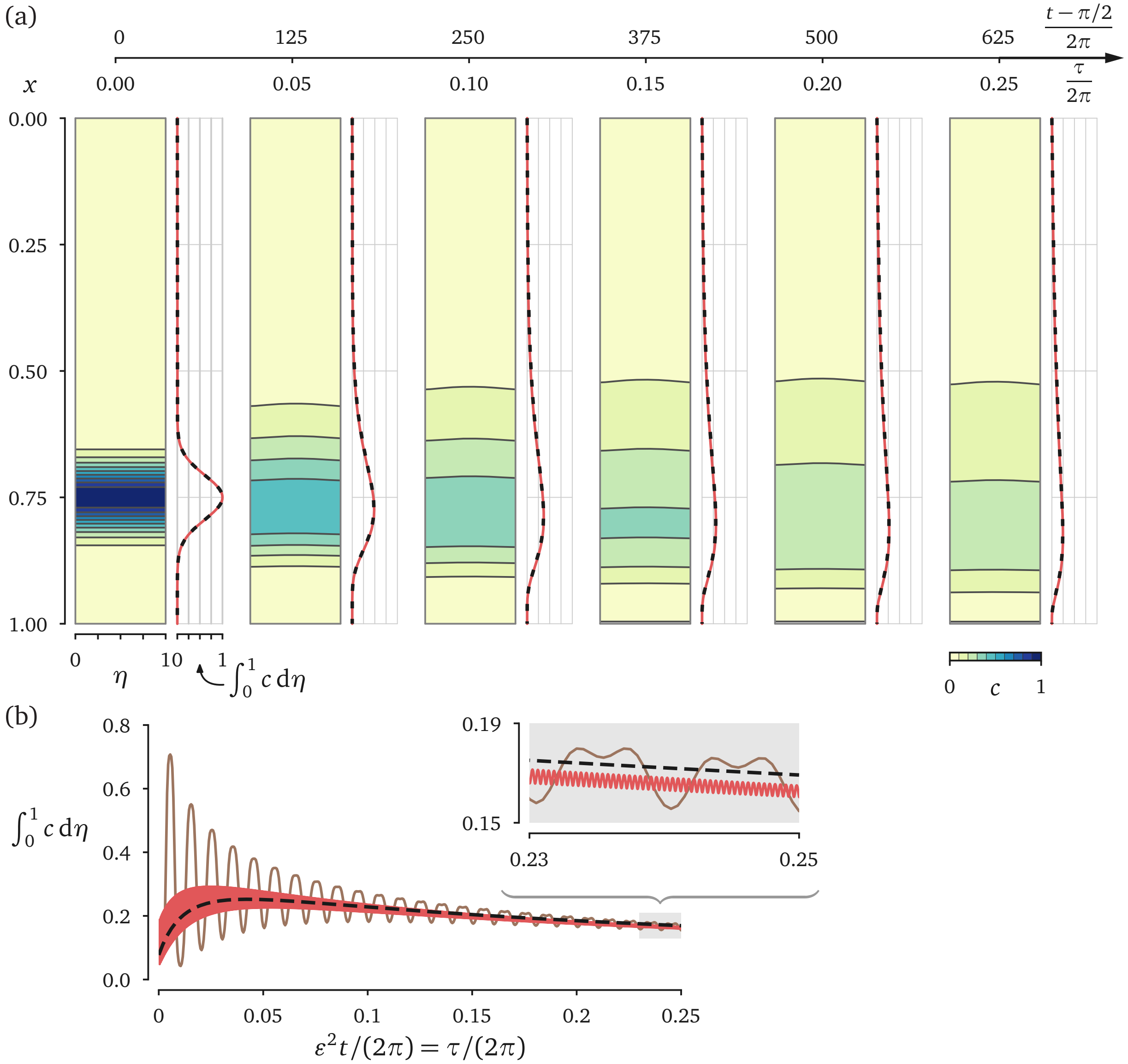

Figure 3.5: (a) The evolution of the solute concentration in a concentric canal ($\beta = 0.0$) obtained for $\alpha = 6$, $k = 1$, and $S = 1$: (a) Instantaneous spatial distributions at six instants of time. Each panel shows on the left the concentration $c(x, \eta, t)$ obtained from integration of (3.38) for $\varepsilon = 0.02$, with the corresponding width-averaged value $\int_0^1 c\,d\eta$ (red solid line) compared on the right with the value of $c_0(x, \tau)$ obtained from the simplified transport equation (3.39) (thick dashed line). (b) Comparison of the temporal evolution of the width-averaged value $\int_0^1 c\,d\eta$ at $x = 0.65$ obtained from (3.38) for $\varepsilon = 0.02$ (pink) and $\varepsilon = 0.1$ (purple) with the value of $c_0(x = 0.65, \tau)$ (black) determined from (3.39).

of the resulting fluctuations, larger for larger values of ε, is illustrated by plotting in figure 3.5(b) the variation of $\int_0^1 c\,\mathrm{d}\eta$ with t at $x = 0.65$. The solution is compared with the corresponding variation of c_0 with $\tau = \varepsilon^2 t$ at that same location, obtained by integrating (3.39). The comparisons indicate that the time-averaged value c_0 describes adequately the evolution of the envelope of the fluctuating solution, with decreasing errors that reduce to values of order $|\int_0^1 c\,\mathrm{d}\eta - c_0| \sim \varepsilon$ for long times, as is consistent with the order of the approximation used here.

The model equation (3.39), describing the long-time evolution of the solute in the distinguished limit $S \sim 1$, involves a concentration $c_0(x,\tau)$ that is uniform across the canal. Correspondingly, convective transport is absent in this limit, because the axial velocity u_L has a zero width-averaged value $\int_0^1 u_\mathrm{L}\mathrm{d}\eta = 0$. The nonuniformities of the concentration across the canal become more pronounced for increasing values of S, thereby promoting convective transport by mean Lagrangian motion. This is clearly seen in the reduced transport equation that arises in the distinguished limit $S \sim \varepsilon^{-2}$,

$$\frac{\partial c_0}{\partial \tau} + u_\mathrm{L}\frac{\partial c_0}{\partial x} + v_\mathrm{L}\frac{\partial c_0}{\partial \eta} = \frac{1}{\alpha^2\varepsilon^2 S}\frac{\partial^2 c_0}{\partial \eta^2}, \tag{3.40}$$

obtained by writing (3.8) for a concentric canal.

The reduced transport equations (3.39) (for $S \sim 1$) and (3.40) (for $S \sim \varepsilon^{-2}$) involve different transport mechanisms, namely, Taylor dispersion for $S \sim 1$ and convection driven by steady streaming and Stokes drift for $S \sim \varepsilon^{-2}$. Since the Taylor diffusivity D_{xx} vanishes for $S \gg 1$ whereas convection becomes ineffective as the concentration becomes uniform across the canal for $S \ll \varepsilon^{-2}$, neither transport mechanism can operate efficiently for values of S in the intermediate range $1 \ll S \ll \varepsilon^{-2}$. This reasoning seems to suggest that in concentric canals the dispersion rate must exhibit a nonmonotonic behavior as the Schmidt number increases from that of gases $S \sim 1$ to that of liquids $S \sim \varepsilon^{-2}$, with a minimum in the dispersion rate reached for an intermediate value of S in the range $1 \ll S \ll \varepsilon^{-2}$.

This paradoxical behavior is illustrated in figure 3.6(a) by representing instantaneous distributions of $c(x,\eta,t)$ obtained after 125 integration cycles (i.e. at $t/(2\pi) = 125$) by integration of (3.38) for $\varepsilon = 0.02$ and different values of S. In agreement with the reduced transport equation (3.39), for Schmidt numbers $S \sim 1$ the plots in figure 3.6(a) reveal that dispersion is seen to proceed as a nearly one-dimensional diffusion process, with the diffusion rate decreasing for increasing values of S as a result of the decreasing Taylor diffusivity D_{xx}. On the other hand, convection is seen to dominate the solute transport in the limit $S \sim \varepsilon^{-2}$, as is apparent for $S = 2500$, where the axial velocity, positive in the central region and negative near the walls, is responsible for the resulting spreading pattern. Neither of these mechanisms is effective at intermediate values of S, where the dispersion rate is seen to be much more limited.

The differences in dispersion rate observed in figure 3.6(a) can be quantified by evaluating $\Delta c = \int_0^1 \int_0^1 (c - c_i)^2 \mathrm{d}\eta \, \mathrm{d}x / \int_0^1 \int_0^1 (c_i)^2 \mathrm{d}\eta \, \mathrm{d}x$ as a global measure of the dispersion. The value of Δc is normalized to be $\Delta c = 0$ at $t = 0$ and $\Delta c = 1$ as the solute abandons the canal for $t \to \infty$. The evolution of $\Delta c(t)$ obtained from the results of integrations of the transport equation (3.38) is shown in figure 3.6(b). As can be seen, since Δc is subject to short-time fluctuations, when represented over many cycles the resulting curves appear as bands that evolve slowly in the long time scale $\varepsilon^2 t$.

The results for increasing S appear to be in agreement with the previous discussion of the two different transport mechanisms. Thus the slope of the resulting bands, measuring the rate of dispersion, is seen to decrease initially as the Schmidt number increases from $S = 1$, a result that can be attributed to the diminished effect of Taylor dispersion. The slope is very small in the intermediate cases $S = 50$ and $S = 250$, but increases substantially for $S = 1000$ and $S = 2500$, as convection driven by the mean Lagrangian motion becomes effective.

The plots clearly support the existence of an intermediate range of values of S where neither Taylor dispersion nor Lagrangian convection are very effective, a distinctive feature of solute transport in perfectly axisymmetric canals. As shown in figures 3.3 and 3.4, corresponding

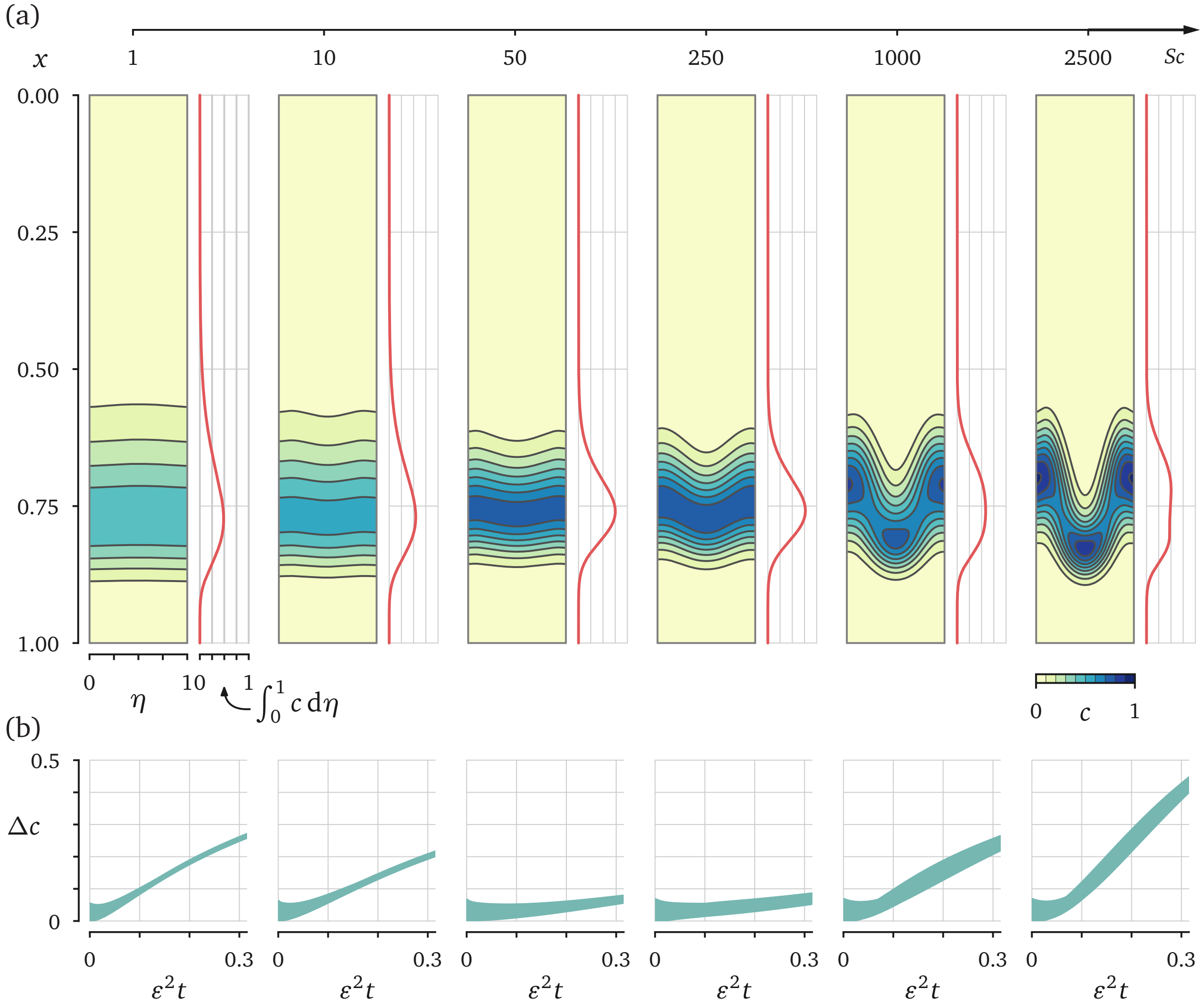

Figure 3.6: Results of integrations of (3.38) for $\varepsilon = 0.02$, $\alpha = 6$, $k = 1$, and different values of S: (a) Concentration fields $c(x, \eta, t)$ at $t/(2\pi) = 125$. (b) Time evolution of $\Delta c = \int_0^1 \int_0^1 (c - c_i)^2 \, d\eta \, dx / \int_0^1 \int_0^1 (c_i)^2 \, d\eta \, dx$.

to a canal defined between two eccentric cylinders, in the presence of asymmetries convection driven by the time-averaged Lagrangian motion remains the dominant transport mechanism regardless of the Schmidt number. An important conclusions of those results is that, with the exception of axisymmetric canals, the simplified equation (3.12) provides a reasonably accurate model for the description of solute transport.

3.4 DNS Validation

In order to validate the simplified model of solute transport described above, full direct numerical simulations of the transport of a solute are calculated. Using the Eulerian velocity field calculated previously in section 2.5, the transport problem

$$\frac{\partial c}{\partial t^*} + \bar{v}^* \cdot \nabla c = \frac{\nu}{S} \nabla^2 c, \tag{3.41}$$

is solved to study the slow-time dispersion of a solute. Again, the asterisks denote dimensional variables. The initial spatial distribution of the solute, defined below in (3.42), is selected to represent the release of a drug in the lumbar region. The simulations are extended over a large number of cycles, corresponding to values of the long-time scale τ of order unity, and their results are compared with those of the simplified transport problem (3.8). Note that in the computations, no simplifications on the basis of the slenderness of the canal or the smallness of the stroke length are introduced.

The numerical solution of (3.41), using the results from the previous solution of (2.64)–(2.65), is carried out with the finite-volume solver Ansys Fluent (Release 16.2), assuring second-order accuracy in time and in space. The same dimensional parameters are used here as are used to solve the flow field. The kinematic viscosity, appearing in (3.41), is taken to be $\nu = 0.698 \times 10^{-6}\,\mathrm{m^2/s}$, the value corresponding to water at 36.8°C. The dimensions of the domain for the two configurations shown in figures 2.3(b) and (c) are $L = 0.6\,\mathrm{m}$, $R_e = 5\,\mathrm{mm}$, and $R_i = 4\,\mathrm{mm}$, corresponding to a canal with characteristic width $h_c = R_e - R_i = 1\,\mathrm{mm}$ and constant inner perimeter $\ell_c = 2\pi R_i \simeq 25\,\mathrm{mm}$. In all computations, the dimensionless eccentricity is taken to be $\beta = 0.5$. The canal deformation, given in (2.66), is evaluated for an angular frequency $\omega = 2\pi s^{-1}$, as corresponds approximately to the cardiac cycle, with the function $H'(x^*/L)$, given in (2.21), computed with $k = 0.5$ and $\alpha = (h_c^2\omega/\nu)^{1/2} = 3$, the latter value consistent with the parametric choice $h_c = 1\,\mathrm{mm}$, $\omega = 2\pi s^{-1}$, and $\nu = 0.698 \times 10^{-6}\,\mathrm{m}^2/\mathrm{s}$. In all computations, the reduced amplitude is taken to be $\varepsilon = 1/20$.

Results are presented for the time-dependent dispersion of a solute for the same two geometrical domains previously presented, with results of integrations of the full transport equation (3.41) compared with those of the simplified equation (3.8) for different values of the Schmidt number S.

3.4.1 Constant Eccentricity

To test the accuracy of the theoretical model in describing transport in the spinal canal, we consider the temporal evolution of a bolus of solute released at the initial instant of time. The initial concentration is given by the truncated Gaussian distribution

$$c\,(x^*/L) = \min\left\{1, \frac{3}{2}\exp\left[-16^2\left(\frac{x^*}{L} - \frac{3}{4}\right)^2\right]\right\}, \tag{3.42}$$

selected as representative of injection of a solute bolus in the upper lumbar region. Predictions obtained by integrating the time-averaged (3.8) in the long time scale $\tau = \varepsilon^2 t = \varepsilon^2\omega t^*$ for $0 \le \tau \le 2$ are compared in figure 3.7 with results of integrations of (3.41) for $0 \le \omega t^* \le 200$. The figure shows distributions of width-averaged concentration for different times, together with the corresponding axial distributions of the averaged concentration at each section x, computed according to $\int_0^1(\bar{h}\int_0^1\langle c\rangle\,\mathrm{d}\eta)\,\mathrm{d}s$ and $\int_0^1(\bar{h}\int_0^1 c_o\,\mathrm{d}\eta)\,\mathrm{d}s$ for the DNS and the model, respectively. Here, $\langle c\rangle = \omega/(2\pi)\int_{t^*}^{t^*+2\pi/\omega} c(\bar{x}^*, t^*)\,\mathrm{d}t^*$ indicates the time-averaged value of the concentration

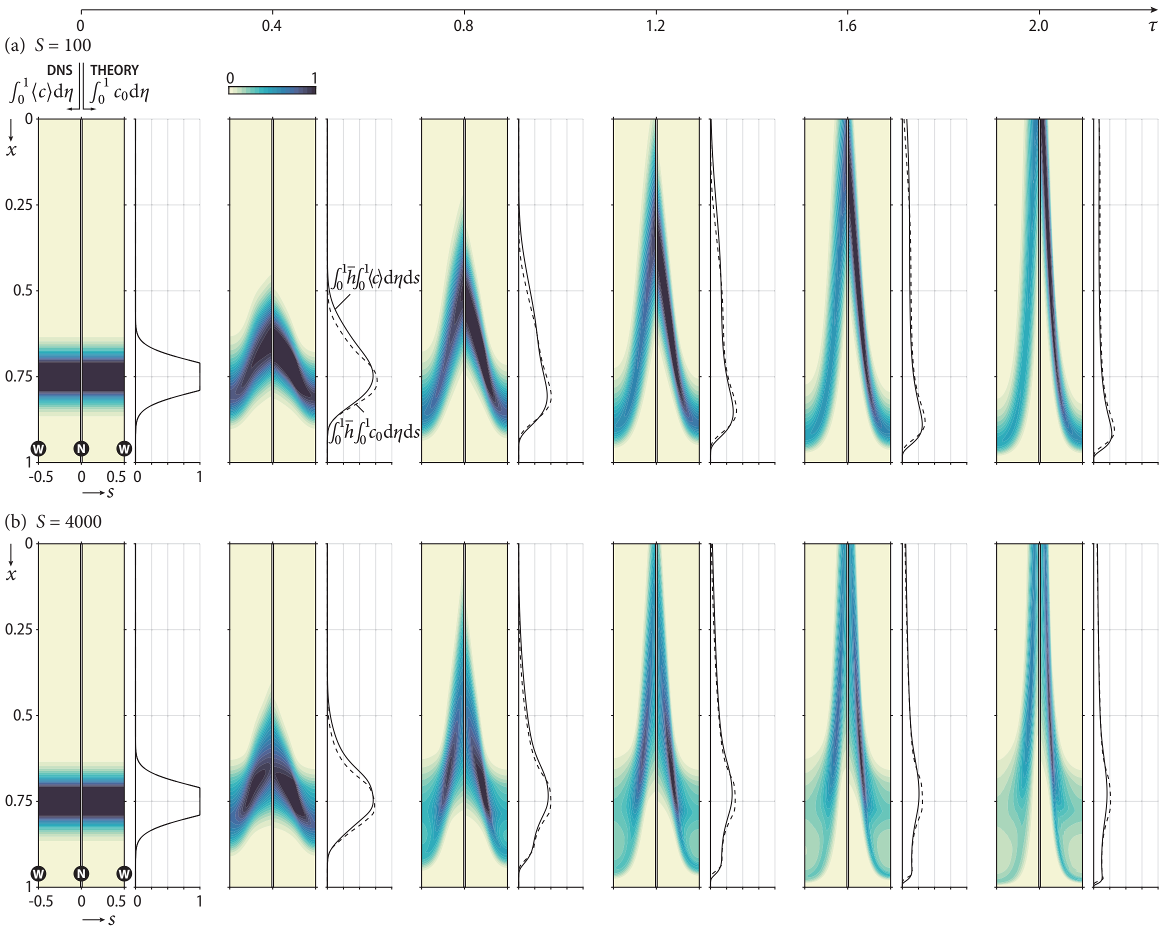

Figure 3.7: Width-averaged distributions of concentration at different instants of time following the release of a bolus of solute with Schmidt number $S = 100$ (a) and $S = 4000$ (b) in the constant-eccentricity canal of figure 2.3(b). Flow conditions correspond to those in figures 2.4 and 2.5. DNS results are represented by the contours on the left-hand side of the panels and by the solid curves representing the axial distribution of solute on the side plots. Theoretical predictions corresponding to integrations of (3.8) are epresented by the contours on the right-hand side of the panels and by the dashed curves on the side plots. The letters N and W near the bottom of the leftmost panels indicate the azimuthal location of the narrowest and widest sections.

over a cardiac cycle. The results correspond to the flow conditions of figures 2.4 and 2.5 for two different values of the Schmidt number, namely $S = 100$ and $S = 4000$.

The agreement between the numerical results and those given by the model is very satisfactory. As expected from the streamline pattern shown in figure 2.7, the solute is convected along the narrow part of the canal ($s = 0$), reaching the canal entrance at $\tau = \varepsilon^2 t \approx 1.2$. This fast upward motion is accompanied by a slower downward motion occurring along the wide part of the canal ($s = 0.5$). The theoretical model is seen to appropriately capture the effects of solute diffusivity, described in the time-averaged (3.8) by the transverse-diffusion term on the right-hand side, leading to solute spatial distributions that are different for $S = 100$ and $S = 4000$, with theoretical predictions in excellent quantitative and qualitative agreement with the DNS results.

3.4.2 Variable Eccentricity

The existence of unconnected closed recirculating regions has a dramatic effect on the solute dispersion along the canal, as verified in accompanying integrations of the transport (3.41) with the initial condition stated in (3.42). These DNS results are shown in figure 3.8, along with predictions obtained with the simplified transport (3.8). According to the streamline pattern shown in figure 2.8, the initial distribution of solute, given in (3.42), is centered at $x^*/L = 0.75$, so that the bolus occupies initially a section of the canal lying between the bottom and central vortices. As a consequence, the upper and lower sides of the bolus are subject to a recirculating flow with opposite sign, eventually resulting in counterflowing convective transport along the line $s = 0.5$, with the solute carried by the central vortex moving upwards and the solute carried by the bottom vortex moving downwards. The subsequent temporal evolution of the solute demonstrates the dominant role of Lagrangian convection, with the solute largely following the streamlines of figure 2.8. In the absence of molecular diffusion, solute particles would remain trapped in the central and bottom recirculating regions. The numerical integrations reveal that diffusive transport provides the needed inter-vortex connectivity, enabling a small portion of solute to reach the entrance of the canal at the end of the numerical integration.

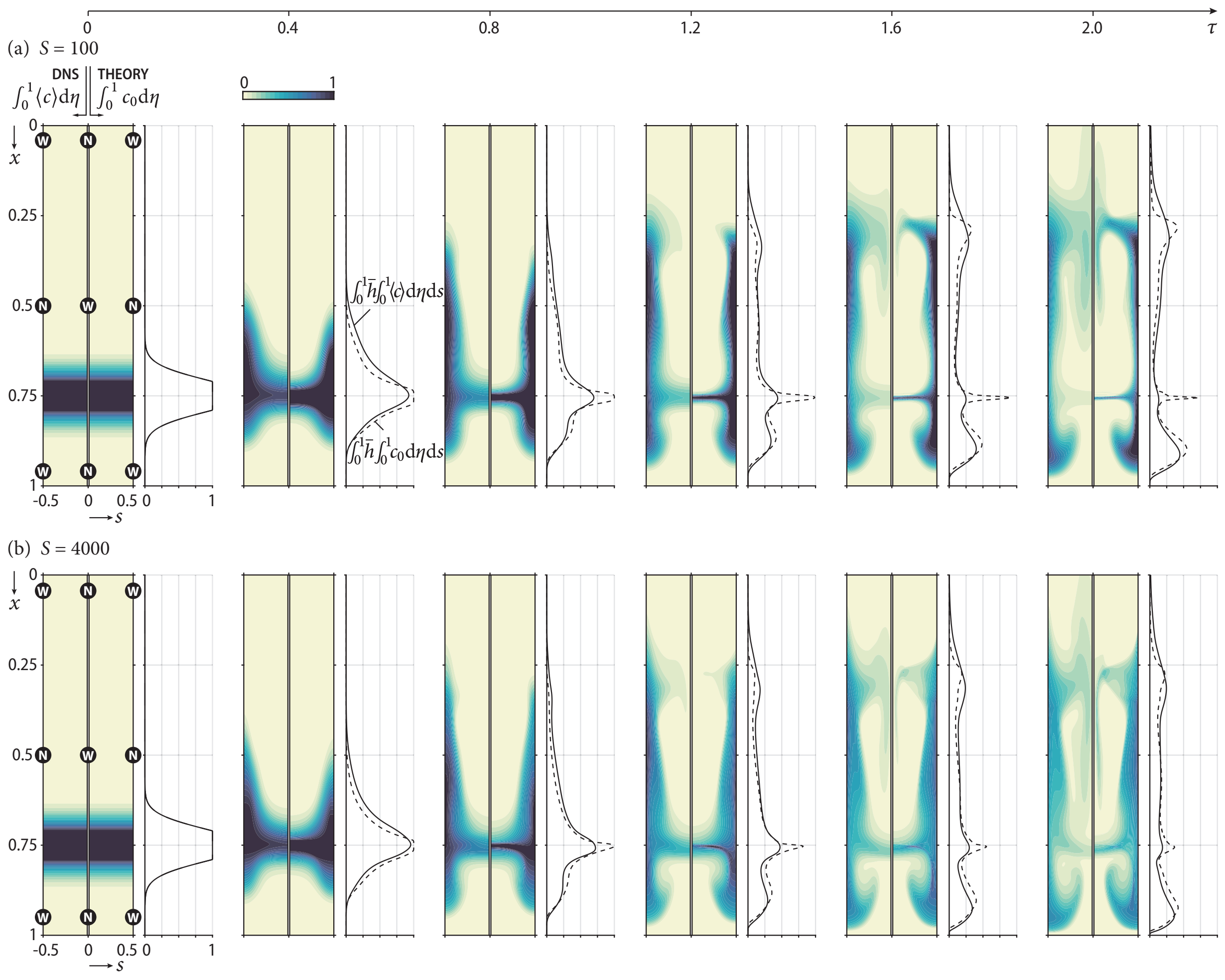

Figure 3.8: Width-averaged distributions of concentration at different instants of time following the release of a bolus of solute with Schmidt number $S = 100$ (a) and $S = 4000$ (b) in the variable-eccentricity canal of figure 2.3(c). The solute is carried by the flow depicted in figure 2.8. DNS results are represented by the contours on the left-hand side of the panels and by the solid curves representing the axial distribution of solute on the side plots. Theoretical predictions corresponding to integrations of (3.8) are represented by the contours on the right-hand side of the panels and by the dashed curves on the side plots. The letters N and W at the leftmost panels indicate the azimuthal location of the narrowest and widest sections.

3.5 Conclusions

A simplified model for the transport of a solute in the spinal canal has been found analytically. The domain is assumed to be doubly slender, following the conditions in (2.1), and the Womersley number α and dimensionless wave number k are assumed to be order unity while the parameter measuring the limited compliance ε, effectively measuring the stroke volume compared to the total volume of fluid in the canal, is assumed to be small. Using this small parameter, all variables are expanded asymptotically. The leading order transport is found to only occur in the long-time scale τ, influenced by the first order corrections to the transport which vary in the short-time scale t.

Results for the simplified transport model are presented for two geometrical configurations, then verified by comparison to full DNS. For the constant eccentricity case, it is clear that convection dominates the transport behavior, with the solute tending cranially on the narrow side of the canal and caudally on the wide side of the canal, matching the streamline patterns found for the Lagrangian velocity. Different diffusion behaviors emerge for the distinguised limits $S \sim 1$ and $S \sim \varepsilon^{-2}$, but convection still dominates in all eccentric cases studied here. For the concentric cylinder case, azimuthal symmetry eliminates the azimuthal velocity and convection is suppressed. The transport is therefore most pronounced at $S \sim 1$ and $S \sim \varepsilon^{-2}$ by the corresponding diffusion behaviors present at those distinguished limits of the Schmidt number.

The simplified model was verified by comparison to full DNS. Good agreement is found in all cases. In verifying the DNS, the case of variable eccentricity is also studied. Since the Lagrangian velocity field yields closed recirculation regions, transport of a solute to the cranial vault ($x = 0$) requires diffusion between the closed vorticies. The simplified transport model for $1 \ll S \ll \varepsilon^{-2}$, containing only the width-averaged convection terms, leads to solute that is trapped in its original vortex with no means of escape. The DNS, which makes no simplifications to the continuity, Navier–Stokes, and transport equations due to the slenderness or the distinguished limit of the Schmidt number, always finds a small amount of diffusion to allow transport of solute between vortices.

This chapter, in part, is a reprint of the material published in the *Journal of Fluid Mechanics*, titled “On the dispersion of a drug delivered intrathecally in the spinal canal,” by J. J. Lawrence, W. Coenen, A. L. Sánchez, G. Pawlak, C. Martínez-Bazán, V. Haughton, and J. C.

Lasheras, (2019) 861, 679-720. The dissertation author was the primary investigator and author of this paper. This chapter, in part, is also a reprint of the material published in *Applied Mathematical Modelling*, titled “Modelling and direct numerical simulation of flow and solute dispersion in the spinal subarachnoid space,” by C. Gutiérrez-Montes, W. Coenen, J. J. Lawrence, C. Martínez-Bazán, A. L. Sánchez, and J. C. Lasheras (2021), 94, 516-533. Cándido Gutiérrez-Montes was the primary author of this paper.

Chapter 4

Effects of Buoyancy on Solute Transport

4.1 Characteristic Scales

The previous chapter considered the transport of a solute assuming that the solute density was exactly equal to the CSF density. The present chapter, however, considers the transport of a solute with a density different from the CSF density. Although the density differences are typically small, the velocities induced by buoyancy are anticipated to be significant since they enter at the same order as the steady streaming and Stokes drift velocities. The transport, dominated by convection caused by these velocities, is expected to see significant changes due to these small density differences.

To anticipate the extent of solute motion induced by buoyancy forces, it is useful to begin by comparing the characteristic value of the buoyancy-induced acceleration $g(\rho-\rho_d)/\rho$ with the characteristic value of the convective acceleration along the canal u_c^2/L, their ratio defining the relevant Richardson number

$$Ri = \frac{g(\rho-\rho_d)/\rho}{\varepsilon^2\omega^2 L}. \tag{4.1}$$

Typical values of this number are evaluated in Table 4.1 for a few common intrathecal drugs with a presumed value of $\varepsilon = 1/30$. The evaluations indicate that values of Ri of order unity

Table 4.1: A few common intrathecal drugs, their densities [48, 60], and associated Richardson numbers $Ri = [g(\rho - \rho_d)]/(\rho \varepsilon^2 \omega^2 L)$, the latter evaluated with $g = 9.81$ m/s^2, $L = 0.6$ m, $\rho = 1.00059$ g/cm^3, and $\varepsilon = 1/30$.

Drug	ρ_d (g/cm^3)	Ri
Droperidol	0.9944	2.30
Normal Saline	0.9995	0.406
Epinephrine	1.0005	0.034
Lidocaine CO_2	1.0010	-0.15
Meperidine	1.0083	-2.872

characterize most situations of practical interest. As previously discussed, the motion of CSF at leading order is given by an unsteady lubrication problem involving the local acceleration and the viscous and pressure forces, with convective acceleration introducing small corrections of order ε, responsible for the steady-streaming motion. The leading-order balance is not altered in the relevant limit $Ri \sim 1$ that applies to intrathecal drugs, in which the associated buoyancy-induced velocities are comparable to the steady-streaming velocities (and therefore a factor ε smaller than the leading-order velocities).

The limit $Ri \sim 1$ will be used in the following analysis to quantify buoyancy effects on drug dispersion. We shall show that, since the buoyancy force depends linearly on the drug concentration, concentration is no longer a passive scalar. Because the coupling with the momentum balance is weak and affects only the higher-order corrections, the slow time dependence of the resulting time-averaged Lagrangian motion includes a buoyancy-induced component that depends on the spatial distribution of drug concentration. The transport equation (3.8) describing the long-time temporal evolution of the drug, which is linear in the absence of buoyancy forces, becomes nonlinear through the dependence of the time-averaged Lagrangian velocities on the solute concentration, thereby complicating the description.

4.2 Updated Eulerian Velocity Field

The problem is formulated in dimensionless form using the scales and notation employed in our previous buoyancy-free analysis shown in chapters 2 and 3. The equations are written in terms of the curvilinear coordinates (x, y, s) indicated in figure 1.1(c), with corresponding streamwise, transverse, and azimuthal velocity components (u, v, w). The geometry of the canal is defined by the dimensionless unperturbed canal width $\bar{h}(x, s)$ and spinal-cord perimeter $\ell(x)$. In the thin-film approximation that applies to the slender spinal canal, the continuity, momentum, and solute conservation equations take the simplified form

$$
\begin{aligned}
\frac{1}{\ell}\frac{\partial}{\partial x}(\ell u)+\frac{\partial v}{\partial y}+\frac{1}{\ell}\frac{\partial w}{\partial s} &= 0, & (4.2)\\
\frac{\partial u}{\partial t}+\varepsilon\left[u\frac{\partial u}{\partial x}+v\frac{\partial u}{\partial y}+\frac{w}{\ell}\frac{\partial u}{\partial s}\right] &= -\frac{\partial p'}{\partial x}+\frac{1}{\alpha^2}\frac{\partial^2 u}{\partial y^2}-\varepsilon Ric, & (4.3)\\
\frac{\partial w}{\partial t}+\varepsilon\left[\frac{u}{\ell}\frac{\partial}{\partial x}(\ell w)+v\frac{\partial w}{\partial y}+\frac{w}{\ell}\frac{\partial w}{\partial s}\right] &= -\frac{1}{\ell}\frac{\partial \hat{p}}{\partial s}+\frac{1}{\alpha^2}\frac{\partial^2 w}{\partial y^2}, & (4.4)\\
\frac{\partial c}{\partial t}+\varepsilon\left(u\frac{\partial c}{\partial x}+v\frac{\partial c}{\partial y}+\frac{w}{\ell}\frac{\partial c}{\partial s}\right) &= \frac{\varepsilon^2}{\alpha^2\sigma}\frac{\partial^2 c}{\partial y^2}, & (4.5)
\end{aligned}
$$

which must be supplemented with the presumed linear elastic equation

$$h' = \gamma(\Pi + k^2 p') \tag{4.6}$$

relating the canal deformation $h' = (h - \bar{h})/\varepsilon$ with the local pressure, the latter given by the sum of the periodic cranial pressure $\Pi(t)$ and the streamwise pressure variation $p'(x, t)$. The order-unity compliance factor $\gamma(x, s)$ is introduced to describe the nonuniform elastic properties of the dura membrane. It is worth noting that, although results are given below only for a simple harmonic intracranial pressure $\Pi = \cos(t)$, the analysis could be easily extended to general periodic functions $\Pi(t)$ with use of Fourier decomposition, as shown in section 6.1.

The problem is formulated using the Boussinesq approximation, as is appropriate for

$|\rho - \rho_d| \ll \rho$. The case considered here is that of a sitting or standing patient, such that the streamwise coordinate x is effectively aligned with gravity, neglecting the spinal curvature. The component of the buoyancy force acting in the azimuthal direction is therefore small, and has been correspondingly neglected in writing (4.4). With the definition (4.1), the Richardson number measuring the buoyancy force in (4.3) is positive when the drug is lighter than the CSF, for which buoyancy drives the drug upwards toward the brain (in the negative x direction), as is common for drugs diluted in water. Conversely, for $\rho_d > \rho$ the corresponding Richardson number is negative, such as the case when dextrose is added to the drug solution, for which the buoyancy force points in the positive x direction, toward the sacral region and away from the brain.

The pressure drop is negligible at the entrance of the canal, resulting in the condition $p' = 0$ at $x = 0$. The velocity satisfies the non-slip condition $u = v = w = 0$ at $y = 0$ and $u = v - \partial h'/\partial t = w = 0$ at $y = h$, while the concentration satisfies $\partial c/\partial \eta = 0$ at $y = 0, h$, as corresponds to the case of non-permeable bounding surfaces considered here. Since the canal is symmetric, the azimuthal velocity component w vanishes at $s = 0$ and $s = 1/2$. The requirement that the axial volume flux $\int_0^1 \left(\int_0^h u \mathrm{d}y \right) \mathrm{d}s$ must vanish at the closed end $x = 1$ completes the set of boundary conditions needed to determine the flow in the canal.

Besides the Richardson number Ri and the compliance parameter $\varepsilon \ll 1$, the set of governing parameters includes the Womersley number $\alpha = h_c/(\nu/\omega)^{1/2}$, the dimensionless elastic wavenumber k, and the rescaled Schmidt number $\sigma = S\varepsilon^2$. The problem is to be solved in the limit $\varepsilon \ll 1$ with $\alpha \sim 1$ and $k \sim 1$, as is appropriate for describing CSF flow in the spinal canal, for solutes with $\sigma = S\varepsilon^2 \sim 1$ and $Ri \sim 1$, the distinguished limit of interest in intrathecal drug dispersion.

In the development, it is convenient to replace the transverse coordinate y by its normalized counterpart $\eta = y/h$, with $0 \leq \eta \leq 1$. Effects of buoyancy can be described by introducing the long time scale $\tau = \varepsilon^2 t$, in addition to the short time scale t. In this two-time scale formalism, all variables are assumed to be 2π periodic in the short time scale t, slow changes in time being described by the additional time variable τ, which is formally introduced in the equations by replacing the original time derivatives by $\partial/\partial t + \varepsilon^2 \partial/\partial\tau$. Following our previous work [75] and chapters 2 and 3, the asymptotic solution for $\varepsilon \ll 1$ is constructed by substituting expansions for all flow variables in powers of ε (e.g. $u = u_0 + \varepsilon u_1 + \cdots$) into the above equations (4.2)–(4.6) and sequentially solving the problems that arise when collecting terms at different orders in powers of ε.

4.2.1 Leading-order Solution

At leading order, (4.2)–(4.5) simplify to

$$\begin{aligned}
\frac{1}{\ell}\frac{\partial}{\partial x}(\ell u_0) &- \frac{\eta}{\bar{h}}\frac{\partial \bar{h}}{\partial x}\frac{\partial u_0}{\partial \eta} + \frac{1}{\bar{h}}\frac{\partial v_0}{\partial \eta} + \frac{1}{\ell}\frac{\partial w_0}{\partial s} - \frac{\eta}{\bar{h}}\frac{1}{\ell}\frac{\partial \bar{h}}{\partial s}\frac{\partial w_0}{\partial \eta} = 0, && (4.7)\\
\frac{\partial u_0}{\partial t} &= -\frac{\partial p_0'}{\partial x} + \frac{1}{\alpha^2 \bar{h}^2}\frac{\partial^2 u_0}{\partial \eta^2}, && (4.8)\\
\frac{\partial w_0}{\partial t} &= -\frac{1}{\ell}\frac{\partial \hat{p}_0}{\partial s} + \frac{1}{\alpha^2 \bar{h}^2}\frac{\partial^2 w_0}{\partial \eta^2}, && (4.9)\\
\frac{\partial c_0}{\partial t} &= 0. && (4.10)
\end{aligned}$$

The last equation indicates that the solute concentration varies at leading order in the long time scale τ, while variations with the short time scale t affect only higher order corrections of relative order ε and smaller. As shown previously, the solution to the periodic lubrication problem (4.7)–(4.9) supplemented with $h_0' = \gamma(\cos t + k^2 p_0')$, the leading-order form of (4.6) when $\Pi = \cos t$, can be written as

$$\begin{aligned}
u_0 &= \mathrm{Re}\left(\mathrm{i}e^{\mathrm{i}t}U\right), v_0 = \mathrm{Re}\left(\mathrm{i}e^{\mathrm{i}t}V\right), w_0 = \mathrm{Re}\left(\mathrm{i}e^{\mathrm{i}t}W\right),\\
p_0' &= \mathrm{Re}\left(e^{\mathrm{i}t}P'\right), \hat{p}_0 = \mathrm{Re}\left(e^{\mathrm{i}t}\hat{P}\right), h_0' = \mathrm{Re}\left(e^{\mathrm{i}t}H'\right), && (4.11)
\end{aligned}$$

where the complex functions $U(x,\eta,s)$, $V(x,\eta,s)$, $W(x,\eta,s)$, $P'(x)$, $\hat{P}(x,s)$, and $H'(x,s)$ are given in section 2.2.1. At leading order, the solution for the velocity is buoyancy-free and independent of the long-time scale τ.

4.2.2 Buoyancy-induced Streaming

While the above harmonic functions (4.11) have zero mean values over an oscillation period, i.e. $\langle u_0 \rangle = 0$ with $\langle \cdot \rangle = \int_0^{2\pi} \cdot \mathrm{d}t/(2\pi)$, the velocity corrections (u_1, v_1, w_1) contain nonzero time-averaged components $(\langle u_1 \rangle, \langle v_1 \rangle, \langle w_1 \rangle)$ that satisfy the quasi-steady conservation equations

$$\begin{aligned}
\mathcal{F} &= \frac{1}{\ell}\frac{\partial}{\partial x}(\ell \bar{h} \langle u_1 \rangle) - \frac{\partial}{\partial \eta}\left(\eta \frac{\partial \bar{h}}{\partial x}\langle u_1 \rangle\right) \\
&+ \frac{\partial \langle v_1 \rangle}{\partial \eta} + \frac{1}{\ell}\frac{\partial}{\partial s}(\bar{h}\langle w_1 \rangle) - \frac{\partial}{\partial \eta}\left(\frac{\eta}{\ell}\frac{\partial \bar{h}}{\partial s}\langle w_1 \rangle\right), \qquad (4.12)\\
\mathcal{F}_x &= -\frac{\partial \langle p_1' \rangle}{\partial x} + \frac{1}{\bar{h}^2\alpha^2}\frac{\partial^2 \langle u_1 \rangle}{\partial \eta^2} - Ri\, c_0, \qquad (4.13)\\
\mathcal{F}_s &= -\frac{1}{\ell}\frac{\partial \langle \hat{p}_1 \rangle}{\partial s} + \frac{1}{\bar{h}^2\alpha^2}\frac{\partial^2 \langle w_1 \rangle}{\partial \eta^2}, \qquad (4.14)
\end{aligned}$$

obtained by taking the time average of the equations that emerge when collecting terms of order ε in (4.2)–(4.4). The left-hand-side functions

$$\mathcal{F} = -\frac{1}{\ell}\frac{\partial}{\partial x}(\ell \langle h_0' u_0 \rangle) + \frac{\partial}{\partial \eta}\left(\eta \langle u_0 \frac{\partial h_0'}{\partial x} \rangle\right) - \frac{1}{\ell}\frac{\partial}{\partial s}(\langle h_0' w_0 \rangle) + \frac{\partial}{\partial \eta}\left(\frac{\eta}{\ell}\langle w_0 \frac{\partial h_0'}{\partial s} \rangle\right), \qquad (4.15)$$

$$\begin{aligned}
\mathcal{F}_x &= \frac{1}{\ell}\frac{\partial}{\partial x}(\ell \langle u_0^2 \rangle) + \frac{1}{\bar{h}}\frac{\partial}{\partial \eta}\langle u_0 v_0 \rangle + \frac{1}{\ell}\frac{\partial}{\partial s}\langle u_0 w_0 \rangle \\
&- \frac{\eta}{\bar{h}}\frac{\partial}{\partial \eta}\langle \frac{\partial h_0'}{\partial t} u_0 \rangle - \frac{\partial \bar{h}}{\partial x}\frac{\eta}{\bar{h}}\frac{\partial}{\partial \eta}\langle u_0^2 \rangle - \frac{1}{\ell}\frac{\partial \bar{h}}{\partial s}\frac{\eta}{\bar{h}}\frac{\partial}{\partial \eta}\langle u_0 w_0 \rangle + \frac{2}{\bar{h}^3\alpha^2}\frac{\partial^2}{\partial \eta^2}\langle h_0' u_0 \rangle, \qquad (4.16)
\end{aligned}$$

and

$$
\begin{aligned}
\mathcal{F}_s \quad = \quad & \frac{\partial}{\partial x}\langle u_0 w_0\rangle + 2\frac{\langle u_0 w_0\rangle}{\ell}\frac{\partial \ell}{\partial x} + \frac{1}{\bar{h}}\frac{\partial}{\partial \eta}\langle v_0 w_0\rangle + \frac{1}{\ell}\frac{\partial}{\partial s}\langle w_0^2\rangle - \frac{\eta}{\bar{h}}\frac{\partial}{\partial \eta}\langle\frac{\partial h_0'}{\partial t}w_0\rangle \\
- \quad & \frac{\partial \bar{h}}{\partial x}\frac{\eta}{\bar{h}}\frac{\partial}{\partial \eta}\langle u_0 w_0\rangle - \frac{1}{\ell}\frac{\partial \bar{h}}{\partial s}\frac{\eta}{\bar{h}}\frac{\partial}{\partial \eta}\langle w_0^2\rangle + \frac{2}{\bar{h}^3\alpha^2}\frac{\partial^2}{\partial \eta^2}\langle h_0' w_0\rangle, \qquad (4.17)
\end{aligned}
$$

carrying the nonlinear corrections arising from the convective acceleration and the deformation of the canal, involve nonzero time averages of products of the harmonic functions (4.11). Because of the presence of the buoyancy force in (4.13), proportional to the solute concentration $c_0(x,\eta,s,\tau)$, the time-averaged velocity corrections $(\langle u_1\rangle,\langle v_1\rangle,\langle w_1\rangle)$ can be expected to evolve in the long-time scale τ.

The velocity must satisfy zero volume flux at the closed end of the canal, given by $\int_0^1\left(\bar{h}\int_0^1\langle u_1\rangle \mathrm{d}\eta\right)\mathrm{d}s = 0$ at $x=1$ and the symmetry condition $\int_0^1\langle w_1\rangle \mathrm{d}\eta = 0$ at $s=(0,1)$. The non-slip condition for the velocity on the bounding surfaces requires that $\langle u_1\rangle = \langle v_1\rangle = \langle w_1\rangle = 0$ at $\eta=(0,1)$, with the condition $\langle v_1\rangle = 0$ at $\eta = 1$ following at this order from the general condition $v = \partial h'/\partial t$ written in the two-time-scale formalism in the form $v = \partial h'/\partial t + \varepsilon^2\partial h'/\partial\tau$, so that $\langle v\rangle = \varepsilon^2\partial\langle h'\rangle/\partial\tau$.

In solving the above linear problem it is convenient to use superposition by writing the velocity in the form $(\langle u_1\rangle,\langle v_1\rangle,\langle w_1\rangle) = (u_{\mathrm{SS}}+u_{\mathrm{B}}, v_{\mathrm{SS}}+v_{\mathrm{B}}, w_{\mathrm{SS}}+w_{\mathrm{B}})$. The subscript SS denotes the time-independent steady streaming velocities resulting from the terms on the left-hand side of (4.12)–(4.14), while the subscript B denotes the velocity corrections induced by buoyancy, linearly proportional to the unknown solute concentration $c_0(x,\eta,s,\tau)$, which introduces in (4.13) a quasi-steady dependence on the long-time scale τ. The steady-streaming components $(u_{\mathrm{SS}}, v_{\mathrm{SS}}, w_{\mathrm{SS}})$, independent of τ, are determined by integration of the problem found for $Ri=0$. The solution, obtained previously, is given in section 2.2.2.

The slowly evolving buoyancy-induced flow is determined by integration of

$$
\begin{aligned}
0 &= \frac{1}{\ell}\frac{\partial}{\partial x}(\ell\bar{h}u_{\mathrm{B}})-\frac{\partial}{\partial\eta}\left(\eta\frac{\partial\bar{h}}{\partial x}u_{\mathrm{B}}\right)+\frac{\partial v_{\mathrm{B}}}{\partial\eta}+\frac{1}{\ell}\frac{\partial}{\partial s}(\bar{h}w_{\mathrm{B}})-\frac{\partial}{\partial\eta}\left(\frac{\eta}{\ell}\frac{\partial\bar{h}}{\partial s}w_{\mathrm{B}}\right), \qquad (4.18)\\
0 &= -\frac{\partial p'_{\mathrm{B}}}{\partial x}+\frac{1}{\bar{h}^2\alpha^2}\frac{\partial^2 u_{\mathrm{B}}}{\partial\eta^2}-Ric_0, \qquad (4.19)\\
0 &= -\frac{1}{\ell}\frac{\partial\hat{p}_{\mathrm{B}}}{\partial s}+\frac{1}{\bar{h}^2\alpha^2}\frac{\partial^2 w_{\mathrm{B}}}{\partial\eta^2}, \qquad (4.20)
\end{aligned}
$$

subject to the conditions $u_{\mathrm{B}} = v_{\mathrm{B}} = w_{\mathrm{B}} = 0$ at $\eta = (0,1)$, $\int_0^1 \left(\bar{h}\int_0^1 u_{\mathrm{B}}\mathrm{d}\eta\right)\mathrm{d}s = 0$ at $x = 1$, and $\int_0^1 w_{\mathrm{B}}\mathrm{d}\eta = 0$ at $s = (0,1)$. The solution can be written in terms of the solute concentration c_0 in the form

$$
\begin{aligned}
\frac{u_{\mathrm{B}}}{\alpha^2 Ri\bar{h}^2} &= \eta\int_0^{\eta}c_0\mathrm{d}\tilde{\eta}-\int_0^{\eta}c_0\tilde{\eta}\mathrm{d}\tilde{\eta}-\eta\int_0^1 c_0(1-\eta)\mathrm{d}\eta+3\eta(1-\eta)\frac{\int_0^1\bar{h}^3C_0\mathrm{d}s}{\int_0^1\bar{h}^3\mathrm{d}s}, \qquad (4.21)\\
\frac{w_{\mathrm{B}}}{\alpha^2 Ri\bar{h}^2} &= \frac{3\eta(1-\eta)}{\bar{h}^3}\frac{\partial}{\partial x}\left[\ell\int_0^s\bar{h}^3C_0\mathrm{d}\tilde{s}-\ell\int_0^s\bar{h}^3\mathrm{d}\tilde{s}\left(\frac{\int_0^1\bar{h}^3C_0\mathrm{d}s}{\int_0^1\bar{h}^3\mathrm{d}s}\right)\right], \qquad (4.22)\\
v_{\mathrm{B}} &= -\frac{1}{\ell}\frac{\partial}{\partial x}\left(\ell\bar{h}\int_0^{\eta}u_{\mathrm{B}}\mathrm{d}\tilde{\eta}\right)+\eta\frac{\partial\bar{h}}{\partial x}u_{\mathrm{B}}-\frac{1}{\ell}\frac{\partial}{\partial s}\left(\bar{h}\int_0^{\eta}w_{\mathrm{B}}\mathrm{d}\tilde{\eta}\right)+\frac{\eta}{\ell}\frac{\partial\bar{h}}{\partial s}w_{\mathrm{B}}, \qquad (4.23)
\end{aligned}
$$

where

$$
C_0(x,s,\tau) = \int_0^1 c_0\eta(1-\eta)\mathrm{d}\eta. \qquad (4.24)
$$

Tildes are used throughout the text to denote dummy integration variables.

4.3 Transport description

4.3.1 Solute Transport for $\sigma = \varepsilon^2 S \sim 1$

As shown in section 3.2, the transport equation for $c_0(x,\eta,s,\tau)$ is obtained by extending the analysis of (4.5) to higher order. Integration of the equation that arises at $O(\varepsilon)$ provides

$$\begin{aligned} c_1 &= -\int u_0 \mathrm{d}t \frac{\partial c_0}{\partial x} - \int w_0 \mathrm{d}t \frac{1}{\ell}\frac{\partial c_0}{\partial s} - \int v_0 \mathrm{d}t \frac{1}{\bar{h}}\frac{\partial c_0}{\partial \eta} \\ &+ \left(h_0' + \int u_0 \mathrm{d}t \frac{\partial \bar{h}}{\partial x} + \int w_0 \mathrm{d}t \frac{1}{\ell}\frac{\partial \bar{h}}{\partial s} \right) \frac{\eta}{\bar{h}}\frac{\partial c_0}{\partial \eta} + \langle c_1 \rangle \end{aligned} \tag{4.25}$$

including the time-averaged value $\langle c_1 \rangle$ and the harmonic functions h_0', $\int u_0 \mathrm{d}t = \mathrm{Re}\left(\mathrm{e}^{\mathrm{i}t} U\right)$, $\int v_0 \mathrm{d}t = \mathrm{Re}\left(\mathrm{e}^{\mathrm{i}t} V\right)$, and $\int w_0 \mathrm{d}t = \mathrm{Re}\left(\mathrm{e}^{\mathrm{i}t} W\right)$. Collecting terms of order ε^2 in (4.5) and taking the time average provides the reduced transport equation

$$\frac{\partial c_0}{\partial \tau} + u_{\mathrm{L}} \left(\frac{\partial c_0}{\partial x} - \frac{\partial \bar{h}}{\partial x}\frac{\eta}{\bar{h}}\frac{\partial c_0}{\partial \eta} \right) + \frac{v_{\mathrm{L}}}{\bar{h}}\frac{\partial c_0}{\partial \eta} + \frac{w_{\mathrm{L}}}{\ell} \left(\frac{\partial c_0}{\partial s} - \frac{\partial \bar{h}}{\partial s}\frac{\eta}{\bar{h}}\frac{\partial c_0}{\partial \eta} \right) = \frac{1}{\alpha^2 \sigma \bar{h}^2}\frac{\partial^2 c_0}{\partial \eta^2}. \tag{4.26}$$

The time-averaged Lagrangian velocity driving convective transport in the long time scale

$$\begin{cases} u_{\mathrm{L}} = u_{\mathrm{SS}} + u_{\mathrm{B}} + u_{\mathrm{SD}} \\ v_{\mathrm{L}} = v_{\mathrm{SS}} + v_{\mathrm{B}} + v_{\mathrm{SD}} \\ w_{\mathrm{L}} = w_{\mathrm{SS}} + w_{\mathrm{B}} + w_{\mathrm{SD}} \end{cases} \tag{4.27}$$

is found to be the sum of the time-averaged Eulerian velocity $(\langle u_1 \rangle, \langle v_1 \rangle, \langle w_1 \rangle) = (u_{\mathrm{SS}} + u_{\mathrm{B}}, v_{\mathrm{SS}} + v_{\mathrm{B}}, w_{\mathrm{SS}} + w_{\mathrm{B}})$, described above, and the Stokes-drift velocity $(u_{\mathrm{SD}}, v_{\mathrm{SD}}, w_{\mathrm{SD}})$, a purely kinematic effect associated with the spatial non-uniformity of the leading-order flow. Explicit expressions are given in section 2.3 for $(u_{\mathrm{SD}}, v_{\mathrm{SD}}, w_{\mathrm{SD}})$, thereby completing the description of the velocity field.

The transport equation (4.26), supplemented with (4.21)–(4.23) for the evaluation of the changing buoyancy-induced velocity $(u_{\mathrm{B}}, v_{\mathrm{B}}, w_{\mathrm{B}})$ and with the expressions given in sections 2.2.2

and 2.3 for the time-independent velocity components $(u_{\mathrm{SS}}, v_{\mathrm{SS}}, w_{\mathrm{SS}})$ and $(u_{\mathrm{SD}}, v_{\mathrm{SD}}, w_{\mathrm{SD}})$, can be integrated with boundary conditions $\partial c_0/\partial\eta = 0$ at $\eta = (0,1)$ to determine the temporal evolution of the solute from a prescribed initial distribution.

4.3.2 Solute Transport for $1 \ll S \ll \varepsilon^{-2}$

The solution simplifies for solutes with $\sigma = \varepsilon^2 S \ll 1$, when c_0 is uniform across the width of the canal, so that (4.26) reduces to

$$\frac{\partial c_0}{\partial \tau} + \left(\int_0^1 u_{\mathrm{L}} \mathrm{d}\eta\right) \frac{\partial c_0}{\partial x} + \left(\int_0^1 w_{\mathrm{L}} \mathrm{d}\eta\right) \frac{1}{\ell} \frac{\partial c_0}{\partial s} = 0. \tag{4.28}$$

The width-averaged values of the buoyancy-induced velocities driving the convective in this limit can be evaluated from

$$\int_0^1 u_{\mathrm{B}} \mathrm{d}\eta = \frac{\bar{h}^2 \alpha^2 Ri}{12 \int_0^1 \bar{h}^3 \mathrm{d}s} \left(\int_0^1 \bar{h}^3 c_0 \, \mathrm{d}s - c_0 \int_0^1 \bar{h}^3 \mathrm{d}s\right) \tag{4.29}$$

and

$$\int_0^1 w_{\mathrm{B}} \mathrm{d}\eta = \frac{\alpha^2 Ri}{12 \bar{h}} \frac{\partial}{\partial x} \left[\frac{\ell}{\int_0^1 \bar{h}^3 \mathrm{d}s} \left(\int_0^1 \bar{h}^3 \mathrm{d}s \int_0^s \bar{h}^3 c_0 \mathrm{d}\tilde{s} - \int_0^1 \bar{h}^3 c_0 \, \mathrm{d}s \int_0^s \bar{h}^3 \mathrm{d}\tilde{s} \right) \right], \tag{4.30}$$

as follows from (4.21) and (4.22) with $C_0 = c_0/6$. For an initial mass-fraction distribution $c = c_i(x,s)$, integration of (4.28) supplemented with (4.29) and (4.30) determines the dispersion of the solute.

4.4 Preliminary Results for a Simplified Geometry

4.4.1 Results for $1 \ll S \ll \varepsilon^{-2}$

The formulation above explicitly defines the dispersion of a drug with density different from that of the CSF given the functions $\bar{h}(x,s)$, $\ell(x)$, $\gamma(x,s)$, the parameters β, α, k, and Ri, and the initial distribution of solute c_i. Here we consider the variable eccentricity case, shown in figure 2.3, where the canal width varies according to $\bar{h} = 1 - \beta \cos(2\pi s)\cos(2\pi x)$. This case is chosen to better illustrate the affects of buoyancy when the width-averaged steady streaming and Stokes drift velocities, previously the only components of the Lagrangian velocities, $\int_0^1 u_L \mathrm{d}\eta$ and $\int_0^1 w_L \mathrm{d}\eta$ predict closed recirculation regions (see figure 2.8).

The time-averaged transport equation for a buoyant solute takes different forms depending on the Schmidt number. For $S \sim \varepsilon^{-2} \gg 1$, the solute concentration at leading order $c_0(x,\eta,s,\tau)$ is obtained from the reduced transport equation (4.26), involving transverse diffusion across the canal and convective transport, the latter driven by the previously found time-averaged Lagrangian velocity (previously called (u_L, v_L, w_L)), which is constant in τ, and the buoyancy-induced steady streaming velocity velocity (u_B, v_B, w_B), which is not constant in τ. For $1 \ll S \ll \varepsilon^{-2}$, the solute concentration $c_0(x,s,\tau)$ is found to be uniform across the width of the canal as a result of the dominant effect of transverse diffusion. The transport equation in this case (4.28) involves convective transport of the previously found width-averaged axial and azimuthal components of the Lagrangian velocity, constant in τ, and the width-averaged axial and azimuthal components of the buoyancy-induced streaming velocity, not constant in τ.

The relevant transport coefficients for (4.26) are u_L, v_L, and w_L, calculated from (2.57)–(2.58), and u_B, v_B, and w_B, calculated from (4.21)–(4.23). For (4.28), the transport coefficients are instead given by the width-averaged values $\int_0^1 u_L \mathrm{d}\eta$ and $\int_0^1 w_L \mathrm{d}\eta$, calculated from (2.62)–(2.63), and $\int_0^1 u_B \mathrm{d}\eta$ and $\int_0^1 w_B \mathrm{d}\eta$, calculated from (4.29)–(4.30). The results depend on the Richardson number, defined in (4.1), which measures the relative importance of buoyancy compared to convection, where a positive Richardson number indicates a light or hypobaric solute and a negative Richardson number indicates a heavy or hyperbaric solute. Additional parameters include the Womersley number α defined in (2.8), which measures the relative importance of inertial forces as compared to viscous forces, and the dimensionless wave number defined in (2.4), which enters in the elastic equation (4.6) relating the pressure with the canal deformation, both order-unity parameters. The Schmidt number $S = \nu/\kappa$, comparing the momentum diffusivity of CSF with the molecular diffusivity of the solute, enters in (4.26), the transport equation for $S \sim \varepsilon^{-2}$, but is absent in (4.28), the transport equation for $1 \ll S \ll \varepsilon^{-2}$. The geometry of the canal is defined by the inner perimeter $\ell(x)$, the unperturbed canal width $\bar{h}(x,s)$, and the dura-membrane compliance $\gamma(x,s)$, all order-unity functions.

The results given in figure 4.1 correspond to an eccentricity parameter $\beta = 0.5$, a Womersley number $\alpha = 3$, and a nondimensional wave number $k = 0.5$. The coupling of the axial momentum and transport equations causes the buoyancy-induced streaming velocities to vary with c_0, and therefore vary with time. Substitution of (4.21)–(4.23) into (4.26) for $S \sim \varepsilon^{-2} \gg 1$ and (4.29)–(4.30) into (4.28) for $1 \ll S \ll \varepsilon^{-2}$ in both cases leads to a nonlinear ordinary differential equation, different from the previous linear ordinary differential equation. The numerical computations utilize a second-order central finite-difference approximation for the spatial derivatives and a third-order backward differentiation formula for the time-advancement. This method is chosen over the previously used Runge-Kutta 4/5 method due to its improved stability. The initial condition, given by (4.32), is a truncated Gaussian expression representing a bolus injection into the lumbar region of the SSAS. The resulting distributions of the width-averaged concentration $\int_0^1 c_0 \mathrm{d}\eta$ as a function of x and s at different instants of time are presented for different values of the Richardson number, where solution of (4.28) is shown in figure 4.1 and solution of (4.26) is to be completed in future work.

The non-buoyant case ($Ri = 0$), shown in figure 4.1(b), is computed in addition to the cases of a light solute and a heavy solute in order to provide comparison. Because this limit of

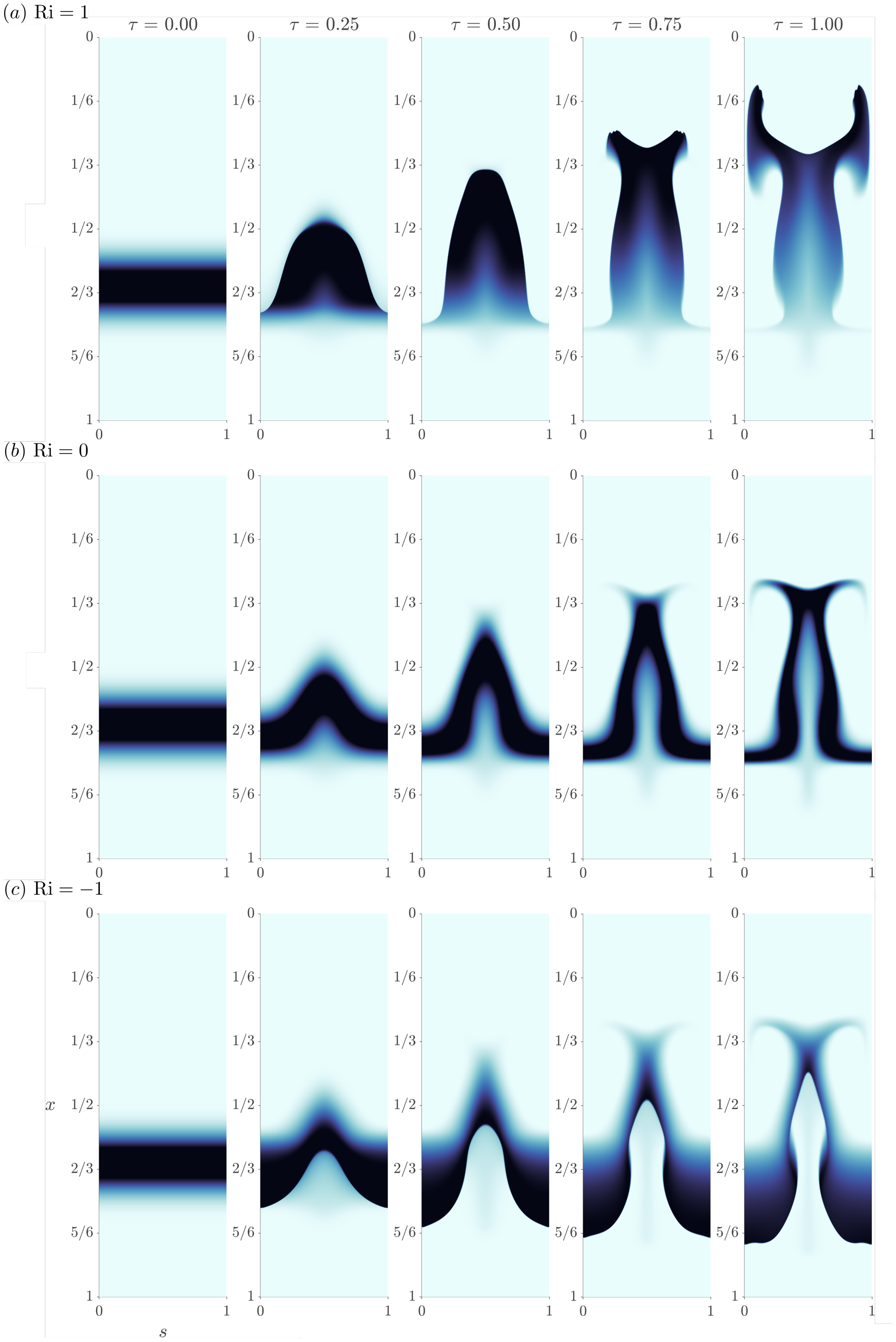

Figure 4.1: Distributions of width-averaged concentration $\int_0^1 c_0 \mathrm{d}\eta$ at different instants of time τ obtained numerically for $\beta = 0.5$, $\alpha = 3$, and $k = 0.5$ by integration of (4.28) for (a) $Ri = 1$, (b) $Ri = 0$, and (c) $Ri = -1$ using the boundary condition defined below in (4.32).

the Schmidt number ($1 \ll S \ll \varepsilon^{-2}$) only considers the convection due to the width-averaged axial and azimuthal velocities, for the variable eccentricity geometry there is no transport across the canal width and the solute has no mechanism to escape the closed recirculation regions. The solute remains trapped in its original vortex, corresponding to the streamlines shown in 2.8, and there is no bulk transport.

The solute is able to escape the recirculation regions when it is buoyant, shown in figure 4.1(a) for $Ri = 1$. Because the solute is lighter than the surrounding CSF, the solute has enough upward momentum to escape the closed vortex. Notably, the solute still favors the preferential path ($s = 0, 1$) given by the Lagrangian velocity for the uppermost vortex. The case of a heavy solute is also considered, shown in figure 4.1(c), corresponding to $Ri = -1$. In this case, the solute escapes its original vortex and sinks. It is important to recognize that the lubrication approximation removes the second derivative in x, and the only boundary condition on the velocities in x is zero flux at $x = 1$, which means that the buoyancy velocity is not necessarily $= 0$ at $x = 1$.

Future work should include the solution of (4.26), the transport equation in the limit $S \sim \varepsilon^{-2}$. For the non-buoyant case ($Ri = 0$), the solute is no longer trapped in closed recirculation regions. Diffusion across the width of the canal is expected to transport solute across the stagnation planes given by solely convective transport. Thus, the solute is expected to slowly leak into the above region, then follow the preferential path given by the Lagrangian motion and exit the canal. The results for (4.26) for $Ri = 0$ are shown on the right-hand-side panels of figure 3.8 for two different Schmidt numbers. For a light or heavy solute, the results are expected to be similar to those calculated for $1 \ll S \ll \varepsilon^{-2}$, with small differences due to diffusion. For Schmidt numbers of the order ε^{-2}, diffusion across the width of the canal is significant, but insufficient to uniformize the solute across the canal width. As a result, the solute initially located near the bounding surfaces $\eta = 0$ and $\eta = 1$, where the velocity is small, tends to remain at its initial location. It is therefore expected that the overall transport pattern will look very similar, with trace amounts of solute remaining near the initial condition, similar to the results presented earlier in 3.3 for $Ri = 0$ and a constant eccentricity.

4.4.2 DNS Comparison

In order to validate the simplified model of solute transport described above, full direct numerical simulations of the transport of a solute are calculated. Using the Eulerian velocity field calculated previously in section 2.5, the transport problem

$$\frac{\partial c}{\partial t^*} + \bar{v}^* \cdot \nabla c = \frac{\nu}{S} \nabla^2 c + \bar{g} \frac{\rho - \rho_d}{\rho} c, \tag{4.31}$$

using the Boussinesq approximation for the buoyancy term, is solved to study the slow-time dispersion of a solute, where ρ is the density of the CSF and ρ_d is the density of the solute or drug. Again, the asterisks denote dimensional variables. The initial spatial distribution of the solute, defined below in (4.32), is selected to represent the release of a drug in the lumbar region. The simulations are extended over a large number of cycles, corresponding to values of the long-time scale τ of order unity, and their results are compared with those of the simplified transport problem (4.28). Note that in the computations, no simplifications on the basis of the slenderness of the canal or the smallness of the stroke length are introduced.

The numerical solution of (4.31), using the results from the previous solution of (2.64)–(2.65), is carried out with the finite-volume solver Ansys Fluent (Release 16.2), assuring second-order accuracy in time and in space. The same dimensional parameters are used here as are used to solve the flow field. The kinematic viscosity, appearing in (3.41), is taken to be $\nu = 0.698 \times 10^{-6}\,\mathrm{m}^2/\mathrm{s}$, the value corresponding to water at 36.8° C. The dimensions of the domain for the two configurations shown in figures 2.3(b) and (c) are $L = 0.6\,\mathrm{m}$, $R_e = 5\,\mathrm{mm}$, and $R_i = 4\,\mathrm{mm}$, corresponding to a canal with characteristic width $h_c = R_e - R_i = 1\,\mathrm{mm}$ and constant inner perimeter $\ell_c = 2\pi R_i \simeq 25\,\mathrm{mm}$. In all computations, the dimensionless eccentricity is taken to be

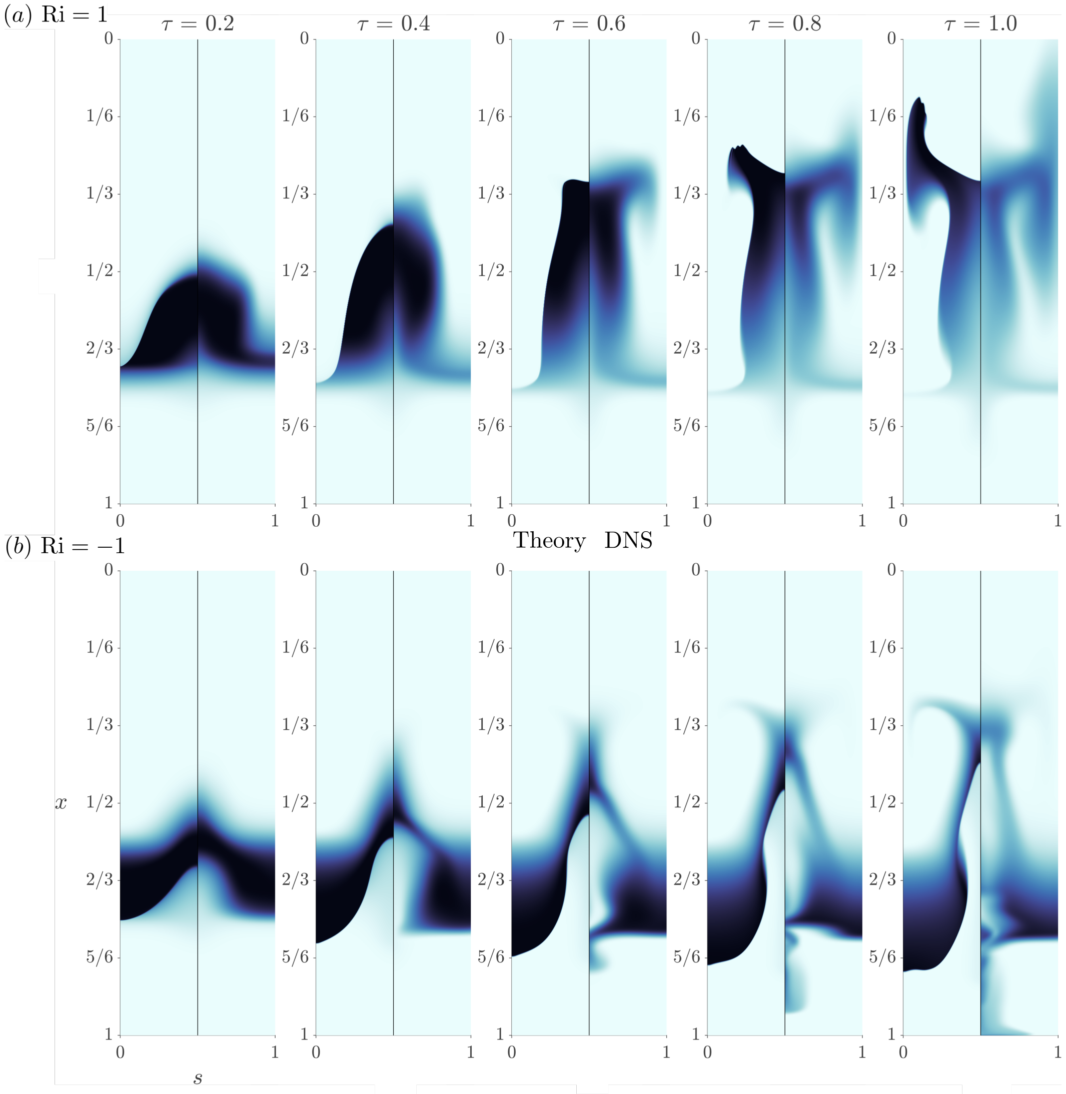

Figure 4.2: Comparisons of the distributions of width-averaged concentration $\int_0^1 c_0 \mathrm{d}\eta$ at different instants of time τ obtained numerically for $\beta = 0.5$, $\alpha = 3$, and $k = 0.5$ by integration of (4.28) for (a) $Ri = 1$ and (b) $Ri = -1$. For each plot, the left-hand-side indicates the solution of (4.28) while the right-hand-side indicates the solution of the full Navier–Stokes and concentration equations via DNS.

$\beta = 0.5$. The canal deformation, given in (2.66), is evaluated for an angular frequency $\omega = 2\pi s^{-1}$, as corresponds approximately to the cardiac cycle, with the function $H'(x^*/L)$, given in (2.21), computed with $k = 0.5$ and $\alpha = (h_c^2\omega/\nu)^{1/2} = 3$, the latter value consistent with the parametric choice $h_c = 1\,\mathrm{mm}$, $\omega = 2\pi s^{-1}$, and $\nu = 0.698 \times 10^{-6}\,\mathrm{m}^2/\mathrm{s}$. In all computations, the reduced amplitude is taken to be $\varepsilon = 1/20$. Gravity is taken to be only in the x direction, corresponding to a standing or sitting subject.

We consider the temporal evolution of a bolus of solute released at the initial instant of time. The initial concentration is given by the truncated Gaussian distribution

$$c\,(x^*/L) = \min\left\{1, \frac{3}{2}\exp\left[-16^2\left(\frac{x^*}{L} - 0.65\right)^2\right]\right\}, \tag{4.32}$$

selected as representative of injection of a solute bolus in the upper lumbar region. Predictions obtained by integrating the time-averaged (4.28) in the long time scale $\tau = \varepsilon^2 t = \varepsilon^2 \omega t^*$ for $0 \leq \tau \leq 2$ are compared in figure 4.2 with results of integrations of (4.31) for $0 \leq \omega t^* \leq 200$. The figure shows distributions of width-averaged concentration for different times.

Figure 4.2(a) shows good agreement between the model and the DNS for $Ri = 1$. The DNS shows some diffusion effects, as shown by the residual concentration at the initial condition as τ increases. While the DNS shows the same overall pattern, the concentration is not as sharp, also due to diffusion effects. The solute reaches the canal entrance at $\tau = \varepsilon^2 t \approx 1.22$, following the same preferential path as found in the case without buoyancy.

The comparison for $Ri = -1$, shown in figure 4.2(b), is less accurate. This can be partially attributed to the boundary condition at $x = 1$. While the DNS employs a no-penetration boundary condition, the model can only define a zero-flux boundary condition due to the lubrication approximation. The difference caused by the boundary condition is more noticeable for the $Ri = -1$ case, since the solute approaches the $x = 1$ boundary. The DNS is likely the more accurate representation because of the boundary conditions.

4.5 Conclusions

A simplified model for the transport of a solute with a variable density in the spinal canal has been found analytically. The density of the solute leads to the definition of the Richardson number, which compares the buoyancy effects to the convective effects. Although the density differences between the solute and the CSF are small, the Richardson numbers are found to be of order unity. The domain is assumed to be doubly slender, following the conditions in (2.1), and the Womersley number α and dimensionless wave number k are assumed to be order unity while the parameter measuring the limited compliance ε, effectively measuring the stroke volume compared to the total volume of fluid in the canal, is assumed to be small. Using this small parameter, all variables are expanded asymptotically. At order ε, the transport and axial momentum equations are coupled and the steady-streaming velocity is now variable with τ due to the buoyancy component.

Results for the simplified transport model are presented for the variable eccentricity case for $Ri = 1$, corresponding to a light or hypobaric solute, and for $Ri = -1$, corresponding to a heavy or hyperbaric solute. Results are also shown for $Ri = 0$, which corresponds to an isobaric solute, for which the solute density equals the CSF density. For $1 \ll S \ll \varepsilon^{-2}$, the $Ri = 0$ case shows closed recirculation regions, and the solute can never exit the vortex from which it starts. However, the addition of buoyancy allows the solute to either rise or sink, depending on the relevant Richardson number. Future calculations will include solution of the $S \sim \varepsilon^{-2}$ case. It is expected that, similar to Chapter 3, convection will be found to dominate a majority of the transport behavior, with small differences due to the inclusion of diffusion.

The simplified model was compared to full DNS. Good agreement is found in particular for the $Ri = 1$ case, while the $Ri = -1$ case shows poor agreement. This is likely because the simplified model has a no-flux boundary condition at $x = 1$, due to the use of the lubrication approximation, while the DNS utilizes a no-penetration boundary condition at $x = 1$. The discrepancy is noticeable for the $Ri = -1$ case since the solute approaches the $x = 1$ boundary.

Additionally, the DNS, which makes no simplifications to the continuity, Navier–Stokes, and transport equations due to the slenderness or the distinguished limit of the Schmidt number, always finds a small amount of diffusion unlike the simplified model in the limit $1 \ll S \ll \varepsilon^{-2}$.

This chapter is coauthored with W. Coenen, C. Gutiérrez-Montes, and A. L. Sánchez. The dissertation author was the primary author of this chapter. The work presented in this chapter was partially supported by the National Science Foundation, grant number 1853954.

Chapter 5

Oscillating Flow Past a Streamwise Periodic Array of Circular Cylinders

5.1 Characteristic Scales

In order to gain some insight on the effect of nerve roots in the spinal canal, let us consider the flow configuration depicted in figure 5.1 in which a fluid of density ρ and kinematic viscosity ν moves with a harmonic velocity $U_\infty \cos(\omega t')$ past an infinite array of equally spaced identical cylinders aligned with the unperturbed stream. The semi-distance between the centers of contiguous cylinders L is assumed to be comparable to the cylinders radius a, their ratio defining the geometrical parameter $\ell = L/a \sim 1$. Attention is focused on situations when the characteristic stroke length U_∞/ω is small, as measured by the asymptotically small parameter

$$\varepsilon = \frac{U_\infty/\omega}{a} \ll 1. \tag{5.1}$$

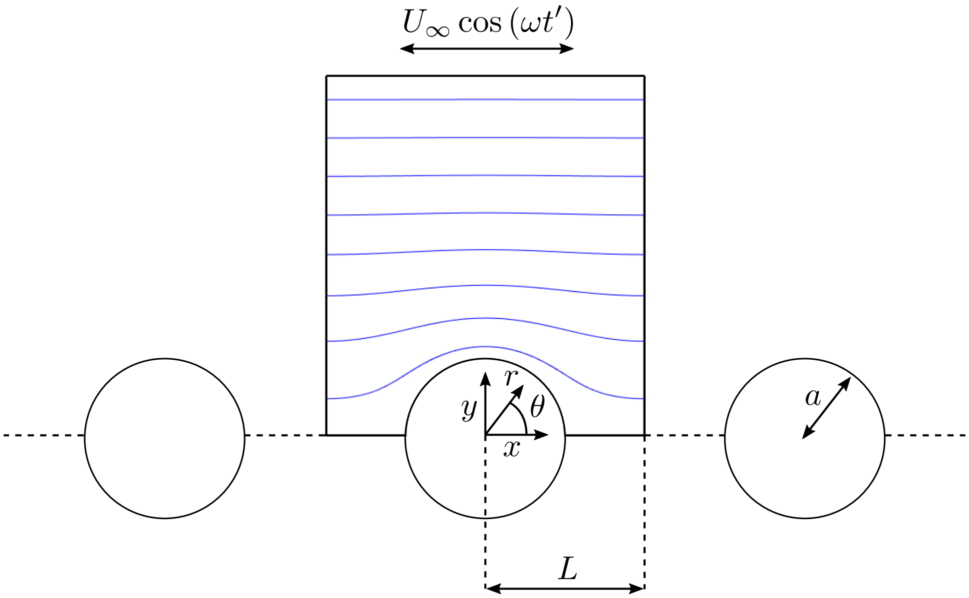

Figure 5.1: Schematic illustration of the cylinder array for $\ell = L/a = 2$, including the streamlines corresponding to the potential-flow solution.

The characteristic viscous time a^2/ν divided by the oscillation time ω^{-1} defines an additional flow parameter M^2, with

$$M = \left(\frac{a^2\omega}{\nu}\right)^{1/2} \tag{5.2}$$

representing the characteristic Womersley number of the flow, related to the Reynolds number by $Re = U_\infty a/\nu = \varepsilon M^2$. Following classical steady-streaming theory, we shall consider the solution for $\varepsilon \ll 1$ for which the velocity displays a harmonic time dependence at leading order, while the first-order corrections, of order ε, contain a steady contribution called steady streaming. For $M \sim 1$, steady streaming is governed by the steady Stokes equations subject to a forcing term arising from the convective acceleration, yielding one or two streaming vortices in each quadrant about the cylinder. In this limit, the Stokes-drift velocity, associated with the non-uniform harmonic oscillatory motion, will be shown to be comparable in magnitude to the steady-streaming velocity, with the sum of both contributions determining the time-averaged Lagrangian motion that governs the convective transport around the cylinders. Stokes drift will be shown to dominate for small values of the Womersley number, while steady streaming will be shown to dominate for large values of the Womersley number. Steady streaming, Stokes drift, and the Lagrangian motion all result in an inner vortex for small values of the Womersley number and develop an outer vortex as the Womersley number increases. The outer vortex dominates the behavior as M becomes very large.

5.2 Governing Equations

The problem is scaled with use of a, ω^{-1}, U_∞, $\rho\omega a U_\infty$ as characteristic values of length, time, velocity, and pressure. Since the resulting velocity $\mathbf{v}$ is periodic in the streamwise direction, the solution can be described by considering the flow about an individual cylinder, with the origin of the coordinate system placed at the cylinder center. While most of the description uses Cartesian coordinates $\mathbf{x} = (x, y)$ and velocity components $\mathbf{v} = (u, v)$, with x aligned in the direction of the unperturbed flow far from the cylinders, as indicated in figure 5.1 in the vicinity of the cylinder surface it shall prove convenient to use polar coordinates, such that $\mathbf{x} = (r, \theta)$ and $\mathbf{v} = (v_r, v_\theta)$. For the circular cylinders considered here, the flow is symmetric about the $y = 0$ plane, so that in the computations it suffices to consider the integration domain extending for $x^2 + y^2 > 1$ with $y > 0$ and $-\ell < x < \ell$, shown in figure 5.1. The velocity must satisfy the continuity and momentum equations

$$\nabla \cdot \mathbf{v} = 0, \tag{5.3}$$

$$\frac{\partial \mathbf{v}}{\partial t} + \varepsilon \mathbf{v} \cdot \nabla \mathbf{v} = -\nabla p + \frac{1}{M^2} \nabla^2 \mathbf{v}, \tag{5.4}$$

subject to the nonslip condition

$$\mathbf{v} = 0 \quad \text{at} \quad r = 1, \tag{5.5}$$

the far-field condition

$$\mathbf{v} = (\cos t, 0) \quad \text{as} \quad y \to \infty \quad \text{for} \quad -\ell \leq x \leq \ell, \tag{5.6}$$

the symmetry condition

$$\frac{\partial u}{\partial y} = v = 0 \quad \text{at} \quad y = 0 \quad \text{for} \quad 1 \leq |x| \leq \ell, \tag{5.7}$$

and the periodicity conditions

$$\left(u, v, \frac{\partial v}{\partial x}\right)(\ell, y, t) = \left(u, v, \frac{\partial v}{\partial x}\right)(-\ell, y, t) \quad \text{for} \quad 0 \leq y < \infty. \tag{5.8}$$

5.3 Velocity Field for $M \sim 1$

We describe the flow by introducing expansions for the different flow variables in powers of ε, i.e.

$$\mathbf{v} = \mathbf{v}_0 + \varepsilon \mathbf{v}_1 + \cdots \tag{5.9}$$

and $p = p_0 + \varepsilon p_1 + \cdots$. As seen below, the leading-order solution has a zero time average, i.e. $\langle \mathbf{v}_0 \rangle = 0$, with $\langle \cdot \rangle = \frac{1}{2\pi} \int_t^{t+2\pi} \cdot \, \mathrm{d}t$, whereas the first-order correction $\mathbf{v}_1$, accounting for the effects of convective acceleration, includes a nonzero steady-streaming component $\mathbf{v}_{SS} = \langle \mathbf{v}_1 \rangle$.

5.3.1 Leading-order Oscillatory Flow

At leading order, the convective acceleration is negligible and the resulting linear problem can be conveniently solved by introducing $\mathbf{v}_0 = \mathrm{Re}\left(\mathrm{e}^{\mathrm{i}t} \mathbf{V}_0\right)$ and $p_0 = \mathrm{Re}\left(\mathrm{e}^{\mathrm{i}t} P_0\right)$ with $\mathbf{V}_0(x, y) =$

(U_0, V_0) and $P_0(x,y)$ representing complex functions satisfying

$$\nabla \cdot \mathbf{V}_0 = 0, \quad \mathrm{i}\mathbf{V}_0 = -\nabla P_0 + \frac{1}{M^2}\nabla^2 \mathbf{V}_0 \tag{5.10}$$

with boundary conditions

$$\mathbf{V}_0 = 0 \quad \text{at} \quad r = 1, \tag{5.11}$$

$$\mathbf{V}_0 = (1,0) \quad \text{as} \quad y \to \infty \quad \text{for} \quad -\ell \leq x \leq \ell, \tag{5.12}$$

$$\frac{\partial U_0}{\partial y} = V_0 = 0 \quad \text{at} \quad y = 0 \quad \text{for} \quad 1 \leq |x| \leq \ell, \tag{5.13}$$

$$\left(\mathbf{V}_0, \frac{\partial V_0}{\partial x}\right)(\ell, y) = \left(\mathbf{V}_0, \frac{\partial V_0}{\partial x}\right)(-\ell, y) \quad \text{for} \quad 0 \leq y < \infty, \tag{5.14}$$

as follows at leading order from (5.3)–(5.8)

For a general value of M, the resulting velocity function $\mathbf{V}_0(x,y)$ has real and imaginary parts. In the limit of steady creeping flow $M \ll 1$, the solution is real everywhere. In the inviscid limit $M \gg 1$, the solution contains an imaginary part only in the thin Stokes layer of thickness $1/M$ that develops on the cylinder surface, outside of which the flow is irrotational, such that $\mathbf{V}_0(x,y) = \nabla \Phi_0$. The associated velocity potential satisfies $\nabla^2 \Phi_0 = 0$ subject to the boundary conditions

$$\frac{\partial \Phi_0}{\partial r} = 0 \quad \text{at} \quad r = 1, \tag{5.15}$$

$$\Phi_0 = x \quad \text{as} \quad y \to \infty \quad \text{for} \quad -\ell \leq x \leq \ell, \tag{5.16}$$

$$\frac{\partial \Phi_0}{\partial y} = 0 \quad \text{at} \quad y = 0 \quad \text{for} \quad 1 \leq |x| \leq \ell, \tag{5.17}$$

$$\left(\Phi_0, \frac{\partial \Phi_0}{\partial x}\right)(\ell, y) = \left(\Phi_0, \frac{\partial \Phi_0}{\partial x}\right)(-\ell, y) \quad \text{for} \quad 0 \leq y < \infty. \tag{5.18}$$

This problem, considered recently by [14], provides in particular the velocity distribution on the surface of the cylinder

$$\mathcal{V} = \left.\frac{\partial \Phi_0}{\partial \theta}\right|_{r=1}, \tag{5.19}$$

to be used later in analyzing steady streaming for $M \sim \varepsilon^{-1} \gg 1$. Distributions of $\mathcal{V}(\theta)$ are shown in figure 5.2 for different values of ℓ. For illustrative purposes, the streamlines corresponding to the specific case $\ell = 2$ are included in the schematic of figure 5.1.

Numerical integration is in general needed to solve the above problem, the only exception being the limiting solution arising for $\ell \gg 1$, corresponding to flow over a single cylinder, for which an analytic solution is available [27].

5.3.2 Steady Streaming

The steady-streaming velocity $\mathbf{v}_{\mathrm{SS}} = \langle \mathbf{v}_1 \rangle = (u_{\mathrm{SS}}, v_{\mathrm{SS}})$ is determined from the problem that arises at the following order. Collecting terms of order ε in (5.3) and (5.4) and taking the time average leads to

$$\nabla \cdot \mathbf{v}_{\mathrm{SS}} = 0, \quad \frac{1}{2}\mathrm{Re}\,(\mathbf{V}_0 \cdot \nabla \mathbf{V}_0^*) = -\nabla \langle p_1 \rangle + \frac{1}{M^2}\nabla^2 \mathbf{v}_{\mathrm{SS}}, \tag{5.20}$$

after writing $\langle \mathbf{v}_0 \cdot \nabla \mathbf{v}_0 \rangle = \frac{1}{2}\mathrm{Re}\left(\mathbf{V}_0 \cdot \nabla \mathbf{V}_0^*\right)$, which follows from the identity $\langle \mathrm{Re}(\mathrm{e}^{\mathrm{i}t}A)\,\mathrm{Re}(\mathrm{e}^{\mathrm{i}t}B)\rangle = \mathrm{Re}(AB^*)/2$, applicable to any generic time-independent complex functions A and B, with the asterisk $*$ denoting complex conjugates. The result, symmetric about the $y = 0$ plane, can be obtained by integrating (5.20) in the first quadrant subject to the boundary conditions

$$\mathbf{v}_{\mathrm{SS}} = 0 \quad \text{at} \quad r = 1, \tag{5.21}$$

$$\mathbf{v}_{\mathrm{SS}} \to 0 \quad \text{as} \quad y \to \infty \quad \text{for} \quad 0 \leq x \leq \ell, \tag{5.22}$$

$$\frac{\partial u_{\mathrm{SS}}}{\partial y} = v_{\mathrm{SS}} = 0 \quad \text{at} \quad y = 0 \quad \text{for} \quad 1 \leq x \leq \ell, \tag{5.23}$$

$$u_{\mathrm{SS}} = \frac{\partial v_{\mathrm{SS}}}{\partial x} = 0 \quad \text{at} \quad x = 0 \quad \text{for} \quad 1 \leq y < \infty, \tag{5.24}$$

$$u_{\mathrm{SS}} = \frac{\partial v_{\mathrm{SS}}}{\partial x} = 0 \quad \text{at} \quad x = \ell \quad \text{for} \quad 0 \leq y < \infty. \tag{5.25}$$

5.3.3 Stokes Drift

As seen above, the Eulerian velocity field for $\varepsilon \ll 1$ includes a harmonic leading-order term $\mathbf{v}_0 = \mathrm{Re}\left(\mathrm{e}^{\mathrm{i}t}\mathbf{V}_0\right)$ and a first-order correction $\mathbf{v}_1$, the latter having a nonzero steady-streaming component $\mathbf{v}_{\mathrm{SS}} = \langle \mathbf{v}_1 \rangle$. The time-averaged Lagrangian velocity of a fluid particle,

$$\mathbf{v}_{\mathrm{L}} = \mathbf{v}_{\mathrm{SS}} + \mathbf{v}_{\mathrm{SD}}, \tag{5.26}$$

accounting for the slow cumulative displacement of the particle over multiple cycles, has in general an additional Stokes-drift component (see, e.g. [69]) given by

$$\mathbf{v}_{\mathrm{SD}} = \left\langle \int \mathbf{v}_0 \mathrm{d}t \cdot \nabla \mathbf{v}_0 \right\rangle, \tag{5.27}$$

which can be written in the form

$$\mathbf{v}_{\mathrm{SD}} = \frac{1}{2} \mathrm{Im}\left(\mathbf{V}_0 \cdot \nabla \mathbf{V}_0^*\right), \tag{5.28}$$

by using $\mathbf{v}_0 = \mathrm{Re}\left(\mathrm{e}^{\mathrm{i}t}\mathbf{V}_0\right)$ along with the identity $\langle \mathrm{Re}(\mathrm{i}\mathrm{e}^{\mathrm{i}t}A)\,\mathrm{Re}(\mathrm{e}^{\mathrm{i}t}B)\rangle = -\mathrm{Im}(AB^*)/2$. It is worth noting that the real part of the complex function $\frac{1}{2}\mathbf{V}_0 \cdot \nabla \mathbf{V}_0^*$ determines the steady streaming, as revealed by (5.20), whereas its imaginary part is the Stokes-drift velocity (5.28), which is identically zero when the function $\mathbf{V}_0$ is real.

5.3.4 Results for $\ell = 2$

The leading order solution, given by (5.10)–(5.14), is solved in terms of $\mathbf{V}_0 = \nabla\Phi_0 + \hat{\mathbf{V}}$. First Φ_0 was determined, subject to the conditions (5.15)–(5.18), from which cylinder slip velocity $\mathcal{V}$ was determined. Then $\hat{\mathbf{V}}$, which carries the vorticity that diffuses from the cylinder surface was calculated, which is subject to the same leading order equations but satisfies the modified boundary conditions $\hat{\mathbf{V}} \to 0$ as $y \to \infty$ and $\hat{\mathbf{V}} = (\hat{V}_r, \hat{V}_\theta) = (0, -\mathcal{V})$ at $r = 1$. Stokes drift velocities were calculated from the leading-order velocities. Steady streaming was determined as the solution of (5.20)–(5.25). From these results, the steady streaming, Stokes drift, and Lagrangian streamfunctions, ψ_{SS}, ψ_{SD}, and ψ_L respectively, were found, all subject to the condition that $\psi = 0$ around the entire edge of the computational domain.

Numerical results were obtained using COMSOL. Though results in figure 5.3 are presented for $0 \leq y \leq 5$, the computational domain extends from $0 \leq y \leq 50$ and $-\ell \leq x \leq \ell$. The computation utilized an unstructured triangular mesh with more elements concentrated toward the cylinder surface. Figure 5.2 contains results for many values of ℓ, for which a different mesh was used for each calculation. 38730 elements were used for $\ell = 1.1$, 53296 elements were used for $\ell = 1.5$, 64528 elements were used for $\ell = 2$, 77748 elements were used for $\ell = 3$, and 93976 elements were used for $\ell = 5$. Figures 5.3 and 5.4 correspond to $\ell = 2$, for which 64528 elements were used again. Residuals, estimations of the algebraic error, were found to be of the order 10^{-6} or smaller for all computed quantities, much smaller than any of the presented quantities. For all computations in this section, the equations were written in weak form and the PARDISO direct linear solver was used.

Figure 5.2 shows the slip velocity on the cylinder surface for a variety of ℓ values, obtained from integration of $\nabla^2\Phi_0 = 0$ subject to the boundary conditions stated in (5.15)–(5.18). As

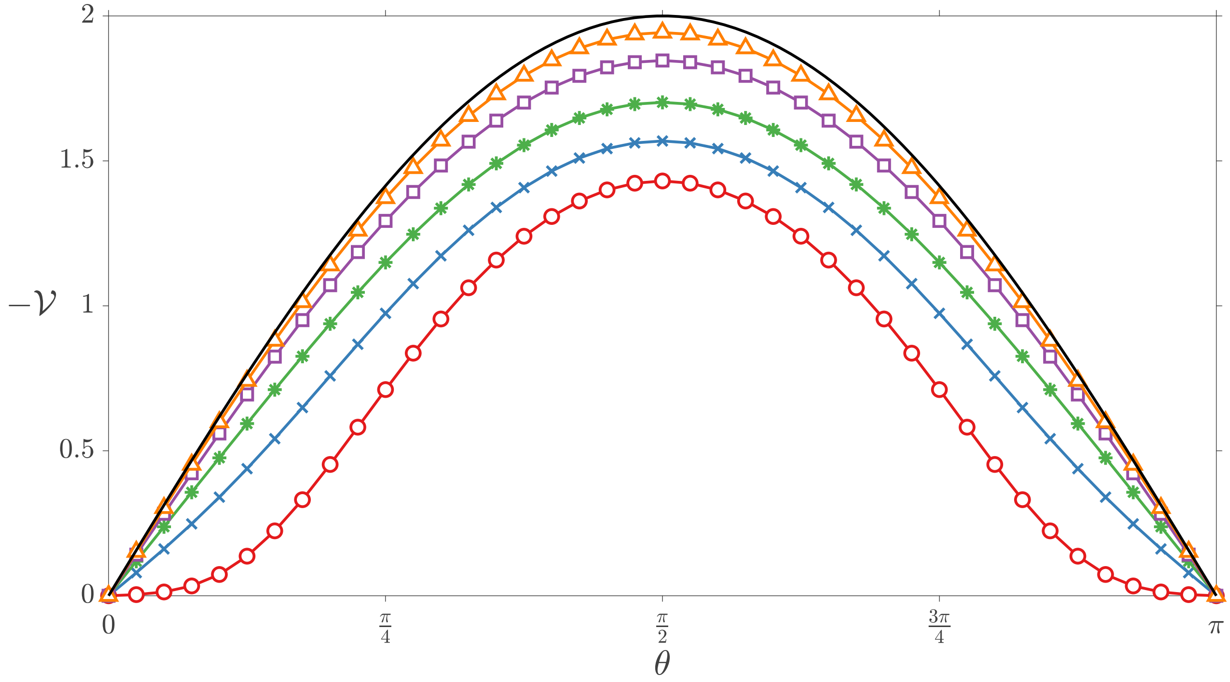

Figure 5.2: The potential-flow slip velocity on the cylinder surface $\mathcal{V}(\theta) = \partial\Phi_0/\partial\theta|_{r=1}$ as obtained numerically by integration of $\nabla^2\Phi_0 = 0$ with the boundary conditions stated in (5.15)–(5.18) for $\ell = 1.1$ (red circles), $\ell = 1.5$ (blue crosses), $\ell = 2$ (green stars), $\ell = 3$ (purple squares), and $\ell = 5$ (orange triangles). A solid black line is used to represent the limiting velocity found for $\ell \to \infty$, which reduces to the familiar solution $\mathcal{V} = -2\sin\theta$ corresponding to an isolated cylinder.

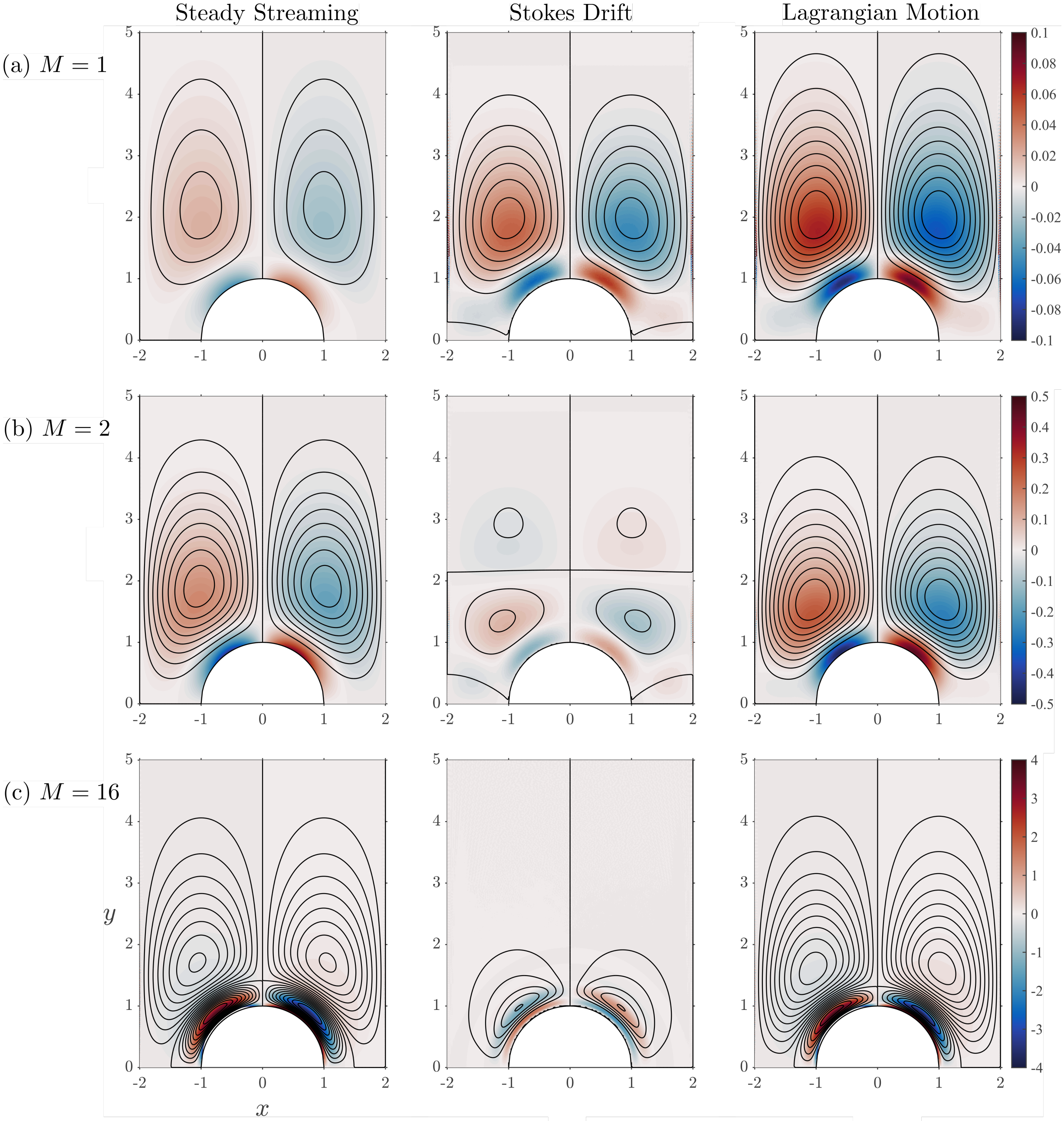

Figure 5.3: Streamlines (black lines) and contours of the vorticity for the steady streaming, Stokes drift, and Lagrangian velocities for (a) $M = 1$, (b) $M = 2$, and (c) $M = 16$. Note that each M value has a different range of values for vorticity, shown by the color bar on the right.

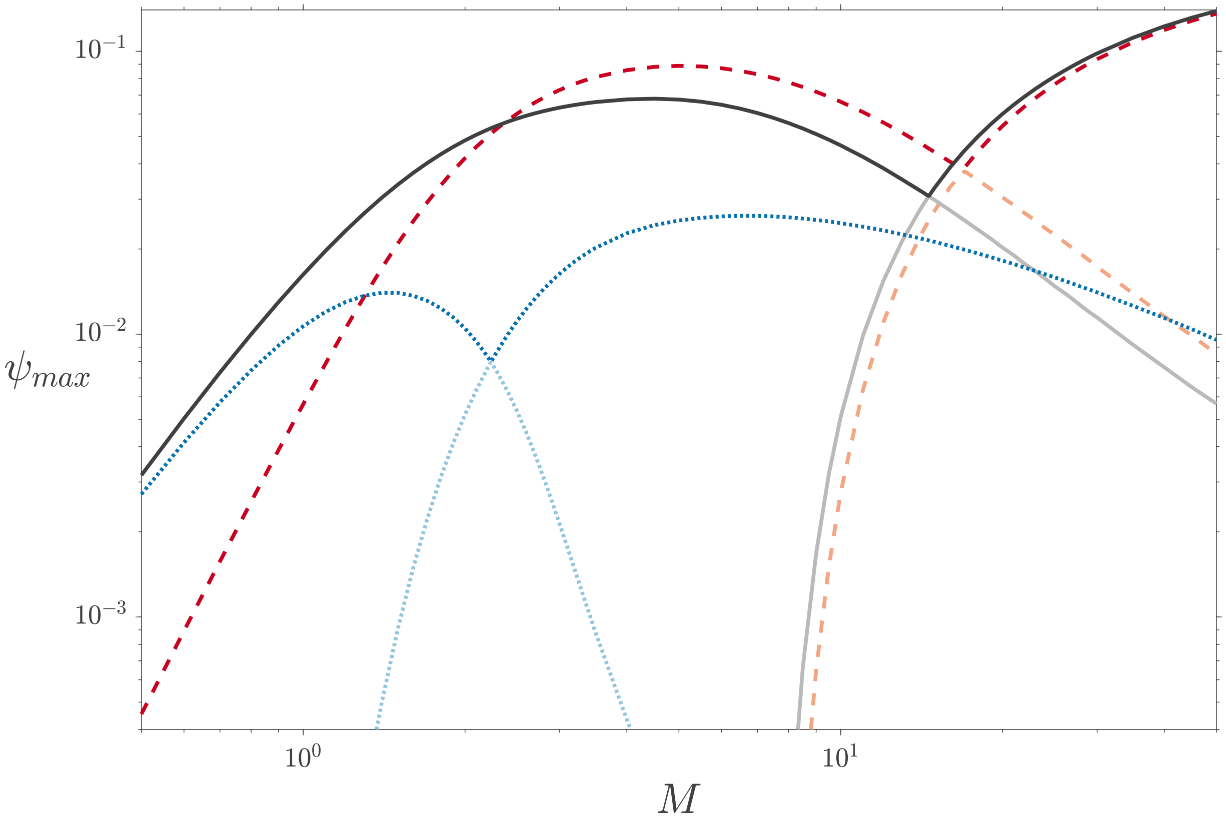

Figure 5.4: Local maxima of the steady streaming (red), Stokes drift (blue), and Lagrangian (black) streamfunctions. For each streamfunction, the higher maximum value is in a darker color and the lower maximum value is in a lighter color.

ℓ increases, the velocity distribution approaches that of the theoretical case $\ell \to \infty$, for which $\mathcal{V} = -2\sin\theta$. While results for $\ell > 5$ are not shown on the figure, it is found that for $\ell \approx 8$, $\mathcal{V}$ is virtually indistinguishable from the theoretical solution for a single cylinder. As ℓ decreases, the slip velocity decreases in magnitude since the smaller gap between cylinders forces the fluid to slow down. For $\ell = 1.1$, $\mathcal{V}$ is very small near $\theta = 0$, π, since the fluid has very little space to flow.

Figure 5.3 shows streamlines and vorticity data for steady streaming, Stokes drift, and the Lagrangian motion. In these plots, contours of the streamfunction were taken for the velocity with the highest maximum, and those same contours were used for each plot in the row. If a plot has fewer contours, then the streamfunction is smaller in magnitude, which corresponds to less overall movement of fluid. Each row also uses the same color bar for the vorticity. For $M = 1$, steady streaming and the Lagrangian motion show a single vortex in each quadrant, while Stokes drift has a very small additional vortex near $y = 0$. All three plots show vorticity concentrated at the cylinder surface as well as further from the cylinder. It is clear from the vorticity magnitude and the number of streamlines that Stokes drift is the main contributor to the Lagrangian motion and that the effects of steady streaming and Stokes drift are additive for this value of M. For $M = 2$, again steady streaming and the Lagrangian motion show a single vortex in each quadrant, but Stokes drift now has three vortices in each quadrant. The additional vortex enters from large y, swirling in the opposite direction. Although the vorticity of Stokes drift is relatively small, it can be seen that the outermost vortex has cancelled out some of the vorticity present in steady streaming, leading to Lagrangian vortices that are slightly smaller. For $M = 16$, steady streaming and Lagrangian motion both show two vortices while Stokes drift shows a single vortex. Steady streaming clearly dominates for this value of the Womersley number, with the outer vortex again approaching from large y with the opposite sign. The outermost vortex has now dominated the behavior of Stokes drift, with the smaller vortices negligibly small and virtually invisible. As M increases further, the steady streaming and Lagrangian outer vortices begin to dominate with the inner vortices shrinking down to the surface of the cylinder as a boundary layer.

Figure 5.4 shows local maxima of the steady streaming, Stokes drift, and Lagrangian streamfunctions. Since all streamfunctions are identically zero at the cylinder surface, this effectively represents the amount of fluid motion for each of these velocity fields. The plot sometimes contains two values of the local maxima for a single M value, which means that the streamfunction has two local maxima, indicating two vorticies. The higher value is represented by the darker color. Although Stokes drift sometimes has an additional third vortex near the cylinder surface, as can be seen in figure 5.3(a) and (b), these values are not included as they are very small by comparison. For $M = 0.5$, Stokes drift is the dominant contribution to the overall Lagrangian motion and all velocities exhibit a single vortex in each quadrant. Between $M = 1$ and 2, steady streaming begins to dominate the Lagrangian motion and the Stokes drift outer vortex begins to approach the cylinder. Between $M = 2$ and 3, the Stokes drift outer vortex begins to dominate over the inner vortex, leading to the sharp dip in the overall maximum. Since the outer Stokes drift vortex is swirling the opposite direction, the total Lagrangian motion is less than the steady streaming motion. Between $M = 8$ and 9, the outer vortices for steady streaming and Lagrangian motion start to become visible. Between $M = 10$ and 11, the outer vortices for both steady streaming and Lagrangian motion begin to dominate over the inner vorticies, leading to similar sharp dips in the overall maximum. Now, both steady streaming and Stokes drift are dominated by the outer vortices, which swirl in the same direction, so additive Lagrangian motion is now the largest. As M continues to increase, steady streaming now dominates the overall Lagrangian motion.

5.4 Transport of a Passive Scalar

5.4.1 Governing Equations

Consider now the transport of a passive scalar of diffusivity $\kappa = \nu/S$, described by the transport equation

$$\frac{\partial c}{\partial t} + \varepsilon \mathbf{v} \cdot \nabla c = \frac{1}{SM^2} \nabla^2 c \tag{5.29}$$

where $c(\mathbf{x},t)$ is the scalar concentration and $S = \nu/\kappa$ is its Schmidt number. As is clear from the above equation, for solutes with $S \sim 1$, typical of gaseous molecules, transport is dominated by diffusion. For diffusive transport in liquids, however, the solute diffusivity is much smaller than the kinematic viscosity, yielding values of S that often exceed $S = 10^3$. To investigate transport in that case, we consider the distinguished limit $S \sim \varepsilon^{-2} \gg 1$, in which the diffusion time a^2/κ becomes comparable to the residence time of the slow Lagrangian motion $\varepsilon^{-2}\omega^{-1}$. To describe this limit, we follow the two-time scale formalism employed earlier, so that the transport equation for the scalar concentration $c(\mathbf{x},t,\tau)$ becomes

$$\frac{\partial c}{\partial t} + \varepsilon^2 \frac{\partial c}{\partial \tau} + \varepsilon \mathbf{v} \cdot \nabla c = \frac{\varepsilon^2}{\sigma M^2} \nabla^2 c, \tag{5.30}$$

where $\sigma = \varepsilon^2 S$ is the rescaled Schmidt number, of order unity in the distinguished limit $S \sim \varepsilon^{-2} \gg 1$ considered here. Substituting the expansion given in (5.9) for the Eulerian velocity along with the presumed expansion

$$c(\mathbf{x},t,\tau) = c_0(\mathbf{x},t,\tau) + \varepsilon c_1(\mathbf{x},t,\tau) + \varepsilon^2 c_2(\mathbf{x},t,\tau) + \cdots, \tag{5.31}$$

where all terms $c_i(\mathbf{x},t,\tau)$ are 2π periodic in the short-time scale t, leads to a series of problems that can be solved sequentially.

At leading order we find

$$\frac{\partial c_0}{\partial t} = 0, \tag{5.32}$$

indicating that $c_0 = \hat{c}_0(\mathbf{x}, \tau)$ is only a function of the long time scale, the small-time fluctuations associated with the pulsating flow entering only at higher order. The equation that arises at the following order (ε)

$$\frac{\partial c_1}{\partial t} + \mathbf{v}_0 \cdot \nabla \hat{c}_0 = 0, \tag{5.33}$$

can be readily integrated to yield

$$c_1 = -\int \mathbf{v}_0 \mathrm{d}t \cdot \nabla \hat{c}_0 + \hat{c}_1(\mathbf{x}, \tau), \tag{5.34}$$

which can be used when taking the time average of the equation that arises at the following order

$$\frac{\partial c_2}{\partial t} + \frac{\partial \hat{c}_0}{\partial \tau} + \mathbf{v}_1 \cdot \nabla \hat{c}_0 + \mathbf{v}_0 \cdot \nabla c_1 = \frac{1}{\sigma M^2} \nabla^2 \hat{c}_0, \tag{5.35}$$

to finally give

$$\frac{\partial \hat{c}_0}{\partial \tau} + \mathbf{v}_{\mathrm{L}} \cdot \nabla \hat{c}_0 = \frac{1}{\sigma M^2} \nabla^2 \hat{c}_0 \tag{5.36}$$

for the transport equation that describes the scalar dispersion in the long time scale. As anticipated, scalar diffusion competes with the convective transport driven by the time-averaged Lagrangian velocity (5.26).

5.4.2 Results for $M = 5$ and $\ell = 2$

Since transport can occur over multiple cylinders, a large computational domain with many cylinders was utilized to capture motion between Lagrangian cells. For the results presented here, nine cylinders were used in the computational domain with $\ell = 2$. The entire domain had a length of 40 and a width of 30, and used 82538 unstructured triangular elements, with more elements concentrated at the cylinder surface. The equations were all written in strong form and the MUMPS direct linear solver was used.

The leading order velocity field was calculated using equations (5.10), with the boundary conditions $\mathbf{V}_0 \to 0$ on all cylinder surfaces and $\mathbf{V}_0 = (1,0)$ on all domain edges, as $(x,y) \to \infty$. The first order corrections to the velocity field were calculated using equation (5.20), with the boundary conditions $\mathbf{v}_{SS} = 0$ on all cylinder surfaces and all domain edges as $(x,y) \to \infty$. Finally the transport equation (5.36) was solved given an initial condition

$$c_i(\mathbf{x},t) = \exp\left(-\frac{(x-2)^2}{2\cdot 0.5^2} - \frac{(y-2)^2}{2\cdot 0.5^2}\right), \tag{5.37}$$

a Gaussian drop of solute centered at $(2,2)$ with standard deviation 0.5.

Figure 5.5 shows results of transport for $M = 5$ and $\ell = 2$. Three different values of the rescaled Schmidt number $\sigma = \varepsilon^2 S$ are shown, $\sigma = 5,\ 20,\ 100$, corresponding to liquid-liquid mixtures with large Schmidt numbers $S \sim \varepsilon^{-2} \gg 1$. As σ increased, diffusion becomes visibly less significant and the convection caused by Lagrangian motion becomes more pronounced and noticeable. For $\sigma = 1$, not shown in the figure, the initial drop of solute diffuses radially outward, with very small effects from the location of the cylinders. Therefore, for small values of the rescaled Schmidt number, diffusion dominates the transport and there is very little convection due to the Lagrangian vortices. However, for large values of the Schmidt number, corresponding to liquids with very low diffusivities, convective transport within cells is clearly visible but diffusive transport between cells is limited.

5.5 Conclusions

The goal here is to study the effects of multiple cylinders on the Lagrangian motion and transport of a solute. It is found that for $\ell > 8$, the potential solution approaches the theoretical solution for $\ell \to \infty$. For $M \sim 1$, it is found that the long-term Lagrangian motion is caused by

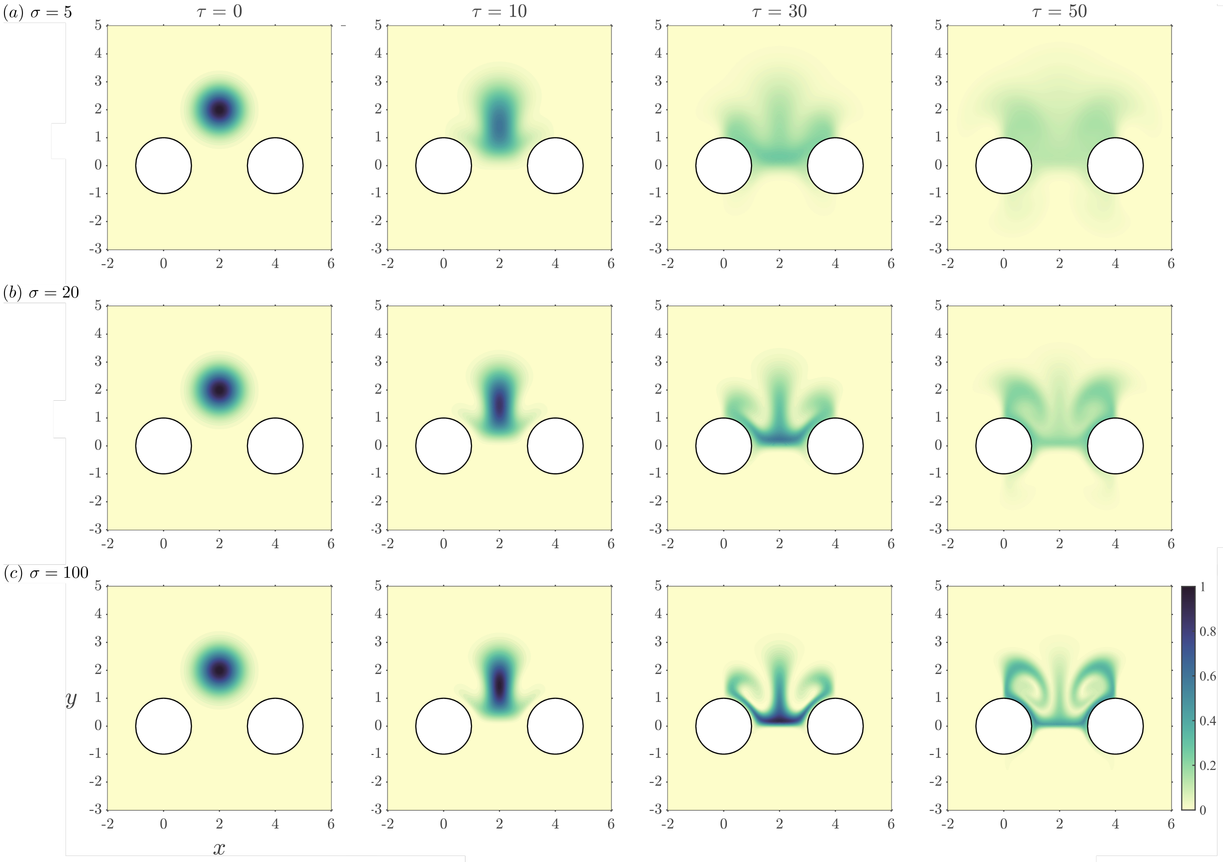

Figure 5.5: Transport of a solute for $M = 5$, $\ell = 2$, and (a) $\sigma = 5$, (b) $\sigma = 20$, and (c) $\sigma = 100$.

the combined effects of steady streaming and Stokes drift. As M increases, steady streaming, Stokes drift, and the Lagrangian motion all have an additional vortex which enters from large y that swirls in the opposite direction. As M continues to increase, this vortex gets larger and the original vortex shrinks down to the surface of the cylinder. For $M \approx 2-10$, steady streaming has a single vortex but Stokes drift has an outer vortex swirling in the opposite direction, so the Lagrangian motion is weaker than steady streaming alone. For $\sigma < 1$ the transport is dominated by diffusion and the convection caused by the Lagrangian motion is not visible. For $\sigma > 100$, however, the transport is dominated by convection and very little diffusion between cells occurs. For $1 < \sigma < 100$, both diffusion and convection affect the transport.

This work represents the first step in studying the effects of the nerve roots on flow and transport in the spinal canal. There are several open questions that should be studied in detail. For instance, the nerve roots in the spinal canal are not infinitely long, but confined axially. Though the effects of confinement might be localized to a small region near the canal walls, additional streaming patterns caused by this axial confinement are worth studying. Furthermore, the distinguished limit $M \sim \varepsilon^{-1} \gg 1$, in which the outer steady-streaming vortex dominates the behavior and the inner vortex is confined to the cylinder surface, should be analyzed theoretically and numerically following [73]. The additional limit of oscillation amplitude $\varepsilon \sim 1$ or $\varepsilon \gg 1$ should also be studied as that more accurately represents the oscillation amplitude in the spinal canal relative to the typical radii of the nerve roots. Finally the flow at infinity could be modified to be more realistic. A more accurate velocity field could be analyzed as Fourier series of terms, although that may not lead to significant changes to the behavior as it will simply be a sum of the patterns already seen here. The symmetry may be broken, however, by introducing a small steady component to the velocity field at infinity, which would more accurately represent the flow in the spinal canal which is an oscillatory flow plus a small steady component.

This chapter is currently being prepared for submission for publication of the material along with W. Coenen and A. L. Sánchez. The dissertation author was primary the author of this

material. The work presented in this chapter was partially supported by the National Science Foundation, grant number 1853954.

Chapter 6

Future Work

6.1 Extension for a General Cranial Pressure

Thus far we have analyzed the flow of cerebrospinal fluid in the spinal canal for a simple sinusoidal function representing the intracranial pressure. The intracranial pressure, however, is a more complicated function typically exhibiting three peaks with every heartbeat and an additional lower frequency modulation due to respiration [58].

In the above analysis, the flow is driven by the periodic pressure function $\Pi(t) = \cos t$, where $\Pi(t)$ is scaled with the amplitude of the cranial pressure $(\Delta p)_c$. Here the analysis is generalized for a general dimensionless periodic function, assumed to be expressible in the Fourier-series form

$$\Pi(t) = \mathrm{Re}\left(\sum_{n=1}^{\infty} a_n \mathrm{e}^{\mathrm{i}nt}\right) \tag{6.1}$$

involving the complex coefficients a_n with $|a_1| = 1$, as corresponds to defining the characteristic pressure fluctuation $(\Delta p)_c$ as the amplitude of the first Fourier mode. The problem can be similarly solved by introducing regular expansions of the form

$$
\begin{aligned}
&u = u_0 + \varepsilon u_1 + \cdots, v = v_0 + \varepsilon v_1 + \cdots, w = w_0 + \varepsilon w_1 + \cdots, \\
&h' = h'_0 + \varepsilon h'_1 + \cdots, p' = p'_0 + \varepsilon p'_1 + \cdots, \hat{p} = \hat{p}_0 + \varepsilon \hat{p}_1 + \cdots,
\end{aligned} \tag{6.2}
$$

where the leading-order terms correspond to periodic oscillatory flow with zero time average $\langle\cdot\rangle = \frac{1}{2\pi}\int_0^{2\pi} \cdot \, \mathrm{d}t = 0$.

6.1.1 Leading-order Solution

At leading-order in the limit $\varepsilon \ll 1$ the solution satisfies the linear equations

$$
\frac{1}{\ell}\frac{\partial}{\partial x}(\ell u_0) - \frac{\partial \bar{h}}{\partial x}\frac{\eta}{\bar{h}}\frac{\partial u_0}{\partial \eta} + \frac{1}{\bar{h}}\frac{\partial v_0}{\partial \eta} + \frac{1}{\ell}\frac{\partial w_0}{\partial s} - \frac{1}{\ell}\frac{\partial \bar{h}}{\partial s}\frac{\eta}{\bar{h}}\frac{\partial w_0}{\partial \eta} = 0 \tag{6.3}
$$

$$
\frac{\partial u_0}{\partial t} = -\frac{\partial p'_0}{\partial x} + \frac{1}{\alpha^2 \bar{h}^2}\frac{\partial^2 u_0}{\partial \eta^2} \tag{6.4}
$$

$$
\frac{\partial w_0}{\partial t} = -\frac{1}{\ell}\frac{\partial \hat{p}_0}{\partial s} + \frac{1}{\alpha^2 \bar{h}^2}\frac{\partial^2 w_0}{\partial \eta^2}, \tag{6.5}
$$

$$
h'_0 = \gamma(\Pi + k^2 p'_0). \tag{6.6}
$$

Following chapters 2, we write the velocity, pressure, and deformation in the form

$$
\begin{aligned}
u_0 &= \mathrm{Re}\left(\mathrm{i}\sum_{n=1}^{\infty} a_n n \mathrm{e}^{\mathrm{i}nt} U_n\right), v_0 = \mathrm{Re}\left(\mathrm{i}\sum_{n=1}^{\infty} a_n n \mathrm{e}^{\mathrm{i}nt} V_n\right), w_0 = \mathrm{Re}\left(\mathrm{i}\sum_{n=1}^{\infty} a_n n \mathrm{e}^{\mathrm{i}nt} W_n\right), \\
p'_0 &= \mathrm{Re}\left(\sum_{n=1}^{\infty} a_n n^2 \mathrm{e}^{\mathrm{i}nt} P'_n\right), \hat{p}_0 = \mathrm{Re}\left(\sum_{n=1}^{\infty} a_n n^2 \mathrm{e}^{\mathrm{i}nt} \hat{P}_n\right), h'_0 = \mathrm{Re}\left(\sum_{n=1}^{\infty} a_n \mathrm{e}^{\mathrm{i}nt} H'_n\right),
\end{aligned} \tag{6.7}
$$

consistent with (6.1). Note that in this case we anticipate the dependence of each quantity with n and a_n.

The canal deformation is related with the streamwise pressure variation through (6.6), which provides

$$
H'_n = \gamma(1 + n^2 k^2 P'_n) \tag{6.8}
$$

upon substitution of (6.7). The axial and azimuthal velocity are given in terms of the components of the pressure gradient by

$$U_n = \frac{\mathrm{d}P'_n}{\mathrm{d}x} G_n \quad \text{and} \quad W_n = \frac{1}{\ell}\frac{\partial \hat{P}_n}{\partial s} G_n, \tag{6.9}$$

where the function G_n satisfies

$$\frac{\mathrm{i}}{n\alpha^2\bar{h}^2}\frac{\partial^2 G_n}{\partial \eta^2} + G_n = 1, \tag{6.10}$$

as follows from (6.4) and (6.5). Integrating (6.10) with the no-slip condition $G = 0$ at $\eta = (0,1)$ yields

$$G_n(x,\eta,s) = 1 - \frac{\cosh\left[\frac{\sqrt{n}\alpha\bar{h}}{2}\frac{1+\mathrm{i}}{\sqrt{2}}(2\eta-1)\right]}{\cosh\left[\frac{\sqrt{n}\alpha\bar{h}}{2}\frac{1+\mathrm{i}}{\sqrt{2}}\right]}. \tag{6.11}$$

The transverse velocity v_0 can be expressed using (6.3) in terms of the axial and azimuthal velocity components, yielding

$$\begin{aligned} V_n = -\frac{1}{\ell}\frac{\partial}{\partial x}\left(\ell \frac{\mathrm{d}P'_n}{\mathrm{d}x}\bar{h}\int_0^\eta G_n \mathrm{d}\eta\right) \quad &- \quad \frac{1}{\ell}\frac{\partial}{\partial s}\left(\frac{1}{\ell}\frac{\partial \hat{P}_n}{\partial s}\bar{h}\int_0^\eta G_n \mathrm{d}\eta\right) \\ &+ \quad \frac{\partial \bar{h}}{\partial x}\frac{\mathrm{d}P'_n}{\mathrm{d}x}\eta G_n + \frac{1}{\ell}\frac{\partial \bar{h}}{\partial s}\frac{1}{\ell}\frac{\partial \hat{P}_n}{\partial s}\eta G_n \end{aligned} \tag{6.12}$$

upon integration in η with the boundary condition $v_0 = 0$ at $\eta = 0$. Evaluating this expression at $\eta = 1$, where $V_n = H'_n$ (as follows from the boundary condition $v_0 = \partial h'_0/\partial t$), and using (6.8) yields

$$\gamma(1 + n^2k^2P'_n) + \frac{1}{\ell}\frac{\partial}{\partial x}\left(\ell\frac{\mathrm{d}P'_n}{\mathrm{d}x}q_n\right) + \frac{1}{\ell}\frac{\partial}{\partial s}\left[\frac{1}{\ell}\frac{\partial \hat{P}_n}{\partial s}q_n\right] = 0, \tag{6.13}$$

with

$$q_n(x,s) = \bar{h}\int_0^1 G_n \mathrm{d}\eta = \bar{h} - \frac{\sqrt{2}(1-\mathrm{i})}{\sqrt{n}\alpha}\tanh\left(\frac{\sqrt{n}\alpha\bar{h}}{2}\frac{1+\mathrm{i}}{\sqrt{2}}\right). \tag{6.14}$$

The pressure distribution can be determined by additional integrations of (6.13). Thus, integrating in s with the condition $\partial \hat{P}_n/\partial s = 0$ at $s = 0$, consistent with the symmetry condition $w_0 = 0$ at

$s=0$, yields

$$\frac{q_n}{\ell^2}\frac{\partial \hat{P}_n}{\partial s}+\frac{1}{\ell}\frac{\partial}{\partial x}\left[\ell\int_0^s q_n \mathrm{d}\tilde{s}\frac{\mathrm{d}P_n'}{\mathrm{d}x}\right]+\left(\int_0^s \gamma \mathrm{d}\tilde{s}\right)(n^2k^2P_n'+1)=0. \tag{6.15}$$

Evaluating the last equation at $s=1$, where $\partial\hat{P}_n/\partial s=0$, finally yields the problem

$$\frac{1}{\ell}\frac{\mathrm{d}}{\mathrm{d}x}\left[\ell Q_n\frac{\mathrm{d}P_n'}{\mathrm{d}x}\right]+\left(\int_0^1 \gamma \mathrm{d}s\right)(n^2k^2P_n'+1)=0;\begin{cases} P_n'=0 & \text{at} \quad x=0 \\ \frac{\mathrm{d}P_n'}{\mathrm{d}x}=0 & \text{at} \quad x=1\end{cases}, \tag{6.16}$$

involving the average section compliance $\int_0^1 \gamma \mathrm{d}s$ and the volume-flux function

$$Q_n(x)=\int_0^1 q_n\mathrm{d}s=\int_0^1\left[\bar{h}-\frac{\sqrt{2}(1-\mathrm{i})}{\sqrt{n}\alpha}\tanh\left(\frac{\sqrt{n}\alpha\bar{h}}{2}\frac{1+\mathrm{i}}{\sqrt{2}}\right)\right]\mathrm{d}s. \tag{6.17}$$

For given values of $\gamma(x,s)$, $\bar{h}(x,s)$, and $\ell(x)$ the integration of (6.16) determines $P_n'(x)$, which can be used to evaluate H_n' and U_n with use made of (6.8) and (6.9), while the associated azimuthal pressure gradient $\partial\hat{P}_n/\partial s$, determined from (6.15), is needed to evaluate the functions W_n and V_n from (6.9) and (6.12), thereby completing the description of the periodic solution (6.7). The axial velocity can be used to evaluate the volume flux crossing a given canal section x at a given time t according to

$$Q(x,t)=\ell\int_0^1\bar{h}\left(\int_0^1 u_0\mathrm{d}\eta\right)\mathrm{d}s=\ell\,\mathrm{Re}\left(\mathrm{i}\sum_{n=1}^{\infty}a_n n\,\mathrm{e}^{\mathrm{i}nt}\frac{\mathrm{d}P_n'}{\mathrm{d}x}Q_n\right). \tag{6.18}$$

The solution simplifies when the average section compliance and the shape of the canal section are independent of x, so that $\int_0^1\gamma\mathrm{d}s=1$, $\ell=1$, and $Q_n=$ constant. In that case, integration of (6.16) yields

$$P_n'=\frac{1}{n^2k^2}\left\{\frac{\cos[nk(1-x)/\sqrt{Q}]}{\cos(nk/\sqrt{Q})}-1\right\}. \tag{6.19}$$

6.1.2 Steady Streaming

Similar to chapter 2, the periodic first-order corrections to the velocity contain steady components that can be evaluated from

$$\begin{aligned}
\frac{\langle u_1\rangle}{\bar{h}^2\alpha^2} &= -\frac{\mathrm{d}\langle p_1'\rangle}{\mathrm{d}x}\frac{(1-\eta)\eta}{2}+\eta\int_0^\eta \mathcal{F}_x \mathrm{d}\bar{\eta}-\int_0^\eta \mathcal{F}_x\bar{\eta}\mathrm{d}\bar{\eta}-\eta\int_0^1 \mathcal{F}_x(1-\eta)\mathrm{d}\eta && (6.20)\\
\frac{\langle w_1\rangle}{\bar{h}^2\alpha^2} &= -\frac{1}{\ell}\frac{\partial\langle\hat{p}_1\rangle}{\partial s}\frac{(1-\eta)\eta}{2}+\eta\int_0^\eta \mathcal{F}_s \mathrm{d}\bar{\eta}-\int_0^\eta \mathcal{F}_s\bar{\eta}\mathrm{d}\bar{\eta}-\eta\int_0^1 \mathcal{F}_s(1-\eta)\mathrm{d}\eta && (6.21)\\
\langle v_1\rangle &= -\frac{1}{\ell}\frac{\partial}{\partial x}\left[\ell\int_0^\eta\left(\bar{h}\langle u_1\rangle+\langle h_0' u_0\rangle\right)\mathrm{d}\eta\right]+\eta\frac{\partial\bar{h}}{\partial x}\langle u_1\rangle+\eta\left\langle u_0\frac{\partial h_0'}{\partial x}\right\rangle\\
&- \frac{1}{\ell}\frac{\partial}{\partial s}\left[\int_0^\eta\left(\bar{h}\langle w_1\rangle+\langle h_0' w_0\rangle\right)\mathrm{d}\eta\right]+\eta\frac{1}{\ell}\frac{\partial\bar{h}}{\partial s}\langle w_1\rangle+\eta\left\langle w_0\frac{1}{\ell}\frac{\partial h_0'}{\partial s}\right\rangle. && (6.22)
\end{aligned}$$

with

$$\begin{aligned}
\mathcal{F}_x &= \frac{1}{\ell}\frac{\partial}{\partial x}(\ell\langle u_0^2\rangle)+\frac{1}{\bar{h}}\frac{\partial}{\partial\eta}\langle u_0v_0\rangle+\frac{1}{\ell}\frac{\partial}{\partial s}\langle u_0w_0\rangle\\
&- \frac{\eta}{\bar{h}}\frac{\partial}{\partial\eta}\langle\frac{\partial h_0'}{\partial t}u_0\rangle-\frac{\partial\bar{h}}{\partial x}\frac{\eta}{\bar{h}}\frac{\partial}{\partial\eta}\langle u_0^2\rangle-\frac{1}{\ell}\frac{\partial\bar{h}}{\partial s}\frac{\eta}{\bar{h}}\frac{\partial}{\partial\eta}\langle u_0w_0\rangle+\frac{2}{\bar{h}^3\alpha^2}\frac{\partial^2}{\partial\eta^2}\langle h_0'u_0\rangle && (6.23)
\end{aligned}$$

and

$$\begin{aligned}
\mathcal{F}_s &= \frac{\partial}{\partial x}\langle u_0w_0\rangle+2\frac{\langle u_0w_0\rangle}{\ell}\frac{\partial\ell}{\partial x}+\frac{1}{\bar{h}}\frac{\partial}{\partial\eta}\langle v_0w_0\rangle+\frac{1}{\ell}\frac{\partial}{\partial s}\langle w_0^2\rangle-\frac{\eta}{\bar{h}}\frac{\partial}{\partial\eta}\langle\frac{\partial h_0'}{\partial t}w_0\rangle\\
&- \frac{\partial\bar{h}}{\partial x}\frac{\eta}{\bar{h}}\frac{\partial}{\partial\eta}\langle u_0w_0\rangle-\frac{1}{\ell}\frac{\partial\bar{h}}{\partial s}\frac{\eta}{\bar{h}}\frac{\partial}{\partial\eta}\langle w_0^2\rangle+\frac{2}{\bar{h}^3\alpha^2}\frac{\partial^2}{\partial\eta^2}\langle h_0'w_0\rangle. && (6.24)
\end{aligned}$$

The average streamwise pressure gradient $\mathrm{d}\langle p_1'\rangle/\mathrm{d}x$ is obtained from the continuity condition

$$\int_0^1\bar{h}\left(\int_0^1\langle u_1\rangle\mathrm{d}\eta\right)\mathrm{d}s+\int_0^1\int_0^1\langle h_0'u_0\rangle\mathrm{d}\eta\mathrm{d}s=0, \qquad (6.25)$$

with $\partial\langle\hat{p}_1\rangle/\partial s$ similarly obtained in terms of $\mathrm{d}\langle p_1'\rangle/\mathrm{d}x$ by use of

$$\bar{h}\int_0^1 \langle w_1\rangle \mathrm{d}\eta + \int_0^1 \langle h_0' w_0\rangle \mathrm{d}\eta = -\frac{\partial}{\partial x}\left[\ell \int_0^s \left(\bar{h}\int_0^1 \langle u_1\rangle \mathrm{d}\eta + \int_0^1 \langle h_0' u_0\rangle \mathrm{d}\eta\right)\mathrm{d}s\right]. \tag{6.26}$$

The computation of the time averages in the above expressions, involving products of the Fourier expansions defined in (6.7), is facilitated by noting that products of functions belonging to different modes yield a zero time average. Further use of the identities $\langle \mathrm{Re}(\mathrm{i}e^{\mathrm{i}nt}A)\,\mathrm{Re}(\mathrm{i}e^{\mathrm{i}nt}B)\rangle = \mathrm{Re}(AB^*)/2$ and $\langle \mathrm{Re}(e^{\mathrm{i}nt}A)\,\mathrm{Re}(\mathrm{i}e^{\mathrm{i}nt}B)\rangle = \mathrm{Re}(\mathrm{i}A^*B)/2$, which apply to any generic time-independent complex functions A and B, with the asterisk $*$ denoting complex conjugates, provides

$$\mathcal{F}_x = \frac{1}{2}\sum_{n=1}^{\infty} |a_n|^2 n^2\,\mathrm{Re}\left(\mathcal{F}_{x,n}\right) \quad \text{and} \quad \mathcal{F}_s = \frac{1}{2}\sum_{n=1}^{\infty} |a_n|^2 n^2\,\mathrm{Re}\left(\mathcal{F}_{s,n}\right) \tag{6.27}$$

with

$$\begin{aligned} \mathcal{F}_{x,n} \;=\;& \frac{1}{\ell}\frac{\partial}{\partial x}(\ell|U_n|^2) + \frac{1}{\bar{h}}\frac{\partial}{\partial\eta}(U_n V_n^*) + \frac{1}{\ell}\frac{\partial}{\partial s}(U_n W_n^*) - \frac{\eta}{\bar{h}}\frac{\partial}{\partial\eta}(U_n H_n'^*) \\ -\;& \frac{\partial\bar{h}}{\partial x}\frac{\eta}{\bar{h}}\frac{\partial}{\partial\eta}|U_n|^2 - \frac{1}{\ell}\frac{\partial\bar{h}}{\partial s}\frac{\eta}{\bar{h}}\frac{\partial}{\partial\eta}(U_n W_n^*) + \frac{2}{\bar{h}^3 n\alpha^2}\frac{\partial^2}{\partial\eta^2}(\mathrm{i}U_n H_n'^*) \end{aligned} \tag{6.28}$$

and

$$\begin{aligned} \mathcal{F}_{s,n} \;=\;& \frac{\partial}{\partial x}(W_n U_n^*) + 2\frac{(W_n U_n^*)}{\ell}\frac{\partial\ell}{\partial x} + \frac{1}{\bar{h}}\frac{\partial}{\partial\eta}(W_n V_n^*) + \frac{1}{\ell}\frac{\partial}{\partial s}|W_n|^2 - \frac{\eta}{\bar{h}}\frac{\partial}{\partial\eta}(W_n H_n'^*) \\ -\;& \frac{\partial\bar{h}}{\partial x}\frac{\eta}{\bar{h}}\frac{\partial}{\partial\eta}(W_n U_n^*) - \frac{1}{\ell}\frac{\partial\bar{h}}{\partial s}\frac{\eta}{\bar{h}}\frac{\partial}{\partial\eta}|W_n|^2 + \frac{2}{\bar{h}^3 n\alpha^2}\frac{\partial^2}{\partial\eta^2}(\mathrm{i}W_n H_n'^*), \end{aligned} \tag{6.29}$$

Similarly, the time averages $\langle h_0' u_0\rangle$ and $\langle h_0' w_0\rangle$ appearing in (6.25) and (6.26) can be computed from the expressions

$$\langle h_0' u_0\rangle = \frac{1}{2}\sum_{n=1}^{\infty} |a_n|^2 n \,\mathrm{Re}\left(\mathrm{i} H_n'^{*} U_n\right) \quad \text{and} \quad \langle h_0' w_0\rangle = \frac{1}{2}\sum_{n=1}^{\infty} |a_n|^2 n \,\mathrm{Re}\left(\mathrm{i} H_n'^{*} W_n\right). \tag{6.30}$$

6.1.3 Stokes Drift

The Lagrangian velocity components are computed according to $u_{\mathrm{L}} = \langle u_1\rangle + u_{\mathrm{SD}}$, $v_{\mathrm{L}} = \langle v_1\rangle + v_{\mathrm{SD}}$, and $w_{\mathrm{L}} = \langle w_1\rangle + w_{\mathrm{SD}}$, where the Stokes-drift velocities are given by

$$\begin{aligned}
u_{\mathrm{SD}} &= \frac{1}{\bar{h}}\left\{\langle u_0 h_0'\rangle + \frac{1}{\ell}\frac{\partial}{\partial s}\left(\bar{h}\left\langle u_0 \int w_0 \mathrm{d}t\right\rangle\right)\right\} \\
&+ \frac{1}{\bar{h}}\frac{\partial}{\partial \eta}\left\langle u_0\left[\int v_0 \mathrm{d}t - \eta\left(h_0' + \frac{1}{\ell}\frac{\partial \bar{h}}{\partial s}\int w_0 \mathrm{d}t\right)\right]\right\rangle, && (6.31)\\
v_{\mathrm{SD}} &= \frac{1}{\ell}\frac{\partial}{\partial x}\left(\ell\left\langle v_0 \int u_0 \mathrm{d}t\right\rangle\right) + \frac{1}{\ell}\frac{\partial}{\partial s}\left\langle v_0 \int w_0 \mathrm{d}t\right\rangle \\
&- \frac{\eta}{\bar{h}}\frac{\partial}{\partial \eta}\left\langle v_0\left(h_0' + \frac{\partial \bar{h}}{\partial x}\int u_0 \mathrm{d}t + \frac{1}{\ell}\frac{\partial \bar{h}}{\partial s}\int w_0 \mathrm{d}t\right)\right\rangle && (6.32)\\
w_{\mathrm{SD}} &= \frac{1}{\bar{h}}\left[\langle w_0 h_0'\rangle + \frac{\partial}{\partial x}\left(\bar{h}\left\langle w_0 \int u_0 \mathrm{d}t\right\rangle\right)\right] \\
&+ \frac{1}{\bar{h}}\frac{\partial}{\partial \eta}\left\langle w_0\left[\int v_0 \mathrm{d}t - \eta\left(h_0' + \frac{\partial \bar{h}}{\partial x}\int u_0 \mathrm{d}t\right)\right]\right\rangle. && (6.33)
\end{aligned}$$

The above considerations pertaining to time averages of products of Fourier expansions also apply in this case, thereby yielding the simplified expressions

$$(u_{\mathrm{SD}}, v_{\mathrm{SD}}, w_{\mathrm{SD}}) = \frac{1}{2}\sum_{n=1}^{\infty} |a_n|^2 n \,\mathrm{Re}\left[\mathrm{i}\left(\mathcal{U}_n, \mathcal{V}_n, \mathcal{W}_n\right)\right], \tag{6.34}$$

where

$$
\begin{aligned}
\mathcal{U}_n &= \frac{1}{\bar{h}}\left[U_n H_n'^{*} + \frac{1}{\ell}\frac{\partial}{\partial s}\left(\bar{h}U_n W_n^{*}\right)\right] + \frac{1}{\bar{h}}\frac{\partial}{\partial \eta}\left\{U_n\left[V_n^{*} - \eta\left(H_n'^{*} + \frac{1}{\ell}\frac{\partial \bar{h}}{\partial s}W_n^{*}\right)\right]\right\}, \\
\mathcal{V}_n &= \frac{1}{\ell}\frac{\partial}{\partial x}\left(\ell V_n U_n^{*}\right) + \frac{1}{\ell}\frac{\partial}{\partial s}\left(V_n W_n^{*}\right) - \frac{\eta}{\bar{h}}\frac{\partial}{\partial \eta}\left[V_n\left(H_n'^{*} + \frac{\partial \bar{h}}{\partial x}U_n^{*} + \frac{1}{\ell}\frac{\partial \bar{h}}{\partial s}W_n^{*}\right)\right], \\
\mathcal{W}_n &= \frac{1}{\bar{h}}\left[W_n H_n'^{*} + \frac{\partial}{\partial x}\left(\bar{h}W_n U_n^{*}\right)\right] + \frac{1}{\bar{h}}\frac{\partial}{\partial \eta}\left\{W_n\left[V_n^{*} - \eta\left(H_n'^{*} + \frac{\partial \bar{h}}{\partial x}U_n^{*}\right)\right]\right\}.
\end{aligned}
\tag{6.35}
$$

6.1.4 Suggested Work

The flow and transport calculations described in the main text could all be modified for a general pressure signal following the equations listed above. It is suggested that the flow and transport are investigated for a simple three-peak model, which is a more accurate model of intracranial pressure in a healthy individual. This should only require three Fourier modes, so it should not be significantly more computationally intensive. Additionally, a detailed model of the intracranial pressure using many more modes could also be studied, although it may be more computationally expensive. The resulting velocity fields and concentration distributions should be compared to those found using a simple intracranial pressure, and any differences should be investigated thoroughly.

Furthermore, MRI data similar to that found in [13], could be obtained for the CSF flow at several locations along the canal. Since MRI measurements are typically gated to the cardiac cycle, the simple three-peak intracranial pressure model will be sufficient to model the real results obtained from cardiac-gated MRI, as this signal behavior is caused by the cardiac cycle. The is an additional lower-frequency modulation due to respiration could also be investigated by using respiratory-gated measurements.

6.2 Respiratory-driven Flow in the Spinal Canal

So far we have analyzed cerebrospinal fluid motion due to intracranial pressure variations. However, many have shown that deep breathing [20] and coughing [92] influence CSF motion. The respiratory cycle, as well as respiratory events such as coughing, affect the pressure in the veins surrounding the spinal canal which, due to their close contact with the spinal canal, influence the local pressure everywhere along the canal [47].

6.2.1 Changes to the Leading-Order Equations

The analysis presented here is nearly the same as chapter 2 with any changes described below.

The venous pressure p_v is defined as

$$p_v(x,t) = p_0 - f(x)\Pi_v(t) \tag{6.36}$$

where p_0 is the constant background pressure in the veins, $f(x)$ is a function that describes the variation with the lengthwise coordinate x, and $\Pi_v(t)$ is a periodic function (e.g. $\Delta p_v \cos \omega t$, where Δp_v is a constant) that describes the variation with time. Note that $p_v(x,t) - p_0$ has been assumed to be separable.

The perturbation of the canal width h' given by $\varepsilon h' = h - \bar{h}$ is related to the pressure by

$$h'(x,s,t) = \gamma(p - p_v) = \gamma\left(k^2 p' + f(x)\Pi_v(t)\right). \tag{6.37}$$

The analysis proceeds in the same manner as section 2.2.1 with these new conditions and begins to differ when continuity is enforced. P' must satisfy

$$\frac{\mathrm{d}}{\mathrm{d}x}\left[\tilde{Q}(x)\frac{\mathrm{d}P'}{\mathrm{d}x}\right] + l\left(\int_0^1 \gamma \mathrm{d}s\right)\left(k^2 P' + f(x)\right) = 0 \tag{6.38}$$

where

$$\tilde{Q}(x) = l(x)Q(x) = l(x)\int_0^1 \bar{h}(x,s)\int_0^1 G(x,\eta,s)\ \mathrm{d}\eta\mathrm{d}s \tag{6.39}$$

is a function which describes the volume flux of CSF, which is given by

$$\dot{V}_{CSF}(x,t) = \mathrm{Re}\left[\mathrm{i}e^{\mathrm{i}t}\frac{\mathrm{d}P'}{\mathrm{d}x}\tilde{Q}(x)\right]. \tag{6.40}$$

The boundary condition at $x = 1$ is simply $\frac{\mathrm{d}P'}{\mathrm{d}x} = 0$ as before, which enforces zero flux at the closed end. However, the boundary condition at $x = 0$ is now more complicated. In the previous analysis, the boundary condition at $x = 0$ was $P' = 0$ to indicate that the pressure at the entrance of the canal was equal to the intracranial pressure. Now only the venous pressure along the canal is being taken into account. We start with a conservation equation in the cranial cavity from the Monro-Kellie doctrine [56], assuming the brain volume is constant in time, which gives

$$\dot{V}_a = \dot{V}_v + \dot{V}_{CSF} \tag{6.41}$$

where $\dot{V}_a$ is the volume flux of arterial blood into the cranial cavity and $\dot{V}_v$ is the volume flux of the venous blood out of the cranial cavity, measured at the foramen magnum. Note that these volume fluxes are all defined such that they are, on average, positive. The venous blood flow rate is assumed to be linear with the pressure difference between the cranial cavity and the veins. Therefore, it is written as

$$\dot{V}_v = \beta_c\left(\frac{\mathrm{d}p_c}{\mathrm{d}t} - \frac{\mathrm{d}p_v}{\mathrm{d}t}\right) \tag{6.42}$$

where β_c is a constant that describes the compliance of the cranial vault as it responds to pressure changes. This has been nondimensionalized such that β_c is expected to be of order unity.

Since only the respiratory effects are of interest here, we set $\dot{V}_a = 0$. Then, by combining

(6.40), (6.41), and (6.42) we obtain

$$\left.\frac{\mathrm{d}P'}{\mathrm{d}x}\right|_0 \tilde{Q}(0) + \beta_c\left[k^2 P'(0) + f(0)\right] = 0 \tag{6.43}$$

which has been evaluated at $x = 0$ since the volume conservation is only valid at that location. For clarity, the equation and boundary conditions are all repeated here. The equation to be solved is

$$\frac{\mathrm{d}}{\mathrm{d}x}\left[\tilde{Q}(x)\frac{\mathrm{d}P'}{\mathrm{d}x}\right] + l\left(\int_0^1 \gamma \mathrm{d}s\right)\left(k^2 P' + f(x)\right) = 0 \tag{6.44}$$

with boundary conditions

$$\begin{cases} \frac{\mathrm{d}P'}{\mathrm{d}x}\tilde{Q}(x) + \beta_c\left[k^2 P'(x) + f(x)\right] = 0, & x = 0; \\ \frac{\mathrm{d}P'}{\mathrm{d}x} = 0, & x = 1. \end{cases} \tag{6.45}$$

The above can be solved numerically for any $l(x)$, $\gamma(x,s)$, $\bar{h}(x,s)$.

However, for $l(x) = \gamma(x) = 1$ and $\bar{h}(x,s) = \bar{h}(s)$ such that $\tilde{Q}$ is constant, P' is found analytically to be

$$P'(x) = A\cos(\mu x) + B\sin(\mu x) - \frac{\sin(\mu x)}{\mu\tilde{Q}}\int_1^x f(\xi)\cos(\mu\xi)\mathrm{d}\xi + \frac{\cos(\mu x)}{\mu\tilde{Q}}\int_1^x f(\xi)\sin(\mu\xi)\mathrm{d}\xi \tag{6.46}$$

where

$$A = \frac{\beta_c\mu\int_0^1 f(\xi)\sin(\mu\xi)\mathrm{d}\xi - \int_0^1 f(\xi)\cos(\mu\xi)\mathrm{d}\xi - \beta_c f(0)}{\mu\tan(\mu)\tilde{Q} + \beta_c k^2}, \tag{6.47}$$

$$B = A\tan(\mu) = \frac{\beta_c\mu\int_0^1 f(\xi)\sin(\mu\xi)\mathrm{d}\xi - \int_0^1 f(\xi)\cos(\mu\xi)\mathrm{d}\xi - \beta_c f(0)}{\mu\tilde{Q} + \beta_c k^2\cot(\mu)}, \tag{6.48}$$

$$\mu = \frac{k}{\sqrt{\tilde{Q}}}, \tag{6.49}$$

where ξ is a dummy integration variable. The subsequent analysis of the Lagrangian velocity field is identical to the previous paper, except that h' and p' have changed.

6.2.2 Suggested Work

The flow and transport calculations described in the main text could all be modified to instead analyze the effect of pressure variations along the canal. It is suggested that the flow and transport are studied for several simple functions $f(x)$, as well as a more detailed model describing the pressure variations along the canal due to venous blood pressure changes.

It is also recommended that respiratory-gated MRI measurements of CSF flow are obtained for at several locations along the canal. By measuring the local CSF flow, as well as the arterial and venous blood flow across the foramen magnum, one could estimate the overall cranial compliance β_c and the function describing the local pressure variation due to veins $f(x)$.

6.3 Transport of Particles in the Spinal Canal

The velocities and transport equations described in chapters 2–4 can effectively describe small, light particles or dissolved fluids which will perfectly follow the fluid motion, such as the radioactive tracers used in early experiments to study CSF motion [17]. However, larger or heavier particles have an increased inertia which may lead to trajectories which do not perfectly track the fluid motion. Biological macromolecules as well as liposome particles containing drugs are both active research areas in intrathecal drug delivery which can possibly be large enough for their inertia to affect their trajectory [31, 78]. The same model and expressions for the Eulerian velocities in chapter 2 are used here to calculate trajectories of inertial particles.

6.3.1 Governing Equations

From Newton's Second Law, we can write

$$m\frac{\mathrm{d}^2\mathbf{x}_p}{\mathrm{d}t^2} = -3\pi\mu d_p\left(\frac{\mathrm{d}\mathbf{x}_p}{\mathrm{d}t} - \mathbf{v}\right) \tag{6.50}$$

where m is the mass of the particle, $\mathbf{x}_p$ is the location of the particle, μ is the viscosity of the fluid, d_p is the diameter of the particle, and $\mathbf{v}$ is the fluid velocity. It is assumed that the particles are spherical and that the only body force is drag. Additional body forces, such as magnetic or gravitational forces, could also be added here.

This equation can be nondimensionalized with the scales used in chapter 2 to yield

$$\mathrm{St}\frac{\mathrm{d}^2\mathbf{x}_p}{\mathrm{d}t^2} = -\left(\frac{\mathrm{d}\mathbf{x}_p}{\mathrm{d}t} - \varepsilon\mathbf{v}\right) \tag{6.51}$$

where the Stokes number takes the form

$$\mathrm{St} = \frac{\rho_p d_p^2/(18\mu)}{\omega^{-1}} \tag{6.52}$$

where ρ_p is the particle density and ω is the frequency of the leading order pulsatile flow. The Stokes number represents the comparison between the relaxation time of the drag ($\rho_p d_p^2/(18\mu)$) and the time scale related to the fluid flow (ω^{-1}). A large Stokes number corresponds to a large or heavy particle, which will tend to continue along its current path, while a small Stokes number corresponds to a light or small particle, which will tend to follow the fluid motion. For $\mathrm{St} \to 0$, the previously found fluid-particle trajectories (2.38) are obtained. This system of second-order ordinary differential equations may be solved for using a time-advancing numerical scheme. As in the main text, it is recommended to introduce a moving coordinate $\eta = y/h(x,\theta,t)$ so that the boundary conditions are constant in time.

Although (6.51) can be solved directly for $\mathbf{x}_p$ in terms of t, we can again introduce a second time variable $\tau = \varepsilon^2 t$, along with the expansions

$$\mathbf{x}_p(t,\tau) = \mathbf{x}_{p0}(t,\tau) + \varepsilon \mathbf{x}_{p1}(t,\tau) + \varepsilon^2 \mathbf{x}_{p2}(t,\tau) + \ldots \tag{6.53}$$

$$\mathbf{v} = \mathbf{v}_0 + \varepsilon[\mathbf{v}_1(\mathbf{x}_{p0},t) + \mathbf{x}_{p1} \cdot \nabla \mathbf{v}_1(\mathbf{x}_{p0},t)], \tag{6.54}$$

to describe the slow motion of a particle. All periodic motion with zero mean over a cycle of 2π is assumed to follow the short time scale t and all other motion is carried by the dependence on τ. Thus, (6.53) and (6.54) can be substituted in to (6.51) and evaluated at each order of the small parameter ε. At $O(1)$, (6.51) becomes

$$\mathrm{St}\frac{\partial^2 \mathbf{x}_{p0}}{\partial t^2} = \frac{\partial \mathbf{x}_{p0}}{\partial t} \tag{6.55}$$

which implies $\mathbf{x}_{p0}$ must be a function of τ only because the motion in t must be periodic. Therefore, $\mathbf{x}_{p0} = c_1(\tau)$.

At $O(\varepsilon)$, (6.51) becomes

$$\mathrm{St}\frac{\partial^2 \mathbf{x}_{p1}}{\partial t^2} = \frac{\partial \mathbf{x}_{p1}}{\partial t} + \mathbf{v}_0 \tag{6.56}$$

which can be integrated to give

$$\mathbf{x}_{p1} = c_3(\tau) + \int^t \mathrm{Re}\left[\frac{i e^{it} \mathbf{V}}{1 + i\mathrm{St}}\right] \mathrm{d}t, \tag{6.57}$$

upon substitution of the known oscillatory velocity components, where the dependence on the Stokes number is clearly found.

Finally, at $O(\varepsilon^2)$, the equation becomes

$$\mathrm{St}\frac{\partial^2 \mathbf{x}_{p2}}{\partial t^2} = -\frac{\partial \mathbf{x}_{p0}}{\partial \tau} - \frac{\partial \mathbf{x}_{p2}}{\partial t} + \varepsilon \mathbf{v}_1 + \mathbf{x}_{p1} \cdot \nabla \mathbf{v}_0 \tag{6.58}$$

which can then be time averaged, using the notation $\langle\cdot\rangle = \int_t^{t+2\pi} \cdot \mathrm{d}t$, to give

$$\frac{\partial \mathbf{x}_{p0}}{\partial \tau} = \langle \mathbf{v}_1 \rangle + \langle \mathbf{x}_{p1} \cdot \nabla \mathbf{v}_0 \rangle \tag{6.59}$$

and therefore the short time scale t is eliminated from the problem and we have an equation only in terms of the long time scale τ. Note that this is the same equation for the long-time behavior of a fluid-particle trajectory found in section 3; however, x_{p1} now carries the dependence on the Stokes number. Thus, the change in the long-term behavior of inertial particles, as compared to fluid particles, is caused solely by Stokes drift.

6.3.2 Suggested Work

It is suggested that these equations in τ are solved and compared to the original, full solution in the small time scale t, thus validating the two-time scale analysis. It is expected that calculation of a trajectory in τ is much faster than an equivalent amount of time in t. It is also suggested that these results are compared to those for fluid-particle motion with little diffusion, the $1 \ll S \ll \varepsilon^{-2}$ case. Perhaps larger particles will have enough inertia to escape the Lagrangian vortices found in the variable eccentricity case. Finally, it is suggested that this problem is expanded for other types of body forces such as gravitational and magnetic.

Bibliography

[1] ACKERMAN, M. J. The visible human project. *Proceedings of the IEEE 86*, 3 (1998), 504–511.

[2] BARKER, A. E. Clinical experiences with spinal analgesia in 100 cases. *The British Medical Journal 1*, 2412 (1907), 665–674.

[3] BHADELIA, R. A., BOGDAN, A. R., KAPLAN, R. F., AND WOLPERT, S. M. Cerebrospinal fluid pulsation amplitude and its quantitative relationship to cerebral blood flow pulsations: a phase-contrast MR flow imaging study. *Neuroradiology 39*, 4 (Apr 1997), 258–264.

[4] BLASBERG, R., PATLAK, C., AND FENSTERMACHER, J. Intrathecal chemotherapy: brain tissue profiles after ventriculocisternal perfusion. *Journal of Pharmacology and Experimental Therapeutics 195*, 1 (1975), 73–83.

[5] BLOOMFIELD, I. G., JOHNSTON, I. H., AND E., B. L. Effects of proteins, blood cells and glucose on the viscosity of cerebrospinal fluid. *Pediatric Neurosurgery 28*, 5 (1998), 246–251.

[6] BORHANI, N., NELISSEN, R. M., AND BUCHSER, E. Fluid dynamics of drug spread in the intrathecal space. Neurohydrodynamics Working Group Meeting, 2011.

[7] BOTTROS, M. M., AND CHRISTO, P. J. Current perspectives on intrathecal drug delivery. *Journal of Pain Research 7* (2014), 615–626.

[8] BOULTON, M., FLESSNER, M., ARMSTRONG, D., MOHAMED, R., HAY, J., AND JOHNSTON, M. Contribution of extracranial lymphatics and arachnoid villi to the clearance of a CSF tracer in the rat. *American Journal of Physiology-Regulatory, Integrative and Comparative Physiology 276*, 3 Pt 2 (Mar 1999), R818–823.

[9] BUCHSER, E., DURRER, A., CHDEL, D., AND MUSTAKI, J. Efficacy of intrathecal bupivacaine: How important is the flow rate? *Pain Medicine 5* (2004), 248–252.

[10] CARPENTER, P. W., BERKOUK, K., AND LUCEY, A. D. Pressure wave propagation in fluid-filled co-axial elastic tubes part 2: Mechanisms for the pathogenesis of syringomyelia. *Journal of Biomechanical Engineering 125*, 6 (2003), 857–863.

[11] CHIKLY, B. Is human CSF reabsorbed by lymph? Lymph drainage therapy and manual drainage of the central nervous system. *American Academy of Osteopathy 8*, 2 (1998), 28–34.

[12] COENEN, W. Steady streaming around a cylinder pair. *Proceedings of the Royal Society 472*, 2195 (2016).

[13] COENEN, W., GUTIÉRREZ-MONTES, C., SINCOMB, S., CRIADO-HIDALGO, E., WEI, K., KING, K., HAUGHTON, V., MARTÍNEZ-BAZÁN, C., SÁNCHEZ, A., AND LASHERAS, J. C. Subject-specific studies of CSF bulk flow patterns in the spinal canal: Implications for the dispersion of solute particles in intrathecal drug delivery. *American Journal of Neuroradiology 40*, 7 (2019), 1242–1249.

[14] CROWDY, D. G. Uniform flow past a periodic array of cylinders. *European Journal of Mechanics-B/Fluids 56* (2016), 120–129.

[15] CUTLER, R. W., PAGE, L., GALICICH, J., AND WATTERS, G. V. Formation and absorption of cerebrospinal fluid in man. *Brain 91*, 4 (1968), 707–720.

[16] DAVSON, H. Formation and drainage of the cerebrospinal fluid. *The Scientific Basis of Medicine. Annual Reviews* (1966), 238–259.

[17] DI CHIRO, G. Movement of the cerebrospinal fluid in human beings. *Nature 204* (1964), 290–291.

[18] DI CHIRO, G. Observations on the circulation of the cerebrospinal fluid. *Acta Radiologica: Diagnosis 5* (1966), 988–1002.

[19] DI CHIRO, G., LARSON, S. M., HARRINGTON, T., JOHNSTON, G. S., GREEN, M. V., AND SWANN, S. J. Descent of cerebrospinal fluid to spinal subarachnoid space. *Acta Radiologica: Diagnosis 14*, 4 (1973), 379–384.

[20] DREHA-KULACZEWSKI, S., JOSEPH, A. A., MERBOLDT, K. D., LUDWIG, H. C., GÄRTNER, J., AND FRAHM, J. Inspiration is the major regulator of human CSF flow. *Journal of Neuroscience 35*, 6 (2015), 2485–2491.

[21] DU BOULAY, G. H. Pulsatile movements in the CSF pathways. *British Journal of Radiology 39* (1966), 255–262.

[22] GREITZ, D., FRANCK, A., AND NORDELL, B. On the pulsatile nature of intracranial and spinal CSF-circulation demonstrated by MR imaging. *Acta Radiologica 34*, 4 (1993), 321–328.

[23] GREITZ, D., AND HANNERZ, J. A proposed model of cerebrospinal fluid circulation: observations with radionuclide cisternography. *American Journal of Neuroradiology 17*, 3 (1996), 431–438.

[24] GROTBERG, J. B. Pulmonary flow and transport phenomena. *Annual Review of Fluid Mechanics 26*, 1 (1994), 529–571.

[25] HALLWORTH, S. P., FERNANDO, R., COLUMB, M. O., AND M., S. G. The effect of posture and baricity on the spread of intrathecal bupivacaine for elective cesarean delivery. *Anesthesia & Analgesia 100*, 4 (2005), 1159–1165.

[26] HETTIARACHCHI, H. D. M., HSU, Y., HARRIS, T. J., AND LINNINGER, A. A. The effect of pulsatile flow on intrathecal drug delivery in the spinal canal. *Annals of Biomedical Engineering 39*, 10 (2011), 2592.

[27] HOLTSMARK, J., JOHNSEN, I., SIKKELAND, T., AND SKAVLEM, S. Boundary layer flow near a cylindrical obstacle in an oscillating, incompressible fluid. *Journal of the Acoustical Society of America 26*, 1 (1954), 26–39.

[28] HOUSE, T. A., LIEU, V. H., AND SCHWARTZ, D. T. A model for inertial particle trapping locations in hydrodynamic tweezers arrays. *Journal of Micromechanics and Microengineering 24*, 4 (2014).

[29] HSU, Y., HETTIARACHCHI, H. D. M., ZHU, D. C., AND LINNINGER, A. A. The frequency and magnitude of cerebrospinal fluid pulsations influence intrathecal drug distribution: key factors for interpatient variability. *Anesthesia & Analgesia 115*, 2 (2012), 386–394.

[30] HYDON, P. E., AND PEDLEY, T. J. Axial dispersion in a channel with oscillating walls. *Journal of Fluid Mechanics 249* (1993), 535–555.

[31] ISHIDA, T., TAKANASHI, Y., AND KIWADA, H. Safe and efficient drug delivery system with liposomes for intrathecal application of an antivasospastic drug, fasudil. *Biological and Pharmaceutical Bulletin 29*, 3 (3 2006), 397–402.

[32] ISSA, R. I. Solution of the implicitly discretised fluid flow equations by operator-splitting. *Journal of Computational Physics 62*, 1 (1986), 40–65.

[33] JOHANSON, C. E., DUNCAN, J. A., KLINGE, P. M., BRINKER, T., STOPA, E. G., AND SILVERBERG, G. D. Multiplicity of cerebrospinal fluid functions: new challenges in health and disease. *Cerebrospinal Fluid Research 5*, 1 (2008), 10.

[34] KALATA, W., MARTIN, B. A., OSHINSKI, J. N., JEROSCH-HEROLD, M., ROYSTON, T. J., AND LOTH, F. MR measurement of cerebrospinal fluid velocity wave speed in the spinal canal. *IEEE Transactions on Biomedical Engineering 56*, 6 (2009), 1765–1768.

[35] KAMRAN, S., AND WRIGHT, B. D. Complications of intrathecal drug delivery systems. *Neuromodulation: Technology at the Neural Interface 4* (2001), 111–115.

[36] KAO, Y. H., GUO, W. Y., LIOU, A. J. K., HSIAO, Y. H., AND CHOU, C. C. The respiratory modulation of intracranial cerebrospinal fluid pulsation observed on dynamic echo planar images. *Magnetic Resonance Imaging 26*, 2 (2008), 198–205.

[37] KHANI, M., SASS, L. R., XING, T., SHARP, M. K., BALÉDENT, O., AND MARTIN, B. A. Anthropomorphic model of intrathecal cerebrospinal fluid dynamics within the spinal subarachnoid space: spinal cord nerve roots increase steady-streaming. *Journal of Biomechanical Engineering 140*, 8 (2018), 081012.

[38] KROIN, J. S., ALI, A., YORK, M., AND PENN, R. D. The distribution of medication along the spinal canal after chronic intrathecal administration. *Neurosurgery 33*, 2 (1993), 226–230.

[39] KURTCUOGLU, V. Computational fluid dynamics for the assessment of cerebrospinal fluid flow and its coupling with cerebral blood flow. In *Biomechanics of the Brain*, K. Miller, Ed. Springer, New York, 2011, pp. 169–188.

[40] LANZ, E., DÄUBLER, F., EISSNER, D., BROD, K. H., AND THEISS, D. Effect of spinal CSF dynamics on the subarachnoid diffusion of a substance applied close to the spinal cord. *Regional-Anaesthesie 9*, 1 (1986), 4–8.

[41] LARRIEU, E., HINCH, E. J., AND CHARRU, F. Lagrangian drift near a wavy boundary in a viscous oscillating flow. *Journal of Fluid Mechanics 630* (2009), 391–411.

[42] LAWRENCE, J. J., COENEN, W., SÁNCHEZ, A. L., PAWLAK, G., MARTÍNEZ-BAZÁN, C., HAUGHTON, V., AND C., L. J. On the dispersion of a drug delivered intrathecally in the spinal canal. *Journal of Fluid Mechanics 861* (2019), 679–720.

[43] LEE, Y. C., HSIEH, C. C., CHUANG, J. P., AND LI, C. Y. The necessity of intrathecal chemotherapy for the treatment of breast cancer patients with leptomeningeal metastasis: A systematic review and pooled analysis. *Current Problems in Cancer 41* (2017), 355–370.

[44] LEVY, L. M., AND DI CHIRO, G. MR phase imaging and cerebrospinal fluid flow in the head and spine. *Neuroradiology 32*, 5 (1990), 399–406.

[45] LIEU, V. H., HOUSE, T. A., AND SCHWARTZ, D. T. Hydrodynamic tweezers: impact of design geometry on flow and microparticle trapping. *Analytical Chemistry 84*, 4 (2012), 1963–1968.

[46] LINNINGER, A. A., TANGEN, K., HSU, C. Y., AND FRIM, D. Cerebrospinal fluid mechanics and its coupling to cerebrovascular dynamics. *Annual Review of Fluid Mechanics 48* (2016), 219–257.

[47] LOCKEY, M., POOTS, G., AND WILLIAMS, B. Theoretical aspects of the attenuation of pressure pulses within cerebrospinal-fluid pathways. *Medical and Biological Engineering 13* (11 1975), 861–869.

[48] LUI, A. C. P., POLIS, T. Z., AND CICUTTI, N. J. Densities of cerebrospinal fluid and spinal anaesthetic solutions in surgical patients at body temperature. *Canadian Journal of Anesthesia 45*, 4 (1998), 297–303.

[49] LUTZ, B. R., CHEN, J., AND SCHWARTZ, D. T. Microscopic steady streaming eddies created around short cylinders in a channel: Flow visualization and stokes layer scaling. *Physics of Fluids 17*, 2 (2005), 023601.

[50] LUTZ, B. R., CHEN, J., AND SCHWARTZ, D. T. Hydrodynamic tweezers: 1. noncontact trapping of single cells using steady streaming microeddies. *Analytical Chemistry 78*, 15 (2006), 5429–5435.

[51] LYNCH, L. Intrathecal drug delivery systems. *Continuing Education in Anaesthesia Critical Care & Pain 14* (2014), 27–31.

[52] MILHORAT, T. H. Choroid plexus and cerebrospinal fluid production. *Science 166*, 3912 (1969), 1514–1516.

[53] MILHORAT, T. H. The third circulation revisited. *Journal of Neurosurgery 42*, 6 (1975), 628–645.

[54] MILHORAT, T. H., HAMMOCK, M. K., FENSTERMACHER, J. D., RALL, D. P., AND LEVIN, V. A. Cerebrospinal fluid production by the choroid plexus and brain. *Science 173*, 3994 (1971), 330–332.

[55] MITCHELL, R. W. D., BOWLER, G. M. R., SCOTT, D. B., AND EDSTRÖM, H. H. Effects of posture and baricity on spinal anaesthesia with 0.5% bupivacaine 5 ml. *British Journal of Anaesthesia 61*, 2 (1988), 139–143.

[56] MOKRI, B. The Monro–Kellie hypothesis applications in CSF volume depletion. *Neurology 56*, 12 (2001), 1746–1748.

[57] MORTAZAVI, M. M., QUADRI, S. A., KHAN, M. A., GUSTIN, A., SURIYA, S. S., HASSANZADEH, T., FAHIMDANESH, K. M., ADL, F. H., FARD, S. A., TAQI, M. A., ARMSTRONG, I., MARTIN, B. A., AND TUBBS, R. S. Subarachnoid trabeculae: A comprehensive review of their embryology, histology,morphology, and surgical significance. *World Neurosurgery 111* (2018), 279–290.

[58] NAG, D. S., SAHU, S., SWAIN, A., AND KANT, S. Intracranial pressure monitoring: Gold standard and recent innovations. *World Journal of Clinical Cases 7*, 13 (7 2019), 1535–1553.

[59] NELISSEN, R. M. *Fluid mechanics of intrathecal drug delivery*. PhD thesis, École Polytechnique Fédérale de Lausanne, 2008.

[60] NICOL, M. E., AND HOLDCROFT, A. Density of intrathecal agents. *British Journal of Anaesthesia 68*, 1 (1992), 60–63.

[61] ONOFRIO, B. M., L., Y. T., AND G., A. P. Continuous low-dose intrathecal morphine administration in the treatment of chronic pain of malignant origin. *Mayo Clinic Proceedings 56* (1981), 516–520.

[62] Orešković, D., and Klarica, M. The formation of cerebrospinal fluid: nearly a hundred years of interpretations and misinterpretations. *Brain Research Reviews 64*, 2 (2010), 241–262.

[63] Pardridge, W. M. Drug transport in brain via the cerebrospinal fluid. *Fluids and Barriers of the CNS 8*, 1 (2011), 7.

[64] Penn, R. D. Intrathecal medication delivery. *Neurosurgery Clinics of North America 14*, 3 (2003), 381–387.

[65] Pizzichelli, G. *Modelling approaches of innovative drug delivery strategies for the Central Nervous System*. PhD thesis, Scuola Superiore Sant'Anna, 2016.

[66] Pollay, M. The function and structure of the cerebrospinal fluid outflow system. *Cerebrospinal Fluid Research 7*, 1 (2010), 9.

[67] Povey, H. M. R., Jacobsen, J., and Westergaard-Nielsen, J. Subarachnoid analgesia with hyperbaric 0.5% bupivacaine: effect of a 60-min period of sitting. *Acta Anaesthesiologica Scandinavica 33*, 4 (1989), 295–297.

[68] Rallabandi, B., Marin, A., Rossi, M., Kähler, C. J., and Hilgenfeldt, S. Three-dimensional streaming flow in confined geometries. *Journal of Fluid Mechanics 777* (2015), 408–429.

[69] Raney, W., Corelli, J., and Westervelt, P. Acoustical streaming in the vicinity of a cylinder. *Journal Of The Acoustical Society of America 26*, 6 (1954), 1006–1014.

[70] Reina, M. A., De Andrés, J. A., Hadzic, A., Prats-Galino, A., Sala-Blanch, X., and van Zundert, A. A. J. *Atlas of Functional Anatomy for Regional Anesthesia and Pain Medicine: Human Structure, Ultrastructure and 3D Reconstruction Images*. Springer, 2015.

[71] Remeš, F., Tomáš, R., Jindrák, V., Vaniš, V., and Setlík, M. Intraventricular and lumbar intrathecal administration of antibiotics in postneurosurgical patients with meningitis and/or ventriculitis in a serious clinical state. *Journal of Neurosurgery 119* (2013), 1596–1602.

[72] Richardson, M. G., Thakur, R., Abramowicz, J. S., and Wissler, R. N. Maternal posture influences the extent of sensory block produced by intrathecal dextrose-free bupivacaine with fentanyl for labor analgesia. *Anesthesia & Analgesia 83*, 6 (1996), 1229–1233.

[73] Riley, N. Oscillatory viscous flows. review and extension. *Journal of Applied Mathematics 3*, 4 (1967), 419–434.

[74] Riley, N. Steady streaming. *Annual Review of Fluid Mechanics 33*, 1 (2001), 43–65.

[75] SÁNCHEZ, A. L., MARTÍNEZ-BAZÁN, C., GUTIÉRREZ-MONTES, C., CRIADO-HIDALGO, E., PAWLAK, G., BRADLEY, W., HAUGHTON, V., AND C., L. J. On the bulk motion of the cerebrospinal fluid in the spinal canal. *Journal of Fluid Mechanics 841* (2018), 203–227.

[76] SASS, L. R., KHANI, M., NATIVIDAD, G., TUBBS, R. S., BALEDENT, O., AND MARTIN, B. A. A 3D subject-specific model of the spinal subarachnoid space with anatomically realistic ventral and dorsal spinal cord nerve rootlets. *Fluids and Barriers of the CNS 14*, 1 (2017), 36.

[77] SHAFER, S. L., EISENACH, J. C., HOOD, D. D., AND TONG, C. Cerebrospinal fluid pharmacokinetics and pharmacodynamics of intrathecal neostigmine methylsulfate in humans. *Anesthesiology 89* (1998), 1074–1088.

[78] SODERQUIST, R. G., AND MAHONEY, M. J. Central nervous system delivery of large molecules: challenges and new frontiers for intrathecally administered therapeutics. *Expert Opinion on Drug Delivery 7*, 3 (3 2010), 285–293.

[79] STOCKMAN, H. W. Effect of anatomical fine structure on the flow of cerebrospinal fluid in the spinal subarachnoid space. *Journal of Biomechanical Engineering 128*, 1 (2006), 106–114.

[80] STOCKMAN, H. W. Effect of anatomical fine structure on the dispersion of solutes in the spinal subarachnoid space. *Journal of Biomechanical Engineering 129*, 5 (2007), 666–675.

[81] STØVERUD, K. H., ALNÆS, M., LANGTANGEN, H. P., HAUGHTON, V., AND MARDAL, K.-A. Poro-elastic modeling of syringomyelia–a systematic study of the effects of pia mater, central canal, median fissure, white and gray matter on pressure wave propagation and fluid movement within the cervical spinal cord. *Computer Methods in Biomechanics and Biomedical Engineering 19*, 6 (2016), 686–698.

[82] TANGEN, K., LEVAL, R., MEHTA, A. I., AND LINNINGER, A. A. Computational and in vitro experimental investigation of intrathecal drug distribution: Parametric study of the effect of injection volume, cerebrospinal fluid pulsatility, and drug uptake. *Anesthesia & Analgesia 124*, 5 (2017), 1686–1696.

[83] TANGEN, K. M., HSU, Y., ZHU, D. C., AND LINNINGER, A. A. CNS wide simulation of flow resistance and drug transport due to spinal microanatomy. *Journal of Biomechanics 48*, 10 (2015), 2144–2154.

[84] TAO, J., SUN, Q., LIANG, W., CHEN, Z., HE, Y., AND DEHMER, M. Computational fluid dynamics based dynamic modeling of parafoil system. *Applied Mathematical Modelling 54* (2018), 136–150.

[85] TAYLOR, G. Dispersion of soluble matter in solvent flowing slowly through a tube. *Proceedings of The Royal Society of London A 219*, 1137 (1953), 186–203.

[86] TUBBS, R. S., SALTER, G., GRABB, P. A., AND OAKES, W. J. The denticulate ligament: anatomy and functional significance. *Journal of Neurosurgery 94*, 2 (2001), 271–275.

[87] VEERING, B. T., IMMINK-SPEET, T. T. M., BURM, A. G. L., STIENSTRA, R., AND VAN KLEEF, J. W. Spinal anaesthesia with 0.5% hyperbaric bupivacaine in elderly patients: effects of duration spent in the sitting position. *British Journal of Anaesthesia 87*, 5 (2001), 738–742.

[88] WALLACE, M., AND YAKSH, T. L. Characteristics of distribution of morphine and metabolites in cerebrospinal fluid and plasma with chronic intrathecal morphine infusion in humans. *Anesthesia & Analgesia 115* (2012), 797–804.

[89] WATSON, E. J. Diffusion in oscillatory pipe flow. *Journal of Fluid Mechanics 133* (1983), 233–244.

[90] WHEDON, J. M., AND GLASSEY, D. Cerebrospinal fluid stasis and its clinical significance. *Alternative Therapies in Health and Medicine 15*, 3 (2009), 54.

[91] WILDSMITH, J. A. W., MCCLURE, J. H., BROWN, D. T., AND SCOTT, D. B. Effects of posture on the spread of isobaric and hyperbaric amethocaine. *Br. J. Anaesth. 53*, 3 (1981), 273–278.

[92] YILDIZ, S., THYAGARAJ, S., JIN, N., ZHONG, X., PAHLAVIAN, S. H., MARTIN, B. A., LOTH, F., OSHINSHKI, J., AND SABRA, K. G. Quantifying the influence of respiration and cardiac pulsations on cerebrospinal fluid dynamics using real-time phase-contrast MRI. *Journal of Magnetic Resonance Imaging 46*, 2 (8 2017), 431–439.